SQUARAINE DONOR BASED ORGANIC SOLAR CELLS

By Guodan Wei

A dissertation submitted in partial fulfillment
of the requirements for the degree of
Doctor of Philosophy
(Materials Science and Engineering)
in the University of Michigan
2012

Doctoral Committee:

Prof. Stephen R. Forrest, Chair
Prof. Pallab Bhattacharya
Prof. Rachel S. Goldman
Prof. Max Shtein

DEDICATION

To my two sons Anderson Shao, Allen Shao and my husband Jing Shao

ACKNOWLEDGEMENTS

I would like to thank many people for their enormous assistance, contributions and encouragement. With all their support and help, I could continue to work for the completion of this thesis work.

Formost, I would like to express my deep appreciation to my advisor Prof. Stephen R. Forrest for his continuous support, instruction and encouragement of my Ph.D course study and research work, for his enormous patience, motivation, enthusism and immense knowledge. His instructive guidance helped me keep the right track of the projects all the time and speed up their completions. Especially, his careful correction and revision have refreshed and deepened each manuscript I have written, where I have gained precious lessons that will benefit my life in the future.

Besides my advisor, I would like to thank the rest of my thesis committee: Prof. Rachel S. Goldman, Prof. Max Shtein and Prof. Pallab Bhattacharya, for their encouragement, insightful comments and suggestions. Especially, I would like to thank Prof. Goldman for her kind words and strong support through my ways to find a balance between a graduate student and a working mom.

My sincere appreciation also goes to Prof. Mark E. Thompson and Siyi Wang for offering the promising new designed solar materials: squaraines. With more than four years' close collaboration work, we have carried out systematical and comprehensive studies on these new materials and employed them to improve solar cell performance. Also, I would like thank Dr. Kai Sun for his strong collaboration on the microscopic characterization of crystallized squaraines which greatly helps us understand the correlation between crystal structure and device performance.

I would like to thank the group members in Optoelectronic Components and Materials (OCM) Group for their friendship and collaboration. In particular, I would like to thank g, Fan YRhonda Bailey-Salzman and Elizabeth Mayo for instructing me how to fabricate organic solar cells. I would also like to thank Kuen-Ting Shiu, Noel Chris Giebink, Stephane Kena-Cohen, Marcelo Davanco and Richard Johnny Lunt for discussions and collaboration on the thermodynamic limit efficiency of quantum solar cells. Their questions, suggestions and advice guided a new direction and enlightened points in this work. The other collaborators and colleagues within OCM were a great help, including Xin Xiao, Jeramy Zimmerman, Brian Lassiter, Yifan Zhang, Ning li, Xiangfei Qi, Kyle Renshaw and Xiaoran Tong.

Last but not the least, I would like to thank my mom, my dad in heaven for supporting me spritually throughout my life; and would like to thank my parents-in-law for encouraging me and helping take care of my son, Anderson. Especially, I would like to thank my husband, Jing Shao, for his endless support and patience on my work and family life.

Guodan Wei

San Jose

October, 2011

TABLE OF CONTENTS

List of Figures

List of Table

List of Appendices

ABSTRACT

Squaraine Donor Based Organic Solar Cells

By Guodan Wei

Chair: Stephen R. Forrest

There are three main ongoing avenues to improve the power conversion efficiency of organic photovoltaics (OPV): the development of new organic **materials**, improved **process** control and novel **device** architecture design. In this thesis, through molecular design with chemical modification of functional organic molecules, a family of new highly absorptive solution processable squaraine (SQ) materials have been systematically synthesized and explored to improve the sunlight harvesting and charge transport. The spin-cast SQ donors are then coated with fullerene acceptors to form a unique nanocrystalline heterojunction (NcHJ) OPV device. This combination of a novel and efficient family of SQ donors, a unique NcHJ device architecture and optimized fabrication processes leads to high efficiency solar cells. For example, solar cells with efficiencies of ~5.7 % and a fill factor ~0.74 are achieved.

We find a correlation between solar cell fill factor with the SQ thin film density, providing support for the molecular design concept that planar end groups result in close intermolecular stacking, and hence improved charge transport and exciton diffusion. Finally, thermal annealing of the films results in the formation of nanocrystalline morphologies that lead to further improvements in device performance. The microcrystal growth of SQ donors have been characterized by XRD, AFM and TEM.

Chapter 1

Introduction to solution processed organic solar cells

Organic photovoltaics (OPV) have been considered as a potential low-cost solar energy conversion solution for an affordable and sustainable energy future. They have attracted tremendous academic interest in recent years, which stems from the potential for cost effectiveness, mechanical flexibility and easy processing [1]. As the demand for cost-competitive renewable energy sources grows, considerable advances are being placed on the synthesis [2], processing [3], theory [4] and application of new organic semiconductor materials [5]. Up to now, there has a significant improvement in device efficiency for organic solar cells with the introduction of novel organic materials [6] that tune molecular electronic properties and new device architectures [7].

This thesis is focused on solution processed small molecule squaraine donors, device processing and the relationship between molecular structure and device properties. Several efficiency improvement strategies are demonstrated to control crystallization of donor materials through thermal and solvent annealing processes in different device architectures. This chapter aims to summarize the development and characteristics of organic solar cells and highlight recent research progress in the area of solution-processed small molecular solar cells. First, pertinent definitions and device operationof organic solar cells are presented. Characteristics of organic solar cells follow, along with the difference between a planar and a bulk heterojunction (HJ). Then, recent efforts to improve solution-processed small molecular organic solar cells are highlighted.

1.1 Principles of organic solar cells

Typical OPVs are multilayer devices, consisting of electron donor (D) and acceptor (A) materials. The absorption of a photon in an OPV active region generates an exciton that can either relax back to the ground state or form a bound of electron and hole. This tightly bound exciton, or electron-hole pair, is the result of a low intermolecular orbital overlap between adjacent molecules and low dielectric constant [4]. Efficient exciton dissociation typically occurs at a D/A interface, where the donor material usually has a low ionization potential while the acceptor has a high electron affinity [8]. The dissociation of the strongly bound exciton is energetically favorable when the highest occupied molecular orbital (HOMO) and the lowest unoccupied molecular orbital (LUMO) level offsets between the donor and acceptor materials are sufficiently large to overcome the exciton binding energy [3]. Through the charge-transfer process, a free hole in the HOMO of the donor and a free electron in the LUMO of the acceptor are created after the dissociation of an exciton, as illustrated in Fig. 1.1.

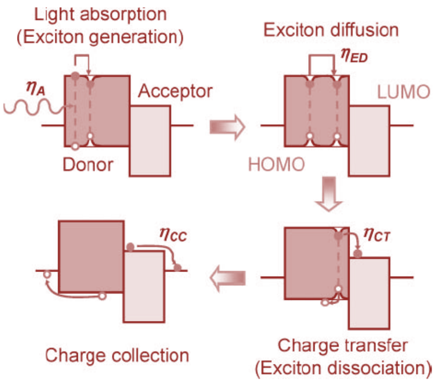

Figure 1.1: Schematic illustration of the four consecutive steps in the generation of photocurrent from incident light to an organic solar cell [8].

The optical-to-electrical conversion processes are detailed in Fig. 1 for a typical OPV: (1) photon absorption (η_α) and the subsequent generation of an exciton; (2) exciton diffusion (η_{ED}); (3) exciton dissociation into a free electron and hole by charge transfer (η_{CT}); (4) charge collection by the anode (holes) and cathode (electrons) (η_{CC}) [8]. The external quantum efficiency of the solar cell is η_{EQE}, defined as the ratio of the number of electron-hole pairs collected at the electrodes to the number of incident photons, that is, the probability that one photon converts into an electron-hole pair. Then η_{EQE} is the product of these four efficiencies, viz.:

$$\eta_{EQE} = \eta_\alpha \times \eta_{ED} \times \eta_{CT} \times \eta_{CC}, \tag{1.1}$$

Under short-circuit conditions, the photocurrent density J_{sc} can be integrated with a solar illumination spectrum of s(λ) and η_{EQE} [9], viz.:

$$J_{sc} = \int \frac{q\lambda}{hc} s(\lambda) \eta_{EQE}(\lambda) d\lambda, \tag{1.2}$$

where h is Planck's constant, q is the electron charge, λ is the wavelength, c is the speed of light and $d\lambda$ is the wavelength interval. Thus J_{sc} is directly proportional to η_{EQE}. To obtain a high photosensitivity, exciton dissociation at a D-A interface must be preceded by efficient transport of the photogenerated excitons toward this interface and followed by efficient charge extraction.

1.2 Device architectures of organic solar cells

The HJ structure is of great importance to the characteristics of the device. The basic planar (or bilayer) and bulk HJ structures are illustrated at Fig.1.2. In a planar device

(Fig.1.2(a)), the junction between the donor and acceptor materials is flat and the organic films are sandwiched between two metal electrodes with different work functions. Typically, these organic layers are vacuum deposited and their crystalline order is maintained during the growth process. In addition, their layer structures can be precisely controlled during the growth process. In this case, the photogenerated electrons and holes are spatially located in the acceptor and donor, respectively, making the recombination between these charges unlikely. Transport of photogenerated charges toward their respective electrodes is driven by the built-in electric field as well as by the concentration gradient at the heterojunction.

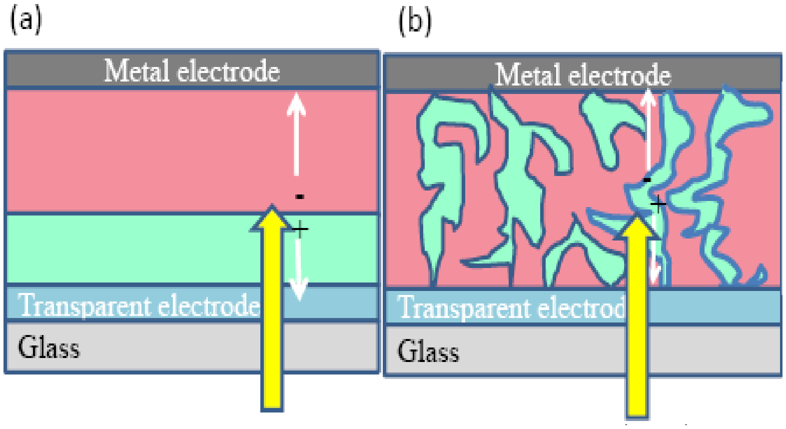

Figure 1.2: Schematic illustration of two organic solar cell architectures: (a) planar and (b) bulk heterojunction

The exciton diffusion length, L_D, in an organic material is limited due to weak intermolecular interactions. Typically, L_D is between 20 Å and 200 Å [10], which is considerably shorter than the optical absorption length (~1000 Å). This situation forms an exciton diffusion bottleneck in a planar HJ solar cell, whereby most of the photogenerated excitons cannot reach a D/A interface prior to dissociation into free carriers, ultimately limiting device performance.

In addition to the exciton diffusion limitation, planar PV cells suffer from two other problems that significantly limit their device performance. First, the deposition of the cathode metal onto the acceptor layer introduces damage, thereby reducing the exciton diffusion in that layer. Second, the incident optical electric field intensity is less than its maximum value at the HJ interface where photogenerated charge transfer is most efficient [8]. To solve these problems, an exciton blocking layer (EBL) is inserted between the acceptor layer and the metal cathode [11]. It is composed of wide-band gap material that effectively prevents the photogenerated excitons from diffusing to, and quenching at the acceptor/cathode interface. Meanwhile, this EBL material is transparent across the solar spectrum and acts as an optical spacer between the photoactive region and the metal interface. It should be thick enough to place the region of the highest incident optical intensity at the D/A interface, which is located at a distance of approximately an integer multiple of quarter wavelengths ($\lambda/4n$, where n is the index of refraction of the organic material) from the metal cathode. Thus, the optical intensity can be maximized at the D/A interface [9]. Furthermore, the EBL also functions as a buffer layer, preventing damage to the photoactive layer during metal deposition.

Typically, the EBL is about 10 nm thick to avoid the introduction of resistance to the cell and provide efficient electron transport to the cathode. The most commonly used EBLs are wide energy gap (and hence transparent) materials, such as bathocuproine

(BCP), that has been shown to have sufficiently high electron conductivity[11]. The cathode metal-deposition-induced damage on BCP results in a high density of conducting trap states. A second type of EBL is based on tris-(acetylacetonato) ruthenium (III) [Ru(acac)$_3$] and related compounds that have a small HOMO energy [12]. In this case, holes from the cathode are transported along the HOMO of Ru(acac)$_3$ and recombine with electrons at the acceptor/EBL interface. Most recently, a third type of EBL has been introduced based on 3,4,9,10 perylenetetracarboxylic (PTCBI) [13]. The LUMO of PTCBI is aligned with that of the acceptor C_{60} , allowing for low-resistance transport of electrons directly from acceptor to cathode. As a result, this PTCBI layer serves as an efficient electron conductor and forms a low energy barrier contact with the Ag cathode. Adding an transparent wide band gap 1,4,5,8-napthalene-tetracarboxylic-dianhydride (NTCDA) in combination with PTCBI allows for optimized optical spacing and efficient exciton blocking [13]. Tris-(8-hydroxyquinoline) aluminum (Alq$_3$) [14] and bathophenanthroline (BPhen) [15] are also examples of the organic materials used as EBLs in planar solar cells. In this work, both BCP and PTCBI have been used as the EBL for all devices studied.

An alternative approach to overcoming the short L_D problem as discussed in a planar HJ is to form a bulk HJ between the donor and acceptor materials with a large interface area, as shown in Fig. 1.2(b). In this case, an entangled region with two constituents is formed whereby photons can be absorbed over a long distance, creating excitons within a diffusion length of a D/A interface where photoinduced charge transfer can occur [16].

Because the L_D is typically limited to ~10 nm, the donor and acceptor materials should form nanoscale interpenetrating networks within the whole photoactive layer to ensure an efficient dissociation of excitons [17]. Nearly complete transport of excitons to the D/A interface is achieved by establishing an intimate contact between donor and acceptor materials by blending [2], laminating [18], codeposition [3] or chemical linking [19].

Compared to a planar HJ solar cell (Fig.1.2(a)), the conceptual advantage of a BHJ cell is that the interface area is enhanced enormously and that a thicker photoactive layer, optimized for light absorption, can be incorporated in a device. BHJ solar cells consisting of a mixture of donor and acceptor materials, leads to an increase in donor/acceptor junction interfacial area, but often results in no continuous carrier pathways on the one side as planar HJ solar cells [16]. As a result, carrier mobilities are reduced in the mixed layer of bulk HJ cells than in the homogeneous layers of planar HJ cells, and recombination of electron and holes in the active layer can be very significant. Therefore, research in this area has focused on improving the charge transport properties of the blending materials by controlling the domain size and the morphologies of the constituents such that the two phases form percolating paths along which the photogenerated carriers can be readily transported to their respective electrodes [1, 20]. This approach has resulted in a significant improvement in power conversion efficiency over that obtained from a simple planar structure [21].

Overall, there are two basic requirements for efficient organic solar cells: (1) one must maximize the interface area for efficient exciton dissociation between donor and acceptor materials; and (2) create continuous pathways for charge transport to the respective electrodes [16]. Usually, the simple bilayer planar HJ is vacuum deposited using small-molecular- weight organic donor and acceptor materials, although the organic layer thickness and cell efficiency are limited by their short L_D. Compared with polymer materials, it is more difficult for small-molecular-weight materials to achieve a bulk HJ, since their phase separation usually occurs in the solid rather than in the liquid phase. Simply mixing materials by co-evaporation of the donor and acceptor materials can result in a significant decrease in charge carrier mobility, as has been observed by the co-deposition of D/A pair, copper phthalocyanine (CuPc)/PTCBI and CuPc/C_{60} [22]. When deposited into a mixture, their crystal stacks are disrupted, introducing charge trapping and scattering during transport to the electrode. Hence, mixed-layer devices typically have high series resistance, resulting in carrier recombination. One means to circumvent the low mobility of charge in disordered organic films is to create morphological order that leads to a low resistance to charge conduction, lacking bottlenecks or islands that impede carrier extraction through organic vapor phase deposition (OVPD) [7]. The control of organic film crystallization and morphology results in a low resistance, ordered and interdigitated interface in a bulk CuPc:C_{60} HJ cell. This significantly improves efficiency over otherwise a planar CuPc/C_{60} HJ cell.

1.3 Characteristics of organic solar cells

Due to the potential for low cost solar energy conversion, OPVs have attracted tremendous attention since a 0.95 % power conversion efficiency solar cell based on a single D/A planar heterojunction was reported in 1986 [23]. This cell consisted of a CuPc/PTCBI bilayer evaporated onto an indium-tin-oxide (ITO) coated substrate glass (Fig.1.3(a)). The energy offset between the HOMO of the CuPc donor, and the LUMO of the PTCBI acceptor, dissociates the excitons into free electron and holes. The underlying ITO anode is where the holes are collected. And the top contact Ag is where the electrons are collected. In this device, the solar irradiation enters the cell from the glass/ITO side, and is absorbed by the organic layer composed of D/A HJs. The top contact reflects light back into the organic layers, increasing optical interferenceand photon absorption. The first small molecule bilayer organic solar cell showed well defined diode characteristics and a short circuit current density of J_{sc}=2.3 mA/cm^2, open circuit voltage of V_{oc}=0.45V, fill factor FF=0.65 and power conversion efficiency η_p=0.95% under simulated air mass 2(AM2) illumination [23]. Since then, the pace of advances has been rapid with the development of vacuum-deposited small molecular and solution-processed polymer blend solar cells. In organic HJs, there is no strict requirement of lattice matching of the dissimilar materials, providing ease of material growth and selection.

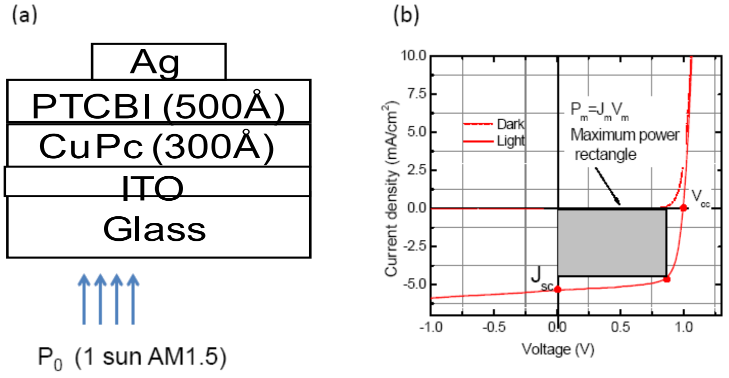

Figure 1.3: (a) the structure of a CuPc/PTCBI bilayer solar cell;(b) the current density

(J)-Voltage (V) is measured in the dark and under 1 sun illumination [23].

The equivalent circuit of a PV cell is shown in Fig. 1.4. A PV cell can be modeled as an ideal diode in parallel with a current density source, J_{ph}. An actual PV cell includes a parallel shunt resistance R_p (or R_{sh}) due to the recombination current through the device, and a series resistance R_s, which results from the finite electrical conductivities of the semiconductor and the electrode materials, as well as the contact resistance between them.

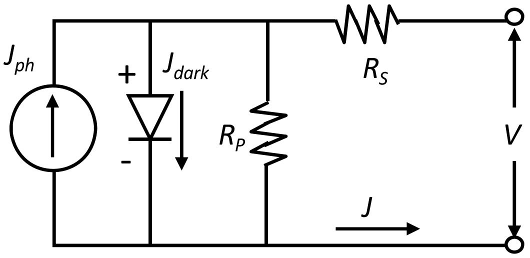

Figure 1.4: Equivalent circuit of a photovoltaic cell [24].

The current density (J)-applied voltage (V) characteristics of organic solar cells can be expressed using the modified ideal diode equation for organic heterojunctions:[24]

$$J = J_s[\exp(q(V - JR_s)/nk_BT) - \frac{k_{PPd}}{k_{PPd,eq}}] + \frac{V - JR_s}{R_p} - J_{ph} \tag{1.3}$$

here, J_s is the reverse saturation current density, q is the electron charge, R_s is the series resistance, n is the ideality factor, k_B is the Boltzmann constant, T is the temperature, and R_p is the parallel (or shunt) resistance. k_{PPd} is the polaron pair dissociation rate and $k_{PPd,eq}$ is polaron pair equilibrium value. For V<0, the interfacial field in the solar cell is high and aids dissociation. Thus, k_{PPd} grows larger than k_{PPd} and the reverse saturation current increases with increasing reverse bias, as typically observed in organic HJs[24]. Under forward bias, k_{ppd} is similar to or less than $k_{PPd,\ eq}$ and the current density increases exponentially with an ideality factor n=1. J_{ph} is the photocurrent density.

Fig. 1.3(b) illustrates the typical *J-V* characteristics of a PV cell in the dark and under illumination. Since the photocurrent density flows in the opposite direction to the normal diode current density (i.e. $J_{ph} < 0$), the product $J \times V < 0$ for $0 < V < V_{oc}$, where V_{oc} is the open-circuit voltage. V_{oc} refers to the maximum possible voltage across a PV cell when no current is flowing. The short circuit current, J_{sc}, is defined as the current when there is zero load resistance.

An important parameter to characterize a PV cell is its power conversion efficiency $\eta_{p.}$ It is defined as the ratio of the maximum electrical power output, P_m to the incident optical power density, P_0. The maximum electrical power output is the maximum area of a rectangle drawn within the *J-V* characteristics in the fourth quadrant as shown in Fig. 1.3(b):

$$P_m = \max_{0<V<V_{oc}} |JV| = J_m \times V_m \tag{1.4}$$

where J_m and V_m are the current density and voltage corresponding to the maximum power output, respectively. It can also be expressed as:

$$P_m = J_{sc} V_{oc} FF \tag{1.5}$$

Where $FF = J_m V_m / J_{sc} V_{oc}$ is the fill factor that is related to the shape of the *J-V* characteristics. Hence, the power conversion efficiency can be expressed as,

$$\eta_p = \frac{P_m}{P_0} = \frac{J_{sc}V_{oc}FF}{P_0} \tag{1.6}$$

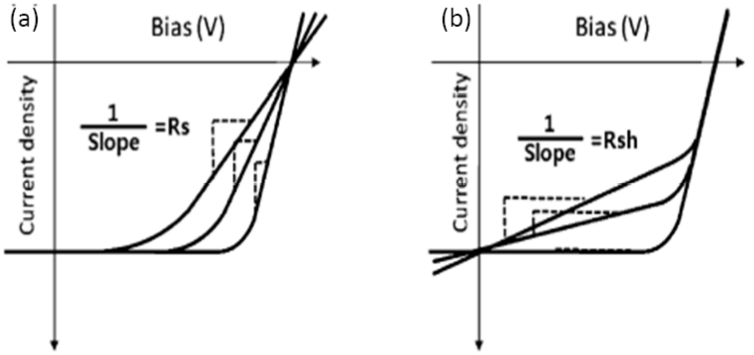

Figure 1.5: (a) increasing series and (b) reducing parallel resistance. In each case the effect of the resistances is to reduce the area of the maximum power rectangle compared to $J_{sc} \times V_{oc}$ [25].

The power generated by a solar cell is dissipated through the resistance of the contacts and through leakage currents around the sides of the device. These effects are electrically equivalent to two resistances: R_s and R_p. The series resistance, R_s, is a function of cell material, particularly through the front surface to the contacts, and from resistive contacts. R_s is a particular problem for bulk HJ solar cells, especially under high power intensity illuminations. The parallel resistance, R_p , arises from leakage of current and recombination current through the junction. Both the R_s and R_p reduce the fill factor as shown in Fig. 1.5. For an efficient solar cell, R_s should be keptsmall and the R_p maximized.[25].

1.4 Recent research progress of solution processed bulk HJ solar cells

1.4.1 Recent research progress of polymer bulk HJ solar cells

The design of a bulk HJ structure allows for extraction of charges from a much larger volume of active material, increasing both light absorption and photocurrent generation [17, 26]. Recent efforts focus on controlling donor/acceptor phase separation [27], increasing and balancing charge-carrier mobilities [28], and searching for new materials that maximize absorption of the solar spectrum [16].

Research on polymer:fullerene blend solar cells started in 1995 with an accepted power conversion efficiency of 2% [26]. Solution processed mixtures of polyphenylene vinylenes (PPV) and [6,6]-phenyl-C_{61}-butyric acid methylester (PCBM) demonstrated a charge transfer rate at the PPV and PCBM interface on a picosecond time scale, leading to high efficiency. With appropriate organic solvents and spin-cast conditions, well-controlled phase separation improved the polymer bulk HJ cell efficiencies to 2.5% [19], indicating the intimate correlation between nanomorphology of active layers and device performance. However, a bottleneck in the PPV-related bulk cells is that the lower hole mobility of PPV phase in the blend films, compared with the electron mobility of PCBM, leads to space-charge-limited photocurrent and carrier recombination. Regioregular poly(3-hexylthiophene) (P3HT), a polymer with higher hole mobility, was introduced and started to replace PPV, achieving an efficiency surpassing 5% with optimized phase separation [29]. The main disadvantage of P3HT is the poor matching of its photon absorbance with the solar illumination spectrum. The bandgap of P3HT is around 1.9 eV, limiting the absorbance to λ<650 nm. When replacing P3HT with the smaller bandgap polymer, poly[2,6-(4,4-bis-(2-ethylhexyl)-4H-cyclopenta[2,1-b;3,4-b′]- dithiophene)-lt-4,7- (2,1,3-benzothiadiazole)] (PCPDTBT, Eg = 1.46 eV) and PC$_{70}$BM (PC$_{70}$BM: phenyl-C$_{70}$-butyric acid methyl ester), cell efficiencies of up to 5.5% have been obtained [30]. In a tandem structure processed from spin-casting, combining the P3HT and PCPDTBT donor materials, a power conversion efficiency of 6.5% was demonstrated [31]. Most recently, new thieno[3,4-b]thiophenebenzodithiophene polymers (PTBs) have been developed for bulk HJ PTB7/PC$_{70}$BM solar cells withη_p =7.4% [21]. The dependence of performance on polymer materials such as regioregularity, polydispersity, and stability [8] has not yet been fully addressed.

1.4.2 Recent research progress of small molecule bulk HJ solar cells

Although most research work in the field of organic bulk HJ solar cells has focused on the mixture of conducting polymers as a donor and a fullerene-based acceptor, recent research has also demonstrated the feasibility of solution-processed small molecule bulk solar cells [27]. Polymers are generally more difficult to synthesize and purify than small molecules. Small molecules have the advantages including monodispersity, high charge carrier mobility and relatively simple synthesis [32].

It is generally believed that factors such as limited solubility and tendency to aggregate in most organic solvents are responsible for the difficulty in solution processing of small molecule organic materials. There are strong intermolecular forces between these conjugated small molecules facilitating intermolecular electron delocalization, which is favorable for efficient charge transport. On the other hand, these strong interactions are also responsible for the crystal nucleation in solution, resulting in low solubility and poor film formation [32]. Despite their difficulties for solution processing, soluble small molecule OPV shave shown steady progresss over the past ten years (Fig.1.6). Representative classes of materials including pentacene derivatives [32], oligothiophenes [27], diketopyrrolopryrroles [33] and push-pull type oligomers [34], as well as a few other dye-based materials [35].

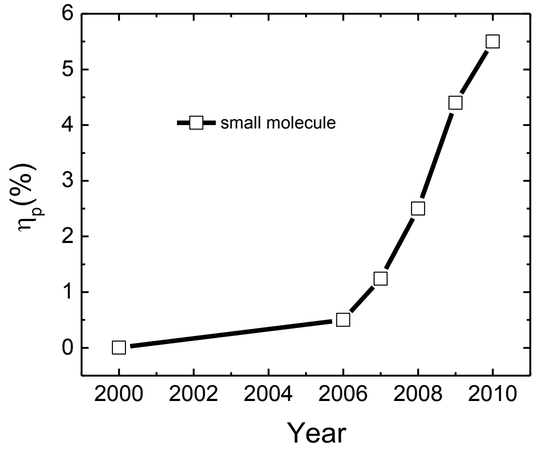

Figure 1.6: Efficiency improvement over years for solution processed small molecule bulk HJ solar cells

Originally, the pioneering work on solution processed small molecule OPVs was carried out on pentacene derivatives such as 6,13-bis(triisopropylsilylethynyl)pentacene (TIPS-pentancene) [32]. The TIPS side groups carry the additional advantage of imparting solubility and facile film formation to the insoluble pentacene molecule.

Unfortunately, TIPS-pentacene has a reaction with fullerene derivatives, resulting in inefficient photoinduced charge transfer. The optimized efficiency was around 0.5%.

Recently, researchers have made progress on 3,6-diaryl-2,5-dihydro-pyrrolo-[3,4-c]pyrrole-1,4-dione (DPP)-based materials [36]. By replacing bithiophene with a benzofuran substituent, the DPP-based molecules have increased intermolecular chromophore interaction through high conjugation. With an optimized ratio of $PC_{70}BM$, the as-cast blend film had very little phase separation. Upon thermal annealing, the surface of the film roughens and shows distinct donor and acceptor domains, resulting in well-controlled phase separation of the DPP-based donor and $PC_{70}BM$ acceptor. The deep HOMO band of the donor material yields an increased V_{oc} =0.9V, J_{sc} =10 mA/cm^2, FF = 0.48, an optimized device efficiency of 4.4%[36].

Several groups have explored a variety of other materials over the past few years including several well-known classes of dye molecules such as borondipyrromethene (BODIPY) [37], merocyanine[38] and squaraine[39]. For soluble small molecule bulk HJ solar applications, these dye materials have been functionalized with solubilizing groups. Squaraines are the condensation products of squaric acid and two equivalents of a suitable electron-rich precursor. They are a class of functional organic dyes for a variety of electronic and photonic applications such as imaging, nonlinear optics, photovoltaics, photodynamic therapy and ion sensing [40]. From the standpoint of their electronic properties, squaraines are highly delocalized conjugated molecules possessing a cyanine-like structure. Their most notable features are that they have sharp and intense absorption in the long-wavelength region, good solubility in low polarity solvents, and they possess considerable photo- and thermal stability under ambient conditions [41]. Due to the synthetic access of a variety of the squaraine dyes with structural variations and the strong absorption and emission properties that respond to the surrounding medium, squaraine dyes have been receiving significant attention and have been extensively investigated in recent years for applications in bulk HJ solar cells [39] and the dye-sensitized solar cells [42], from both fundamental and technological viewpoints.

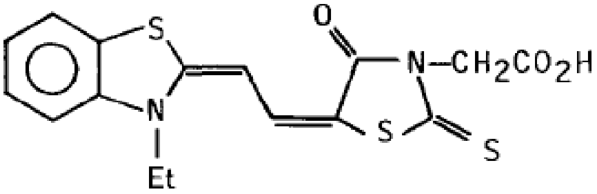

Figure 1.7: Chemical structure of merocyanine dye used in fabricating Al/merocyanine/Ag organic solar cells [43].

The application of squaraines in organic photovoltaics has extended back to 1978 [43], when conventionally vacuum evaporated merocyanine photosensitizing dyes (Fig. 1.7) were sandwiched between two metal electrodes in single layer solar cells with V_{oc}=1.2 V, FF=0.25, J_{sc}=1.8 mA/cm^2 , affording power conversion efficiency of 0.7%. More recently, Grätzel [42] and Marks [39] have extensively employed the hydrazine end capped squaraines in the preparation of solution-processed bulk OPV cells. These squaraine-based BHJ OPVs can be fabricated by conventional spin-coating under ambient atmosphere, which is an important advantage over polymer-based devices.

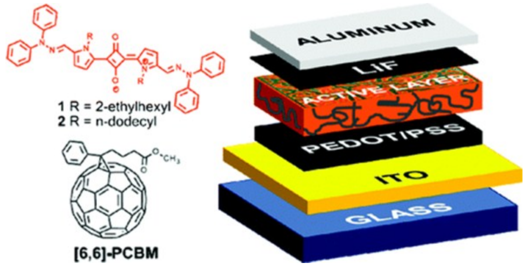

Figure 1.8: New squaraine donors **1** (R=2-ethylhexyl) and **2** (R=n-dodecyl); schematic diagram of squaraine:PCBM bulk solar cells [39].

New soluble squaraine derivatives (Fig. 1.8) as molecular donors were mixed with PCBM from $CHCl_3$ solution to fabricate small molecule BHJ solar cells, exhibiting efficiency of 1.24 % [39], with a short circuit current density of 5.70 mA/cm^2. The use of linear and branched alkyl chain substituents allows managing the squaraine solubility and at the same time offers a tool for the control of the solid-state organization. The same group further reported new squaraines, substituted at the pyrrolic nitrogen with n-hexyl or n-hexenyl chains as shown in Fig. 1.9. The N-alkenyl substituent affords a more compact solid-state structure, enhancing charge mobility (thin film transistor hole mobility is increased ~5×), and OPV performance with η_p =2.05%) [5]. Wurther and co-workers reported an unusually high J_{sc} =12.6 mA/cm^2 from their own squaraine-based materaials with PCBM. However, the V_{oc} = 0.31 V was low [44]. Studies are currently underway to better define and optimize processing/microstructure/photovoltaic response relationships.

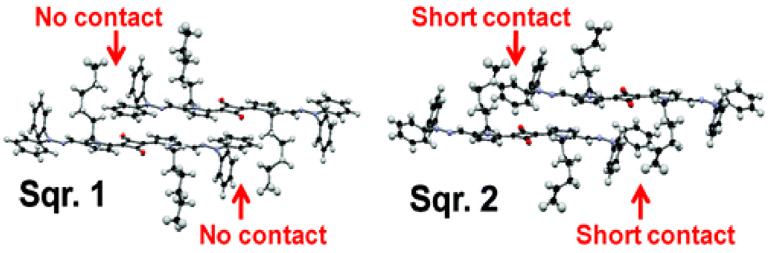

Figure 1.9: Two new squaraine dyes substituted at the pyrrolic rings with n-hexyl

(squaraine 1) or n-hexenyl (squaraine 2) chains. The presence of the terminal double bond results in a much more compact solid-state structure, dramatically affecting charge transport in the thin films [5].

Although squaraine-based OPV devices are typically processed by solution methods, recently, S. Y. Wang, et al. have developed a new squaraine with four hydroxyl groups at the 2, 6-positions of the two phenyl rings to prevent molecular decomposition on sublimation, and have successfully purified it by multiple cycles of thermal gradient sublimation in vacuum [45]. The peak optical density in the thermally evaporated squaraine film is 2.0×10^5 cm^{-1} at a wavelength of λ_{max}=700 nm. An efficient device by vacuum evaporation of the squaraine film in a planar heterojunction structure of composition ITO/squaraine/C_{60}/BCP/Ag was obtained. The thickness of the various layers was optimized to give a 3.1% efficiency at 1 sun illumination with V_{oc} = 0.76 V, J_{sc} = 7.0 mA/cm^2 and FF= 0.56 for a device using a 65 Å thick layer of the squaraine. This result opens the way for sublimable squaraine derivatives for new donors in high vacuum grown OPV devices,. In this work, we employ this solution processable squaraine donor for efficient bulk HJ solar cells.

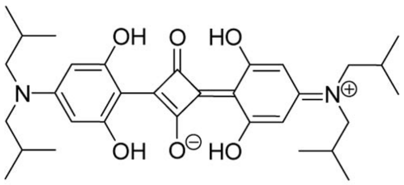

Figure 1.10: Molecular structure of a new squaraine with four hydroxyl groups [45].

1.5 Thesis overview

This work focuses on improving organic solar cell efficiency through solution processed a family of new squaraine donor materials.

The interplay of J_{sc}, V_{oc} and FF determines the final efficiency. V_{oc} depends on the energy offset at the donor/acceptor interface, which can be improved by tuning and designing new squaraine donor materials. J_{sc} is enhanced through understanding the energy harvesting process and shifting the absorption spectrum into longer wavelengths. High FF is achieved through controlling the charge collection process and building new device architectures.

In this introductory chapter, we have discussed the basic principles of organic solar cells on how to efficiently convert photons into free carriers. Two different organic solar cell structures have been introduced and their comparison was discussed. The past progress on solution-processed organic solar cells has implied the importance of the donor material choice to improve device performance. Our goals in this work are to (1) explore new squaraine donor materials; (2) explore novel device architectures for efficiency improvement; (3) understand the correlation between molecular structure and device performance.

In Chapter 2, we examine squaraine device performance employing SQ:$PC_{70}BM$ and SQ:$PC_{60}BM$ bulk HJ structures, in comparison with SQ/C_{70} and SQ/C_{60} planar HJ structures. This result indicates that the nanoparticle morphology introduces internal resistance into the solution-based SQ:$PC_{70}BM$ and SQ:$PC_{60}BM$ blend thin films. The distribution of the SQ donor nanoparticles in the acceptor matrix as a function of relative concentration results in a trade-off between exciton dissociation and hole mobility. In Chapter 3, we show that the performance of SQ/C_{60} photovoltaic cells is influenced by the nanomorphology and crystallinity of the SQ film controlled via the post-deposition annealing process. The rough surface of the annealed SQ film is on the scale of its exciton diffusion length. The improved hole transport through SQ films greatly reduces its internal resistance, leading to efficiency increased to 4.6 ± 0.1% at 1 sun, AM 1.5G. This nanocrystalline bulk HJ structure will be further applied to a family of new squaraines in the following chapters (Chapter 5-7).

In Chapter 4, we improve device performance of SQ:$PC_{70}BM$ (1:6) bulk solar cells through post-solvent annealing. This leads to control of the nanoscale phase separation of SQ:$PC_{70}BM$ (1:6) organic blend films. Through optimizing morphology and molecular ordering of the SQ:$PC_{70}BM$ (1:6) solar cells, a peak efficiency of 5.2 ± 0.3 % has been achieved, with a maximum cell performance achieved when the exciton diffusion length is approximately equal to the mean SQ crystallite size.

In the following chapters (Chapter 5 to 6), we discuss several new squaraines employed the nanocrystalline bulk structures. In Chapter 5, we discuss bulk HJ 1-NPSQ/C_{60} solar cells with roughened interface morphology, which has improved J_{sc} (10.0 mA/cm^2) and V_{oc} (0.90 V). The peak efficiency reaches 5.7 %. In Chapter 6, we explore a family of new squaraines with PTCBI as an electron conducting blocker layer, and study the correlation between molecular structure and device performance. We find a correlation between solar cell *FF* with the functionalized SQ thin film density, providing support for the concept that planar end groups result in close intermolecular stacking, and hence improved charge transport and exciton diffusion.

Finally, Chapter 7 presents conclusions and outlook. In the outlook part of this chapter, we discuss growth and control strategies, possible new donor material designs and device structure design to improve solar cell performance.

References

[1] L. M. Chen, Z. R. Hong, G. Li, and Y. Yang, *Adv.Mater.* **21**, 1434 (2009).

[2] H. Y. Chen, J. H. Hou, S.Q. Zhang, Y.Y. Liang, Y. Yang, L.P. Yu, Y. Wu and G. Li, *Nature Photonics* **3**, 649 (2009).

[3] P. Peumans, S. Uchida, and S. R. Forrest, *Nature* **425**, 158 (2003).

[4] P. Peumans and S. R. Forrest, *Chem. Phys. Lett.* **398**, 27 (2004).

[5] D. Bagnis, L. Beverina, H. Huang, F. Silvestri, Y. Yao, H. Yan, G. A. Pagani, T. J. Marks, and A. Facchetti, *J.Am. Chem. Soc.* **132**, 4074 (2010).

[6] J. M. Szarko , J. C. Guo, Y. Y. Liang, B. Lee , B. S. Rolczynski , J. Strzalka , T. Xu , S. Loser , T. J. Marks , L. P. Yu , and L. X. Chen, *Adv.Mater.* **22**, 5468 (2010).

[7] F. Yang, K. Sun, and S. R. Forrest, *Adv.Mater.* **19**, 4166 (2007).

[8] S. R. Forrest, *MRS Bulletin* **30**, 28 (2005).

[9] P. Peumans, A. Yakimov and S.R. Forrest, *J. Appl. Phys.* **93** (7), 3693 (2003).

[10] R. R. Lunt, N. C. Giebink, A. A. Belak, J. B. Benziger and S. R. Forrest, *J. Appl. Phys.* **105**, 053711 (2009).

[11] P. Peumans, V. Bulovic, and S. R. Forrest, *Appl.Phys. Lett.* **76**, 2650 (2000).

[12] B. P. Rand, J. Li, J. G. Xue, R. J. Holmes, M. E. Thompson, and S. R. Forrest, *Adv.Mater.* **17**, 2714 (2005).

[13] B. E. Lassiter, G. D. Wei, S. Y. Wang, J. D. Zimmerman, V. V. Diev, M. E. Thompson, and S. R. Forrest, *Appl.Phys. Lett.* **98**, 243307 (2011).

[14] Q. L. Song, F. Y. Li, H. Yang, H. R. Wu, X. Z. Wang, W. Zhou, J. M. Zhao, X. M. Ding, C. H. Huang, and X. Y. Hou, *Chem.Phys. Lett.* **416**, 42 (2005).

[15] M. Y. Chan, C. S. Lee, S. L. Lai, M. K. Fung, F. L. Wong, H. Y. Sun, K. M. Lau, and S. T. Lee, *J. Appl. Phys.* **100**, 094506 (2006).

[16] G. Li, V. Shrotriya, J. Huang, Y. Yao, T. Tommoriarty, K. Emery, and Y. Yang, *Nature Mater.* **4**, 864 (2005).

[17] D. H. Wang, J. S. Moon, J. Seifter, J. Jo, J. H. Park, O.O Park, and A. J. Heeger, *Nano Letters* **11**, 3163 (2011).

[18] J. J. M. Halls, C. A. Walsh, N. C. Greenham, E. A. Marseglia, R. H. Friend, S. C. Moratti, and A. B. Holmes, *Nature* **376**, 498 (1995).

[19] S. E. Shaheen, C. J. Brabec, N. S. Sariciftci, F. Padinger, T. Fromherz, and J. C. Hummelen, *Appl.Phys. Lett.* **78** (6) (2001).

[20] J. B. Kima, Z. L. Guan, S. Lee, E. Pavlopoulou, M. F. Toney, A. Kahn, and Y. L Loo, *Organic Electronics* **12**, 1963 (2011).

[21] Y. Y. Liang, Z. Xu, J. B. Xia, S. T. Tsai, Y. Wu, G. Li, C. Ray, and L. P. Yu, *Adv.Mater.* **22** (20), E135 (2010).

[22] B. P. Rand, J. G. Xue, S. Uchida, and S. R. Forrest, *J. Appl. Phys.* **98**, 124902 (2005).

[23] C. W. Tang, *Appl.Phys. Lett.* **48** (2), 183 (1986).

[24] N. C. Giebink, G. P. Wiederrecht, M. R. Wasielewski, and S. R. Forrest, *Phys. Rev. B*, **82**, 155305(2010).

[25] M. S. Kim, B. G. Kim, and J. Kim, *ACS Appl. Mater&Interfaces* **1** (6), 1264 (2009).

[26] G. Yu, J. Gao, J. C. Hummelen, F. Wudl, and A. J. Heeger, *Science* **270**, 1789 (1995).

[27] B. Walker, A. B. Tamayo, X. D. Dang, P. Zalar, J. H. Seo, A. Garcia, M. Tantiwiwat, and T.Q. Nguyen, *Adv.Funct.Mater.* **19**, 3063 (2009).

[28] L. J. A Koster, V. D. Mihailetchi, and P. W. M. Blom, *Appl.Phys. Lett.* **88** (5), 052104 (2006).

[29] W. Ma, C. Yang, X. Gong, K. Lee, and A. J. Heeger, *Adv. Func.Mater.* **15** (10), 1617 (1995).

[30] J. Peet, J. Y. Kim, N. E. Coates, W.L. Ma, D. Moses, A. J. Heeger, and G. C. Bazan, *Nature Mater.* **6**, 497 (2007).

[31] J.Y. Kim, K. Lee, N .E. Coates, D. Moses, T. Q. Nguyen, M. Dante, and A. J. Heeger, *Science* **317** (5835), 222 (2007).

[32] M.T. Lloyd, J. E. Anthony, and G. G. Malliaras, *Mater. Today* **10** (11), 34 (2007).

[33] A. B. Tamayo and T. Q. Nguyen, *J. Phys. Chem. C* **112** (30), 11545 (2008).

[34] P. F. Xia, J. P. Lu, S. W. Tsang, R. Movileanu, Y. Tao, and M. S. Wong, *Adv. Mater.* **20** (24), 4810 (2008).

[35] F. Silvestri, M. D. Irwin, L. Beverina, A. Facchetti, G. A. Pagani, and T. J. Marks, *J. Am. Chem. Soc* **130**, 17640 (2008).

[36] A. B. Tamayo B. Walker, X. D. Dang, P. Zalar, J. H. Seo, A. Garcia, M. Tantiwiwat, T. Q. Nguyen, *Adv.Func.Mater.* **19**, 3063 (2009).

[37] T. Rousseau, T. Bura, G. Ulrich, R. Ziessel, and J. Roncali, *Chem.Comm.* **13**, 1673 (2009).

[38] N. M. Kronenberg, M. Deppisch, F. Wurthner, H. W. A. Lademann, K. Deing, and K. Meerholz, *Chem. Comm.* **48**, 6489 (2008).

[39] F. Silvestri, M. D. Irwin, L. Beverina, A. Facchetti, G. A. Pagani, and T. J. Marks, *J.Am. Chem. Soc.* **130**, 17640 (2008).

[40] S. Sreejith, P. Carol, P. Chithra, and A. Ajayaghosh, *J.Mater.Chem.* **18**, 264 (2008).

[41] L. Beverina, M. Drees, A. Facchetti, M. Salamone, R. Ruffo, and G. A. Pagani, *Eur. J. Org. Chem.* **2011** (28), 5555 (2011).

[42] Y. R. Shi, R. B. M. Hill, J. H. Yum, A. Dualeh, S. Barlow, M. Gratzel, S. R. Marder, and M. K. Nazeeruddin, *Angew. Chem. Int. Ed.* **50**, 6619 (2011).

[43] A.K. Ghosh and T. Feng, J. Appl. Phys. **49** (12), 5982 (1978).

[44] U. Mayerhoffer, K. Deing, K. Gruß, H. Braunschweig, K. Meerholz, and F. Wurthner, *Angew. Chem. Int. Ed.* **48**, 8776 (2009).

[45] S.Y. Wang, E. I. Mayo, M. D. Perez, L. Griffe, G. D. Wei, P I. Djurovich, S. R. Forrest, and M. E. Thompson, *Appl.Phys. Lett.* **94**, 233304 (2009).

Chapter 2

Solution processed squaraine bulk heterojunction photovoltaic cells

2.1 Introduction to bulk heterojunction solar cells

Bulk-heterojunction (BHJ) solar cells consisting of interpenetrating blends of electron- and hole- transporting materials offer promise for low-cost, sustainable electricity production [1-3]. Efficient charge generation throughout the active blends, ultrafast charge transfer at the donor/acceptor interface and efficient charge transport are essential for high performance photovoltaic applications [4]. Due to their potential low-cost of fabrication, solution processing has been widely explored to demonstrate polymeric bulk HJ solar cells with high power efficiencies [5-7], although the dependence of performance on polymer materials such as regioregularity, polydispersity, and stability [8] has not been fully addressed.

In contrast, small molecules are intrinsically monodisperse and simple to synthesize and purify. In general, the concept of the bulk heterojunction has been demonstrated in small-molecular weight organic solar cells with active layers co-deposited by vacuum thermal evaporation [9] or organic vapor phase deposition [10]. There are also examples of small molecules that have been used as solution processable donor materials in BHJ architectures[11-13]. Unfortunately, the strong intermolecular forces between conjugated small molecules can result in the nucleation of molecular crystals in solution, generating incomplete film coverage with high surface roughness. To obtain improved performance, efforts have focused on the design and synthesis of soluable donors with high charge carrier mobility and absorption in the visible and new-infrared spectral regions, in combination with a high interfacial gap energy at the donor-acceptor interface [8]. Among these, 2,4-*bis* [4-(*N,N*-diisobutylamino)-2,6-dihydroxyphenyl] squaraine (SQ) dyes with four hydroxyl groups at the 2,6-positions of the two phenyl rings with four hydroxyl groups [14] have been identified as donors that absorb at wavelengths λ>650 nm while, when combined with a C_{60} acceptor layer, have a larger open circuit voltage (V_{oc}) than that of the commonly used copper phthalocyanine (CuPc)/C_{60} cell [15].

2.2 Cell series resistance

The series resistance (R_s) of an organic solar cell reduces its power conversion efficiency (η_p). The series resistance comes from the finite electrical conductivities of the organic materials and contact electrodes. For an (R_s=0) ideal PV cell, the short-circuit current densities (J_{sc}) depends linearly on the incident power density (P_o), the open-circuit voltage (V_{oc}) increases logarithmically with P_o, and the Fill Factor (FF) also increases with P_o. For this case, the efficiency, is:

$$\eta_p = \frac{P_m}{P_0} = \frac{J_{sc} V_{oc} FF}{P_0} \tag{2.1}$$

organic solar cells have resistance $R_s \neq 0$, limits by the low carrier mobility and electrical conductivity of organic materials. To obtain high J_{sc} and FF, solar cells must have low R_s. In organic solar cells, the FF is limited by the carrier drift length, L_d, [15]

$$L_d = \mu \tau E \tag{2.2}$$

where μ is the carrier mobility, τ is the carrier recombination lifetime and E is the electric field. L_d must be longer than the active thickness to prevent significant loss by recombination. Hence, the low mobility of the organic thin film typically limits the efficient charge-carrier extraction, resulting in a decrease in FF with increasing P_o. A high mobility is necessary to extract the photogenerated carriers without significant loss from recombination.

In this chapter, we show that series resistance fundamentally limits the current SQ BHJ solar cells, due to the low hole mobility in squaraine donors. The combination of the optical, electrical and chemical properties of SQs blended in solution with [6, 6]-phenyl C_{70} butyric acid methyl ester ($PC_{70}BM$) in a 1:6 mixture results in cells with power conversion efficiency η_p=2.7 ± 0.1 %, short-circuit current density J_{sc}= 8.85 ± 0.22 mA/cm^2, and V_{oc} =0.89 ± 0.01 V at 1 sun intensity, AM1.5G simulated solar emission. This corresponds to a peak external quantum efficiency of EQE=48 % at a wavelength of λ=385 nm. Its peak power conversion efficiency of η_p=3.3 ± 0.3 % at 0.2 sun is compared with a control, planar heterojunction SQ/C_{60} cell with an efficiency of 4.1 ± 0.2 % at 1 sun (correcting for solar mismatch). We show that the morphology of the SQ:$PC_{70}BM$ composite affects the hole transport mobility, resulting in an unbalanced electron and hole transport and relatively low FF. The higher efficiency of the control SQ/C_{60} device is due to the nanocrystalline BHJ morphology, resulting in high hole mobility and hence efficient charge collection efficiency.

2.3 Properties of pure squaraine and mixed squaraine:$PC_{70}BM$ thin films

2.3.1 Crystal structure of squaraine material

X-ray-diffraction (XRD) patterns of the SQ powder plus the neat SQ, $PC_{70}BM$ and SQ:$PC_{70}BM$ (in weight concentrations of 3:1, 1:1, 1:2, 1:3 and 1:6) thin films spin-coated on indium tin oxide (ITO) substrates at a rate of 3000 RPM (revolutions per minute) were obtained using a Rigaku diffractometer in the θ-2θ geometry using a 40 kV Cu K_α radiation source. The neat SQ thin films with thicknesses of 360Å were annealed at temperatures varied from 70 ^{0}C to 130 ^{0}C.

The SQ powder characterized by XRD (Fig. 1(a)) indicates a monoclinic unit cell [space group P2/m with a=18.36, b=5.87, c=14.93 Å, $\beta=91.24^0$] [17-18]. Thin films annealed at 110 ^{0}C and 130 ^{0}C for 10 min exhibit (001) and (002) peaks at $2\theta=7.58^0$ and $2\theta=15.29^0$ (Fig. 2.1(b)) corresponding to an intermolecular spacing of d_{002}=7.50 Å. There are no peaks for SQ, $PC_{70}BM$ and SQ:$PC_{70}BM$ blends with five different ratios of 3:1,1:1, 1:2, 1:3 and 1:6 annealed at 70^{0}C, indicating amorphous films.

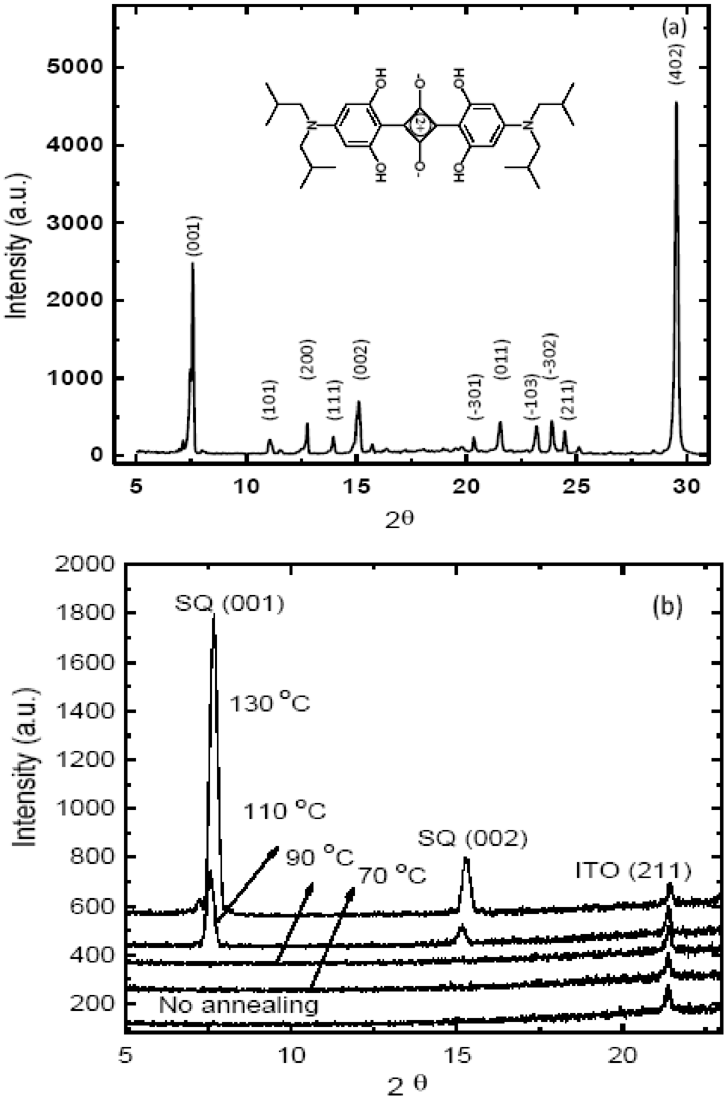

Figure 2.1:(a) X-ray-diffraction (XRD) patterns of squaraine (SQ) bulk powder materials; (b) SQ thin film spin-coated from dichloromethane solvent on indium tin oxide (ITO) coated glass substrates. The diffraction peaks are indexed using Winplotr and FullProf [17-18] software routines.

2.3.2 Optical absorption of squaraine and squaraine:$PC_{70}BM$ blend films

The thicknesses of the five blends from 3:1 to 1:6 SQ:$PC_{70}BM$ cast from 20 mg/ml solutions in chloroform, as determined by using Woolam VASE ellipsometer, were 1660 Å, 1530 Å, 720Å, 730 Å and 760 Å, respectively. The absorption spectra of the pure and blended films on quartz substrates with various compositions were measured using a Perkin Elmer Lambda 1500 UV-NIR spectrometer.

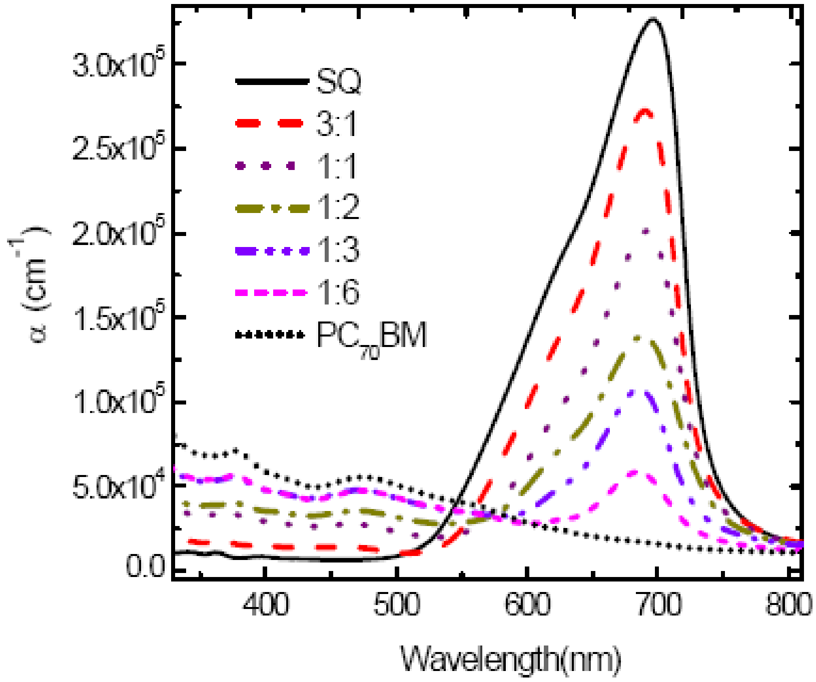

Figure 2.2:The absorption coefficient (α) of pure squaraine, $PC_{70}BM$, and blends of both materials on quartz substrate with SQ:$PC_{70}BM$ ratios of 3:1, 1:1, 1:2, 1:3 and 1:6.

The absorption spectra of pure SQ and blends of SQ:$PC_{70}BM$ films on quartz substrates are shown in Fig. 2.2. The SQ absorption extends to wavelengths of λ=750 nm with a peak at λ=680 nm. When mixed with $PC_{70}BM$ with absorption centered at λ=375 nm and λ=465 nm, the resulting film has spectral coverage across the visible spectrum. As the fraction of $PC_{70}BM$ increases, the SQ absorption peak is suppressed, with a concomitant increase in absorption from λ=300 nm to λ=500 nm, characteristic of $PC_{70}BM$.

2.3.3 Charge carrier mobilities

We plot the *J-V* characterisitcs of a hole-only device with a 1:1 SQ:$PC_{70}BM$ blend, with the top cathode biased positive with respect to the anode (Fig.2.3(a)). The data follow $J \propto V^2$, and hence are fit to a trap-free space charge limited model [19] to extract the zero-field hole mobility (μ_o), as shown. Here, μ_o decreases from 1×10^{-5} cm^2 /V-s to 1.2×10^{-7} cm^2 /V-s when the molecular weight percentage of SQ decreases from 100% (pure SQ thin films) to 28% (Fig.2.3(b)). A minimum of 4×10^{-8} cm^2/V-s is obtained for a 1:3 mixture (corresponding to 42 wt% SQ in $PC_{70}BM$). With the exception of the 100% SQ control device, the lowest mobility is obtained for the1:3 SQ:$PC_{70}BM$ films.

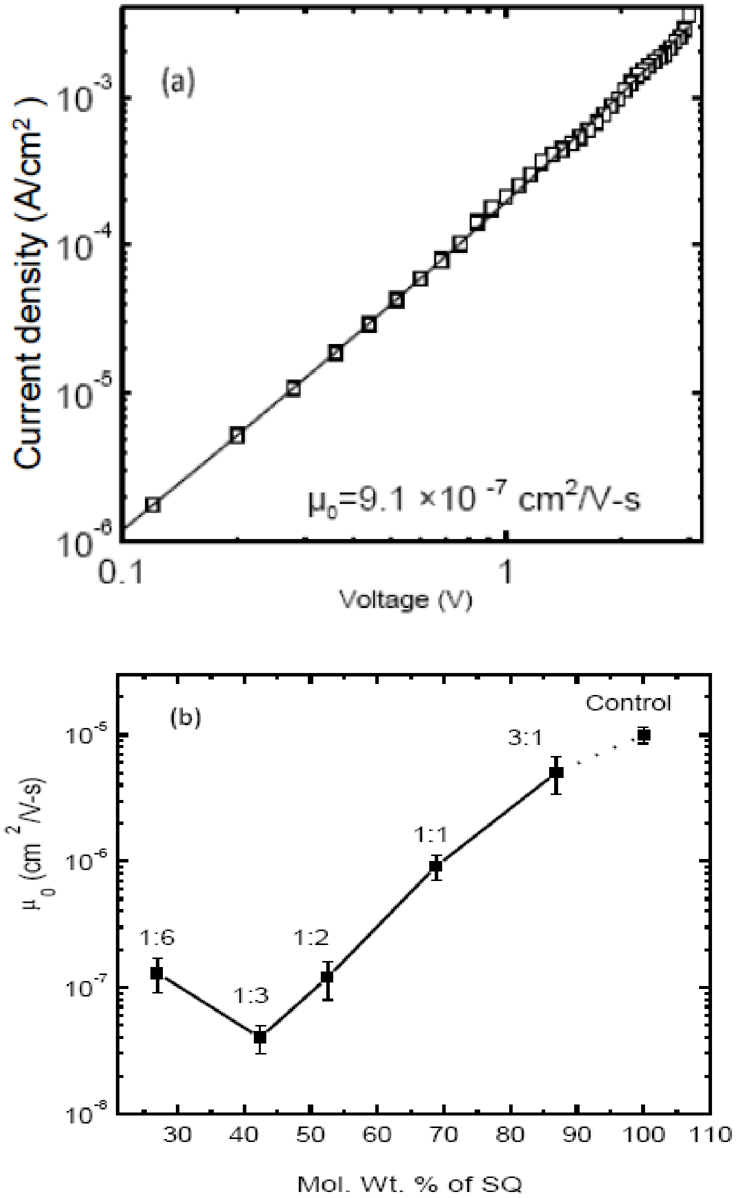

Figure 2.3: (a) Typical current density vs voltage characteristic of samples used for mobility measurement; (b) The zero field hole hole mobility (μ_0) versus molecular weight ratio between squaraine and PC$_{70}$BM.

2.3.4 Surface morphology

Examination of the AFM images of the pure SQ, pure PC$_{70}$BM and their blended films as deposited on 80Å thick MoO$_3$ buffer layers shown in Fig. 2.4.(Fig. 2.3). While the pure, nanocrystalline SQ film of a 5μm x 5μm surface area sample is rough (Fig. 2.4(c)), with a root-mean-square (RMS) roughness of 1.7 ± 0.02 nm, those containing neat PC$_{70}$BM are very smooth with a RMS of only 0.55 ± 0.04 nm (Fig. 2.4a).

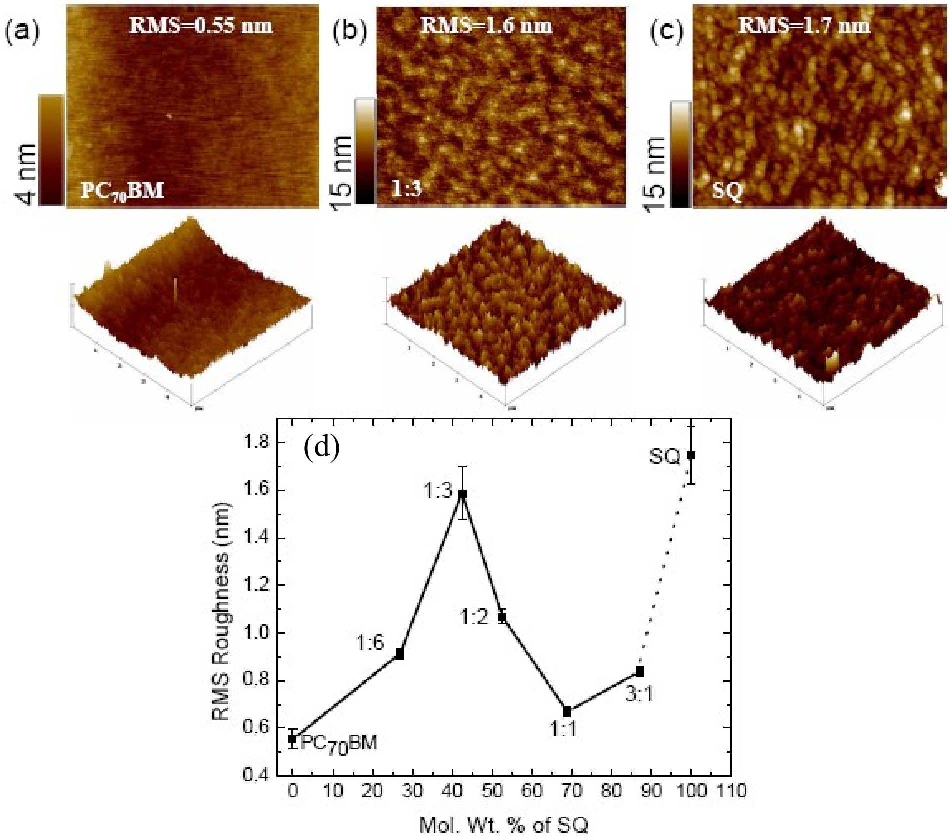

Figure 2.4:Atomic force microscope topographic and 3D images of (a) and pure PC$_{70}$BM, (b) 1:3 SQ:PC$_{70}$BM, and (c) pure SQ films deposited on indium tin oxide coated glass. The field of view of each film is 5 μm x 5 μm. (d) The root-mean-square (RMS) roughness of versus the molecular weight ratio of squaraine blended into PC$_{70}$BM taken from AFM data as shown in (a)-(c).

The active layer roughness of five blends for the ratios of 3:1, 1:1, 1:2, 1:3 and 1:6 are plotted in Fig. 2.4(d), and indicate a surface sufficiently smooth to fabricate devices with films free of pinholes and other macroscopic defects. At lower SQ concentrations (or higher $PC_{70}BM$ concentration), the decreased roughness of <0.8 nm indicates amorphous SQ clusters that are likely separated by intervening $PC_{70}BM$. The separate domains of SQ phase in a matrix of $PC_{70}BM$ phase can be recognized in the 3D image in Fig. 2.4(b) for a 1:3 SQ:$PC_{70}BM$ blend. The tendency of SQ to aggregate leads to a surface with a roughness of 1.6 ± 0.1 nm. Note that at this concentration, the hole mobility has a minimum value of 4×10^{-8} cm^2/V-s (Fig. 2.3), indicating a nonuniform distribution of SQ domains throughout the blend. Thus, the roughest films have the lowest mobility, suggesting that film nanomorphology can control this material characteristic.

2.4 Squaraine/C_{60} control and squaraine:$PC_{70}BM$ bulk solar cells

The *EQE* (Fig. 2.5) and *J-V* (Fig. 2.6) characteristics of the blended and control solar cells are summarized in Table 2.1. The addition of $PC_{70}BM$ broadens the spectral response of the cells into the wavelength range from λ=450 nm to 600 nm. The 3:1 and 1:1 blend film devices shows *EQE* < 22% at the absorption peak of SQ, increasing to 48% at λ=385 nm (due to $PC_{70}BM$) for a 1:6 mixture. Comparison with the absorption characteristics in Fig. 2.2 indicate that the relative balance between the *EQE* due to SQ and $PC_{70}BM$ absorption in the mixed cells suggests that charge collection, and not exciton dissociation, governs cell performance.

Table 2.1: Summary of solar cell characteristics of different SQ:PC$_{70}$BM blend ratios and a SQ/C$_{60}$ planar control cell.

SQ:PC$_{70}$ BM Ratio	V_{oc} (V)	J_{SC} (mA/cm^{2})	FF	J_o (mA/cm^{2})	η_p (%) at P_o=1 sun	η_p (%) (max.)
3:1	0.68(±0.03)	1.79(±0.19)	0.26(±0.01)	2.8×10^{-2}	0.32(±0.01)	0.32(±0.01)
1:1	0.81(±0.01)	3.61(±0.03)	0.31(±0.01)	1.1×10^{-2}	0.90(±0.01)	0.90(±0.01)
1:2	0.87(±0.01)	8.33(±0.50)	0.29(±0.01)	3.7×10^{-7}	2.1 (±0.1)	4.1(±0.2)
1:3	0.84(±0.01)	8.83(±0.34)	0.33(±0.01)	8.7×10^{-6}	2.4 (±0.1)	3.0(±0. 1)
1:6	0.89(±0.01)	8.85(±0.22)	0.35(±0.01)	6.2×10^{-7}	2.7 (±0.1)	3.3(±0. 1)
SQ:PC$_{60}$ BM 1:6	0.78(±0.01)	9.17(±0.25)	0.42(±0.01)	1.6×10^{-5}	3.0 (±0.1)	3.6(±0.1)
SQ/C$_{60}$	0.79(±0.01)	8.90(±0.25)	0.54(±0.02)	1.2×10^{-6}	3.8 (±0.2)	4.1(±0.2)
SQ/C$_{70}$	0.72(±0.01)	8.29(±0.25)	0.45(±0.02)	1.1×10^{-5}	2.7 (±0.2)	3.1(±0.2)

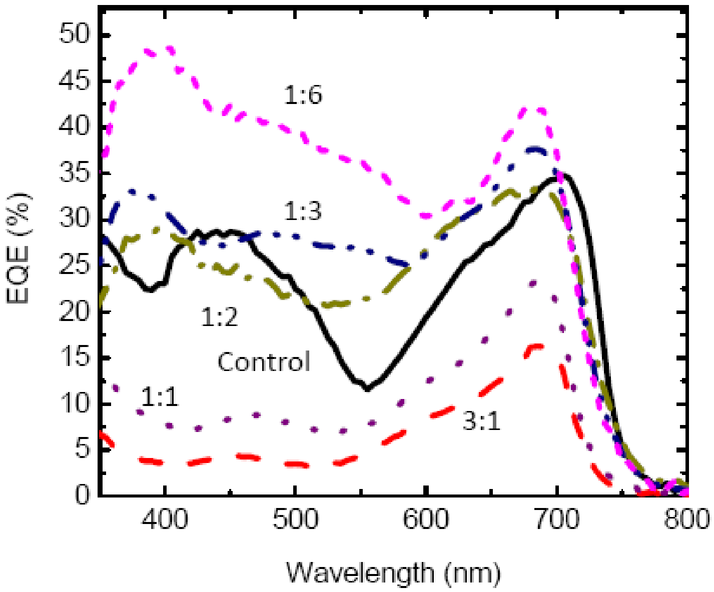

Figure 2.5:The effect of SQ:$PC_{70}BM$ blend ratios on the external quantum efficiency (*EQE*) for the five bulk cells with a device structure of ITO/MoO3(80 Å) /SQ:PC70BM(x Å)/Al (1000 Å), and the EQE of the SQ/C_{60} planar control cell with a device structure of ITO/MoO3(80 Å)/SQ(62 Å)/C_{60}(400 Å)/ bathocuproine (BCP)(100 Å)/Al(1000 Å). Here, x = 320 Å, 400 Å, 720 Å, 730 Å and 760 Å for the five blend cells.

In Fig 2.6, we show the *J-V* characteristics at very low (Fig. 2.6(a)) and at 1 sun intensity (Fig. 2.6(b)) AM1.5G illumination. At the higher intensities, we find that V_{oc} ranges from 0.75 V to 0.90 V as shown in Fig. 2.6(b), with the higher values corresponding to cells with a low *FF*. Hence, the largest open circuits are due, in part to the higher resistance of the cells. Nevertheless, these V_{oc} are consistently higher than previously reported 0.62 V for the SQ:$PC_{60}BM$ bulk cells [11], as a result of the lower saturation dark current, J_o, of our MoO_3 based cells.

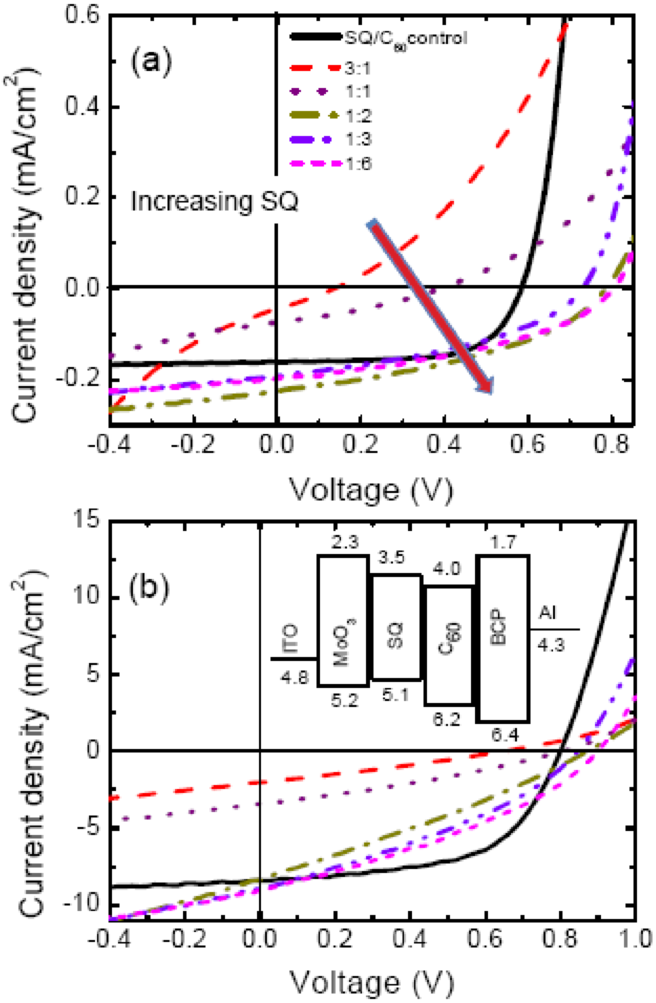

Figure 2.6: Current density-Voltage (*J*-*V*) characteristics characteristics illuminated at (a) 0.02 sun; (b) 1 sun for the SQ:PC$_{70}$BM blended bulk cells, and the SQ/C$_{60}$ planar control cell. Inset shows the energy level diagram of the SQ/C$_{60}$ control cell.

The open circuit voltage (V_{oc}) and fill factors (*FF*) of the solution processed solar cells are shown in Fig. 2.7, respectively. The incorporation of a MoO$_3$ buffer layer leads to a reduction in dark current arising from electron leakage to the anode [20], and hence a concomitant increase in V_{oc}. The SQ/C$_{60}$ control cells have the highest fill factor of *FF* =0.54 ± 0.02 at 1 sun intensity, compared to *FF*= 0.26 to 0.35 for the SQ:PC$_{70}$BM cells

(Table 2.1). Due to the low fill factor, the power conversion efficiency of the 1:6 SQ:PC$_{70}$BM cell drops from 3.0 ± 0.3 % with FF=0.38 ± 0.01 at 0.2 sun (20 mW/cm^2) AM1.5G illumination, to η_p=2.7 ± 0.1 % with FF=0.35 ± 0.01 at 1 sun. This is comparable to the SQ/C$_{70}$ planar cell, with η_p=2.7 ± 0.1 % and V_{oc}=0.72 ± 0.01 V and FF=0.45 ± 0.02 under similar illumination conditions. It is notable that the performance of both the 1:6 SQ:PC$_{70}$BM and SQ:PC$_{60}$BM cells are qualitatively similar, as apparent in Table 2.1. The somewhat reduced V_{oc} of the latter cell is due to the comparatively large J_o = 1.6×10^{-5} mA/cm^2, vs. 6.2×10^{-7} mA/cm^2 for the PC$_{70}$BM based cell.

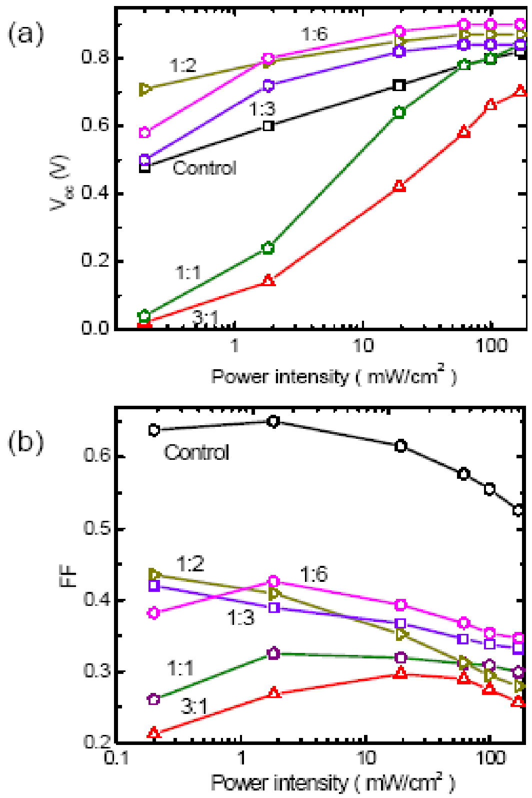

Figure 2.7: (a) Open circuit voltage (V_{oc}), and (b) fill factor (FF) as functions of AM1.5G spectral illumination power (corrected for solar spectral mismatch) of the five blended SQ:PC$_{70}$BM cells and the squaraine/C$_{60}$ planar control cell.

The highest efficiencies (Fig. 2.8) achieved are with the 1:2 blended films at low illumination intensity, and the planar SQ/C_{60} control device at 1 sun intensity, both peaking at 4.1 ± 0.2 %. As in the case of the 1:6 blended cell, the 1:2 cell efficiency falls off sharply with light intensity, along with a concomitant decrease in *FF* (Fig. 2.7b). In contrast, the unblended, planar control with its relatively high and intensity-independent *FF* shows only a weak efficiency dependence as intensity is varied from 0.01 to 2 suns.

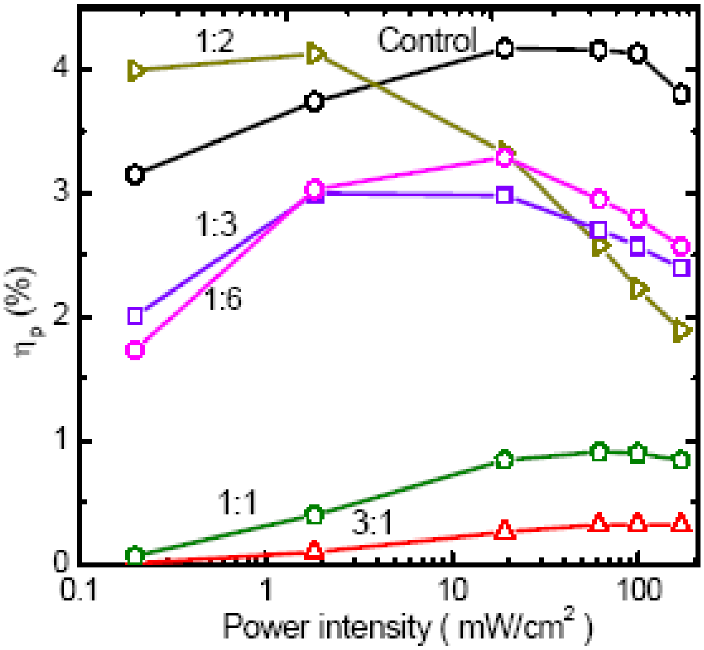

Figure 2.8: Power conversion efficiency (η_p) as a function of AM1.5G spectral illumination power (corrected for solar spectral mismatch) of the five blended SQ:$PC_{70}BM$ cells and the squaraine/C_{60} planar control cell. The highest efficiencies are 4.1 ± 0.2 % for the control (at 1 sun) and the 1:2 (at 0.02 suns) cells.

2.5 Discussion

The highest efficiencies are achieved for the planar SQ/C_{60} devices, where the SQ is both rough (Fig. 2.4(a)) and crystalline (Fig. 2.1, inset). In this case, the RMS roughness of 1.7 nm is characteristic of the crystallite size, and is on the order of an exciton diffusion length in such materials [21]. Hence, the rough interface between SQ and C_{60} forms a nanocrystalline BHJ similar to that previously demonstrated between CuPc and C_{60} grown by organic vapor phase deposition [10]. Note that the considerably lower efficiency obtained for the control SQ/C_{70} cell than for the SQ/C_{60} (Table 2.1) device may be due to lower purity of the C_{70}. This is also apparent due to its roll off in efficiency and fill factor at high intensities, indicative of high series resistance.

While exciton dissociation in uniform blends with high SQ content (e.g. 1:1 and 3:1) is expected to be efficient, the *EQE* of these devices are low, and the resulting solar cells are inefficient, particularly at light intensities >0.1 sun. These mixtures are characterized by discontinuous conducting pathways, as can be inferred from their low fill factors (Fig. 2.7b). We note, however, that the hole mobility for such mixtures is comparatively high. This suggests that SQ forms continuous conducting pathways for holes between anode and cathode in these particular mixtures. To test this assumption, we measured the parallel resistances of the PV cells by fitting their dark current vs. voltage characteristics to the modified ideal diode equation for organic heterojunctions:[24]

$$J = J_s[\exp(q(V - JR_s)/nk_BT) - \frac{k_{PPd}}{k_{PPd,eq}}] + \frac{V - JR_s}{R_p} \qquad (1.3)$$

Here, J_s is the reverse saturation current density, q is the electron charge, R_s is the series resistance, n is the ideality factor, k_B is the Boltzmann constant, T is the temperature, and R_p is the parallel (or shunt) resistance. For simplicity, the ratio of the polaron pair dissociation rate (k_{PPd}) to its equilibrium value ($k_{PPd,eq}$) is assumed to be 1. The resulting values for J_o and R_P are shown in Table 2.1 and Fig. 2.9, respectively, indicating that the films with large concentrations of SQ have a very low parallel resistance, consistent with the existence of shorts formed by percolating hole transport pathways. These pathways lead to very high J_o and hence suppressed V_{oc} as well.

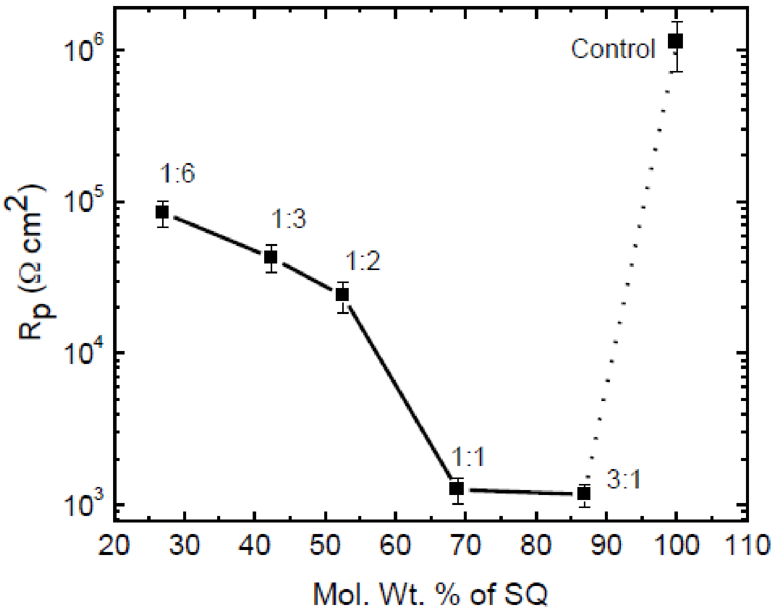

Figure 2.9: Parallel resistance (R_p) versus the molecular weight ratio between squaraine and $PC_{70}BM$. Also shown is the parallel resistance for the SQ/C_{60} control cell.

Photoelectron spectroscopy measurements indicate an ionization potential energy

(*IPE*) for SQ of 5.1 eV, compared to 6.2 eV for C_{60} (inset, Fig. 2.6b). Including the energy gap for C_{60} of $E_G(C_{60})$ = 2.2 eV, we obtain an interface gap between SQ and C_{60} of 1.1 eV. (Here, the interface energy gap is equal to $\Delta E_G = IPE(C_{60}) + E_G(C_{60}) - IPE(SQ)$.) While this is larger than the measured V_{oc}=0.9 V as shown in Fig. 2.6b for a cell with a 1:6 blend, the value is nevertheless considerably improved compared to that for the archetype CuPc/C_{60} cell, where ΔE_G= 1.3 eV vs. V_{oc}=0.55 V [23]. The high V_{oc} in the blended cells is due to their relatively large series resistance, which is clearly apparent in Fig. 2.6, which results in a low *FF* and a flattening of the *J-V* characteristics near *J*=0. Nevertheless, the V_{oc} of the low series resistance control is 0.79 eV, indicative of reduced recombination (and hence lower dark current) as compared to a conventional CuPc-based cell [23-25].

An increase of $PC_{70}BM$ concentration to 1:2, 1:3 and 1:6 increases the formation of electron conducting pathways to the cathode. This also reduces the probability for hole shunts formed by the SQ regions while increasing the interfacial area between donor and acceptor regions in the bulk heterojunction. While the surface roughness is relatively high in these mixtures, the improved bulk heterojunction morphology ultimately results in higher efficiencies, even at high illumination intensities. Note also that there is no significant increase of the *EQE* photoresponse contributed by the SQ donor (Fig. 2.5) at a wavelength of λ=685 nm for these bulk cells. In contrast, there is a doubling in the *EQE* photoresponse in the wavelength range from λ=350 nm to 600 nm, due to $PC_{70}BM$ absorption. As noted above, the relative balance in magnitude of *EQE* from both

$PC_{70}BM$ and SQ across the wavelength region from 350 nm to 750 nm compared to the absorption characteristics of these mixtures in Fig. 2.2 indicates that *carrier conduction* limits the cell response, while the mixtures support very efficient exciton diffusion and dissociation at the high surface area interface between donor and acceptor regions. This observation is supported by the relatively low *EQE* of the nanocrystalline SQ/C_{60} control cell, especially at short wavelengths where we expect that exciton dissociation, and not charge collection limits cell performance.

At $SQ:PC_{70}BM$ mixtures of 1:8 or larger, shorts are formed due to continuous conducting paths of this electron acceptor between anode and cathode. This sets an upper bound to the amount of $PC_{70}BM$ that can be used in the bulk heterojunction before it loses its nanoscale network that can efficiently dissociate excitons. Furthermore, none of the mixtures show a crystalline morphology, as indicated by the XRD patterns for thin film blends shown in Fig. 2.1. This lack of crystallinity is primarily responsible for the relatively low mobilities, and hence fill factors and power conversion efficiencies at high illumination intensities in these blended cells, in contrast to the homogeneous, planar SQ/C_{60} control devices [14].

Indeed, the high *FF* (0.54±0.02) of the SQ/C_{60} planar control cell results from its high hole mobility and hence high charge collection efficiency [26]. The lack of a continuous interpenetrating network of SQ domains in the blended cells ultimately limits their performance to less than that of the planar junction[27-28]. Therefore, further control of the nanoscale morphology and crystallinity in the $SQ:PC_{70}BM$ composites, possibly achieved by employing a higher annealing temperature, is required. However, given that the power efficiencies of the 1:2 bulk and planar junctions are similar at low intensities even though the *EQE* of the latter cell is higher, suggests that modification of the SQ molecules to form such morphologies is within reach, and may ultimately lead to power conversion efficiencies significantly in excess of 4% for these solution-processed junctions.

2.6 Summary

Using a combination of XRD, AFM, and measurements of hole mobilities in interpenetrating networks of SQ and $PC_{70}BM$, we have demonstrated a series of solution processed, small molecule SQ:$PC_{70}BM$ solar cells with various donor-to-acceptor constituent ratio. We find that the 1:2 SQ:$PC_{70}BM$ cells have peak efficiencies at low light levels of 4.1 ± 0.2 % (solar spectral mismatch corrected), which is comparable to that of the control, solution+vacuum deposited planar nanocrystalline SQ/C_{60} cells (4.1 ± 0.2 %). However, these latter structures maintain their high efficiency even at intensities exceeding 1 sun, AM1.5G simulated solar intensity.

We have shown that the performance of these cells is largely determined by the nanomorphology of the bulk heterojunctions formed during film deposition and subsequent annealing. The roll off in efficiency (which is due to a roll off in *FF*) at high intensities in the blends, but not observed in the planar junction control cells, arises from the formation of discontinuous pathways for electron and hole transport. However, the blended films have a more uniform and higher *EQE* than that of the planar device, suggesting that further control of the nanostructure, possibly using a modified SQ molecule with a higher potential for π−π stacking into a regular, crystalline structure, can result in increased efficiency at high illumination intensities.

References

[1] A. J. Janssen and N. S. Sariciftci, *MRS Bulletin* **30**, 33 (2005).

[2] J. K. J. Duren, X. N. Yang, J. Loos, C. W. T. Bulle-Lieuwma, A. B. Sieval, J. C. Hummelen, and R. A. Janssen, *Adv. Funct. Mater.* **14** (5), 425 (2004).

[3] D. Mühlbacher, M. Scharber, Morana, Z. G. Zhu, D. Waller, R. Gaudiana, and C. Brabec, *Adv. Mater.* **18**, 2884 (2006).

[4] G. Li, V. Shrotriya, J. Huang, Y. Yao, T. Moriarty, K. Emery, and Y. Yang, *Nature Mater.* **4**, 864 (2005).

[5] S. H. Park, A. Roy, S. Beaupré, S. Cho, N. Coates, J. S. Moon, D. Moses, M. Leclerc, K. Lee, and A. J. Heeger, *Nature Photonics* **3**, 297 (2009).

[6] M. Lenes, F. B. Kooistra, J. C. Hummelen, I. V. Severen, L. Lutsen, D. Vanderzande, T. J. Cleij, and P. W. M. Blom, *J. Appl. Phys.* **104**, 114517 (2008).

[7] A. J. Moulé and K. Meerholz, *Adv. Funct.Mater*. **19**, 1 (2009).

[8] M. T. Lioyd, J. E. Anthony and G. G. Malliaras, *Mater. Today* **10**, 34 (2007).

[9] P. Peumans, S. Uchida and S. R. Forrest, *Nature* **425**, 158(2003).

[10] F. Yang, K. Sun and S. R. Forrest, *Adv. Mater.* **19**, 4166 (2007).

[11] F. Silverstri, M. D. Irwin, L. Beverina, A. Facchetti, G. A. Pagani and T. J. Marks, *J. Am. Chem. Soc.* **130**, 17640 (2008).

[12] A. B. Tamayo, X. D. Dang, B. Walker, J.W. Seo, T.Kent, and T. Q. Nguyen, *Appl. Phys. Lett.* **94**, 103301 (2009).

[13] B. Walker, A. B. Tamayo, X. D. Dang, P. Zalar, J. H. Seo, A. Garcia, M.

Tantiwiwat, and T. Q. Nguyen, *Adv. Funct. Mater.* **19**, 3063 (2009).

[14] S.Y. Wang, E. I. Mayo, M. D. Perez, L. Griffe, G. D. Wei, P. I. Djurovich, S. R. Forrest, and M. E. Thompson, *Appl. Phys. Lett.* **94**, 233304 (2009).

[15] B. P. Rand, J. G. Xue, S. Uchida, and S. R. Forrest, *J. Appl. Phys.* **98**, 124902 (2005).

[16] V. Shrotriya, G. Li, Y. Yao, T. Morarty, K. Emery, and Y. Yang, *Adv. Funct. Mater.* **16**, 2016 (2006).

[17] A. L. Boultif and D. Louer, *J. Appl. Cryst.* **37**, 724 (2004).

[18] G. J. Ashwell, G. S. Bahra, C. R. Brown, D. G. Hamilton, C. H. L. Kennard, and D. E. Lynch, *J. Mater. Chem.* **6** (1), 23 (1996).

[19] M. A. Lamper and P. Mark, *Current injection in solids* (Academic Press, New York, 1970).

[20] N. Li, B. E. Lassiter, R. R. Lunt, G. D. Wei, and S. R. Forrest, *Appl. Phys. Lett.* **94**, 023307 (2009).

[21] R. R. Lunt, N. C. Giebink, A. A. Belak, J. B. Benziger, and S. R. Forrest, *J. Appl. Phys.* **105**, 053711 (2009).

[22] C. W. P. Schilinsky, J. Hauch, and C. J. Brabec, *J. Appl. Phys.* **95** (5), 023307 (2004).

[23] B. P. Rand, D. P. Burk, and S. R. Forrest, *Phys. Rev. B* **75**, 115327 (2007).

[24] N. C. Giebink, B. E. Lassiter, and S. R. Forrest, *MRS 2009 Fall Mtg*, Boston, MA (2009).

[25] M. D. Perez, C. Borek, S. R. Forrest, and M. E. Thompson, *J. Am. Chem. Soc.* **131**, 9281 (2009).

[26] P. Peumans and S. R. Forrest, *Chem. Phys. Lett.* **398**, 27 (2004).

[27] L. J. A. Koster, E. C. P. Smits, V. D. Mihailetchi, and P. W. M. Blom, *Phys. Rev. B* **72**, 085205 (2005).

[28] M. Lenes, M. Morana, C. J. Brabec, and P. W. M. Blom, *Adv. Funct. Mater.* **19**, 1106 (2009).

Chapter 3

Efficient and ordered squaraine/C_{60} nanocrystalline heterojunction solar cells

3.1 Introduction

Solution processed small molecule solar cells have been gaining interest [1-2], particularly for organic materials that are difficult to sublime in vacuum. For example, squaraine derivatives [3-4] and boron-subnaphthalocyanine [5] have been explored via solution processing as donor layers in bilayer (or planar) organic photovoltaic (OPV) cells. Also, 2,4-*bis* [4-(*N,N*-diisobutylamino)-2,6-dihydroxyphenyl] squaraine (SQ) dyes have been identified as efficient donors with photoactivities at wavelengths 750 nm>λ>550 nm, and with a potential for open circuit voltages (V_{oc}) greater than that of the commonly used donors such as copper phthalocyanine [6]. Compared to polymeric semiconductors, small molecules are monodisperse and hence are easy to purify, and can self-assemble into ordered domains resulting in relatively high charge carrier mobility and extended exciton diffusion lengths[2,7]. Indeed, device performance has been shown to be sensitive to domain size, and the morphologies of the constituents [8]. Polymer bulk heterojunction (BHJ) solar cells consisting of a mixture of donor and acceptor materials, leads to an increase in donor/acceptor junction interfacial area, but often results in increased series resistance [9]. In contrast, bilayer solar cells have continuous carrier transport pathways, but limited interface area[10]. While thermal [8] and solvent vapor annealing[11-12] have been explored for bulk heterojunction solar cells, the differences in these methods and their impact on crystalline morphology has not been thoroughly addressed. In this chapter, we show that post-annealing can improve the solution deposited, small molecule film crystallinity and roughness, thereby providing a route to the optimization leading from a planar to a BHJ architecture.

This work differs from previous reports of solution processed BHJs (c. f. Chapter 2), in that rather than using a homogeneous donor-acceptor mixture, we start with a pure donor film, then roughen it while also forming an extended crystal structure whose length scales are on the same order as the exction diffusion length. This is followed by the deposition of the C_{60} acceptor, resulting in a structure with complete donor-acceptor phase separation. This creates a low resistance, high efficiency, ordered BHJ[13-15].

3.2 Device fabrication and characterization

Squaraine thin films are spin-coated at 3000 RPM on precleaned indium tin oxide (ITO) [8] substrates, coated with a 80 Å thick layer of MoO_3 . Here, MoO_3 is thermally evaporated onto the ITO surface in a vacuum system with a base pressure of 10^{-7} Torr. The neat SQ thin films with thicknesses of 640 Å and 62 Å from 6 mg/ml and 1 mg/ml solutions, respectively, in dichloromethane (DCM) were annealed in nitrogen at temperatures ranging from 50 ^{0}C to 130 ^{0}C. The larger thickness samples were used for X-ray-diffraction (XRD) analysis using a 40 kV Cu K_{α} source, while the thinner, optimized samples were utilized in devices. For comparison to thermal annealing, SQ films were post-annealed in air for 20 min (or double that used in previous reports [3]) in a closed glass vial filled with 1 ml DCM. The thicknesses of the SQ films were determined using a variable angle and variable wavelength ellipsometer.

Solar cells were grown with the structure: ITO/MoO_3(80Å)/SQ(62Å)/C_{60}(400Å)/ bathocuproine (BCP) (100Å)/Al (1000Å). After spin-coating the SQ layer, the substrates were annealed and then transferred through a N_2 glove-box into a vacuum chamber (base pressure $<10^{-6}$ Torr) where C_{60}, BCP and the Al cathode were sequentially thermally deposited. The Al cathode was patterned by deposition through a shadow mask with an array of 1 mm diameter circular apertures. The current density-voltage (*J-V*) characteristics and η_p of the devices were measured using a solar simulator with AM1.5G filters and an NREL-calibrated Si detector. Solar spectral corrections were made using standard methods [19]. Values quoted for efficiencies are typical for the particular conditions used in fabrication, with the error bars indicating the standard deviation for that population both from device-to-device on a substrate fabricated in a given fabrication run, and from run-to-run. The external quantum efficiency (*EQE*) was measured using monochromatic light from a Xe lamp chopped at 400 Hz and focused on the device active area. For the exciton diffusion length (L_D) measurements [18], a 50 Å thick C_{60}, and a 50 Å thick BCP layer were deposited on the annealed SQ films to serve as exciton quenching and blocking layers, respectively. Excitation spectra in the L_D measurements were collected for each sample at a wavelength of λ=750nm, while emission spectra were collected with an excitation wavelength of λ= 600nm.

3.3 Properties of squaraine thin films

3.3.1 Crystallinity evolution through post annealing

X-ray data for the films annealed in nitrogen at 110 ^{0}C and 130 ^{0}C for 20 min and dichloromethane (DCM) vapor annealed in air are shown in Fig. 3.1 where diffraction peaks are observed at 2θ=7.62 ± 0.07^0 and 2θ=15.19 ± 0.05^0, corresponding to the (001) (d_{001}=11.60 ± 0.13Å) and (002) planes[3], respectively. Solvent annealed SQ films show the strongest (001) and (002) peak intensities, indicating an increase in crystalline content compared to that of as-cast or thermally annealed films. The mean crystal size of SQ annealed at 110 ^{0}C and 130 ^{0}C is estimated to be 39 ± 4 nm and 41 ± 2 nm, respectively, inferred from the X-ray peak broadening. Solvent annealing increases the mean crystallite size to 62 ± 3 nm. Thus, the thermal and solvent annealing processes have improved the molecular stacking of SQ molecules, grown into ordered domain.

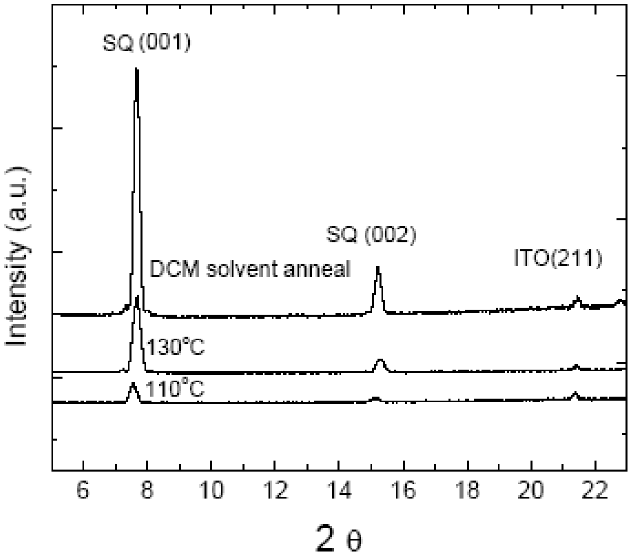

Figure 3.1:X-ray-diffraction patterns of squaraine (SQ) thin films spin-coated from

dichloromethane (DCM) solvent on indium tin oxide (ITO) coated glass substrates. The patterns suggest that the neat SQ film annealed at 110 ^{0}C and 130 ^{0}C and DCM annealed for 20 min, has (001) and (002) crystal axes oriented normal to the substrate plane.

3.3.2 Optical absorption of annealed squaraine films

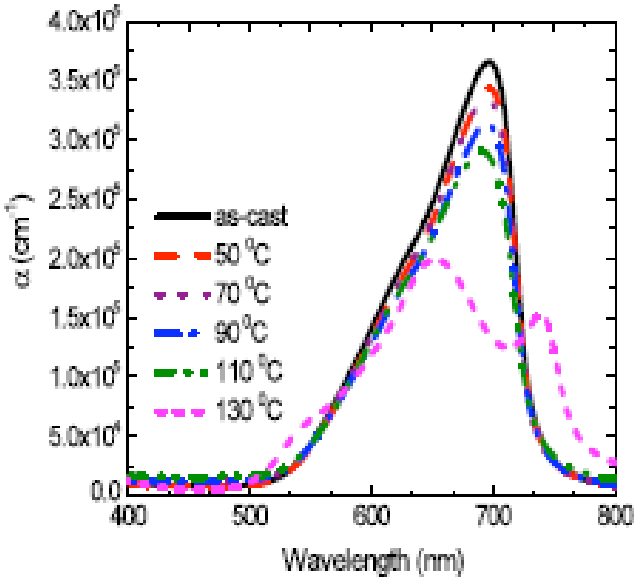

Figure 3.2: UV-Vis absorption spectra of squaraine thin films annealed at different temperatures: as-cast, 50 ^{0}C, 70 ^{0}C, 90 ^{0}C, 110 ^{0}C and 130 ^{0}C.

The absorption spectra of as-cast and thermally annealed SQ films are shown in Fig. 3.2. They exhibit a narrow and intense absorption band. The as-cast SQ film has a maximum at wavelengths of 700 nm, corresponding to peak absorption coefficients of 4.6×10^{5} cm^{-1}. There is a slight blue shift for the moderate thermally annealed SQ films when the annealing temperature is higher than 110 ^{o}C. While the parent SQ film has the sharpest peak, the 130 ^{o}C annealed film has the most broadened absorption coverage ranging from 500 nm to 800 nm, especially two absorption bands with a maximum at 630 nm and 740 nm evolves.

3.3.3 Surface morphology and crystallinity

While the as-cast SQ film has a root-mean-square (*RMS*) roughness of 0.9 ± 0.1 nm (Fig. 3.3(a)), the SQ film annealed at 110 ^{0}C shows crystalline features whose roughness is increased to 1.3 nm ± 0.2 nm (Fig. 3.3(c)). The SQ film after DCM solvent annealing is rougher still, with *RMS* =1.9 nm ± 0.2 nm (Fig. 3.3(e)).

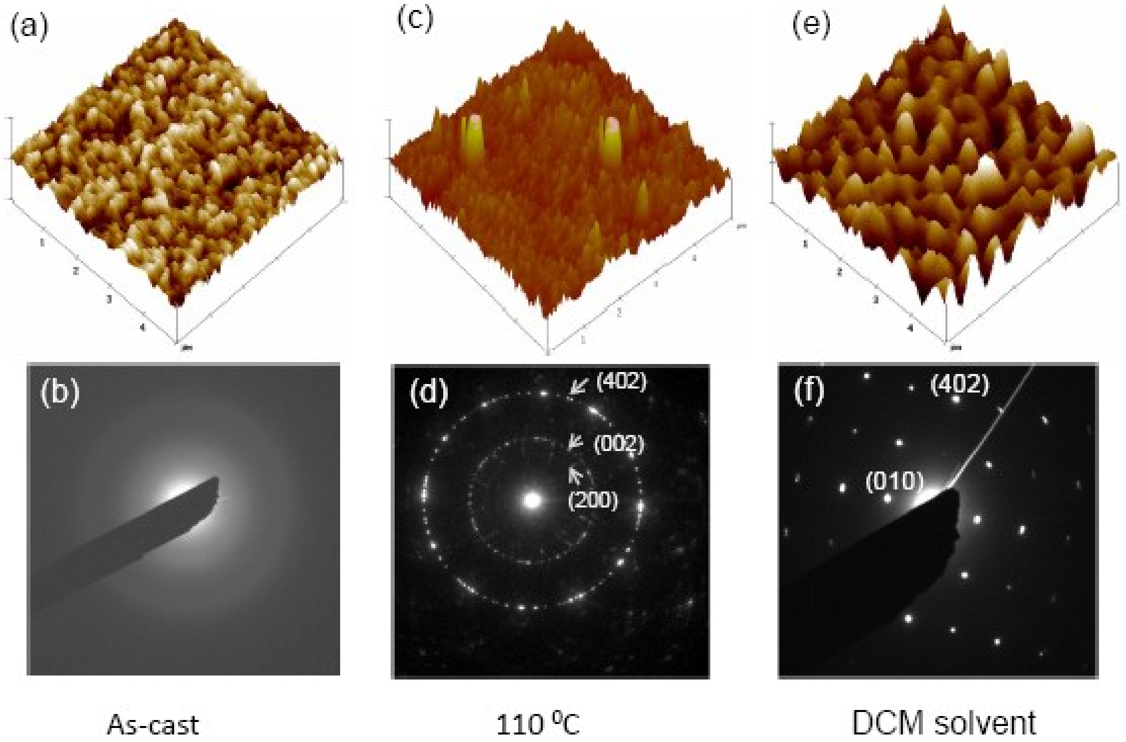

Figure 3.3: Atomic force microscope (AFM) images and selected-area electron diffraction (SAED) patterns of: (a), (b) as-cast; (c), (d) 110 ^{0}C; (e), (f) dichloromethane (DCM) solvent-annealed SQ films deposited on indium tin oxide (ITO) coated glass with a 80 Å thick layer of MoO_3. The three largest d-spacings, 7.49 Ǻ, 5.37 Ǻ and 3.13 Ǻ are shown in (d), which correspond to the (200), (002) and (402) reflections, respectively. The spots in (f) are indexed to (010) and (402) planes.

Selected-area electron diffraction (SAED) analysis in Fig. 3.3 is used to understand the local organization of SQ thin films prepared using these different processing methods. Fig. 3.3(b) shows a diffraction pattern of the as-cast SQ thin films in Fig. 3.3(a) that is characteristic of an amorphous layer. In contrast, for the spin-cast and thermally annealed (110 ^{0}C for 20 min) sample, a locally crystalline film is obtained, and the SAED pattern in Fig. 3.3(d), exhibits Debye-Scherrer ring patterns around the discrete SQ polycrystal diffraction spots. The diffraction rings are indexed as the (200), (002) and (402) reflections, corresponding to crystal spacings of 7.49 Å, 5.37 Å and 3.13 Å, respectively. A similar result is obtained for films annealed at 130 ^{0}C. Fig. 3(f) is a single crystal pattern taken from the solvent vapor annealed SQ film along the $[10\bar{2}]$ crystal direction with diffraction spots from SAED pattern indexed to (010) and (402) planes. It indicates the clusters apparent in the AFM image are SQ single crystals formed in the presence of the DCM vapor. Thus, the thermal annealing of amorphous as-cast SQ films provides a nanocrystalline morphology, which changes to large crystalline sizes achieved by solvent annealing.

3.3.4 Exciton diffusion length

The exciton diffusion length (L_D) of thermally and DCM solvent annealed SQ thin films was measured using spectrally resolved photoluminescence quenching[18]. Here, L_D of SQ thin films annealed at 130 ^{0}C is 1.6 ± 0.2 nm, which is similar to their roughness of RMS = 1.7 ± 0.2 nm. Increasing the crystallinity through solvent annealing leads to L_D = 5.0 ± 0.2 nm, which is three times larger than that of thermally annealed SQ thin films. However, the efficiency of solvent annealed films is not as high (η_p =1.8 ±

0.3 %) as for the polycrystalline films annealed at 110 ^{0}C due to excessive roughness that may lead to direct contact of the C_{60} with the MoO_3/ITO anode.

3.4 Device performance of squaraine/C_{60} bulk solar cells

External quantum efficiencies of the as-cast and thermally annealed solar cells are shown in Fig. 3.4. The *EQE* peak in Fig. 3.4(a) at λ=700 nm is due to SQ absorption, whereas the peaks centered at λ= 430 nm and 470 nm, result from C_{60} absorption. Note that the *EQE* in the C_{60} absorption region increases dramatically with annealing temperature, and its peak of 43 ± 1 % is significantly higher than 28% reported previously for cells with only 10 min annealing time [3].

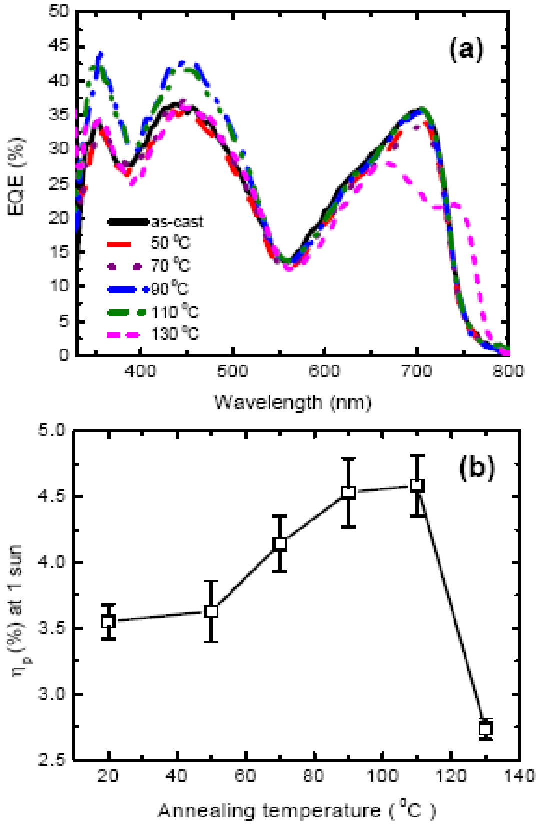

Figure 3.4: (a) External quantum efficiencies (*EQE*) of the control and five cells annealed at temperatures shown in legend; (b) The power conversion efficiency (η_p) versus annealing temperature at 1 sun, AM1.5G simulated illumination for a device structure of ITO/MoO3(80Å)/SQ(62Å)/C60(400Å)/bathocuproine (100 Å)/Al(1000 Å).

For the cell annealed at 130 ^{0}C, the double *EQE* peak centered at λ= 653 nm and λ=740 nm is consistent with aggregation (possibly corresponding to dimer absorption[16]) of the SQ molecules. Note that this double peak is also apparent in the SQ absorption spectrum as shown in Fig.3.2.

The power conversion efficiency at 1 sun is plotted as a function of annealing temperature in Fig.3.4b. Here, η_p=3.6 ± 0.1 % in the as-cast bilayer device (which is somewhat lower than that previously reported[3] of 3.8 ± 0.2 %) increases to a maximum of 4.6 ± 0.1% at an annealing temperature of 110 ^{0}C, and then decreases to 2.7 ± 0.1% at 130 ^{0}C due to the reduction in V_{oc} from 0.79 ± 0.02V to 0.46 ± 0.01V (these and other device performance characteristics are provided in Table 3.1), also presumably due to aggregate formation leading to a discontinuous SQ layer.

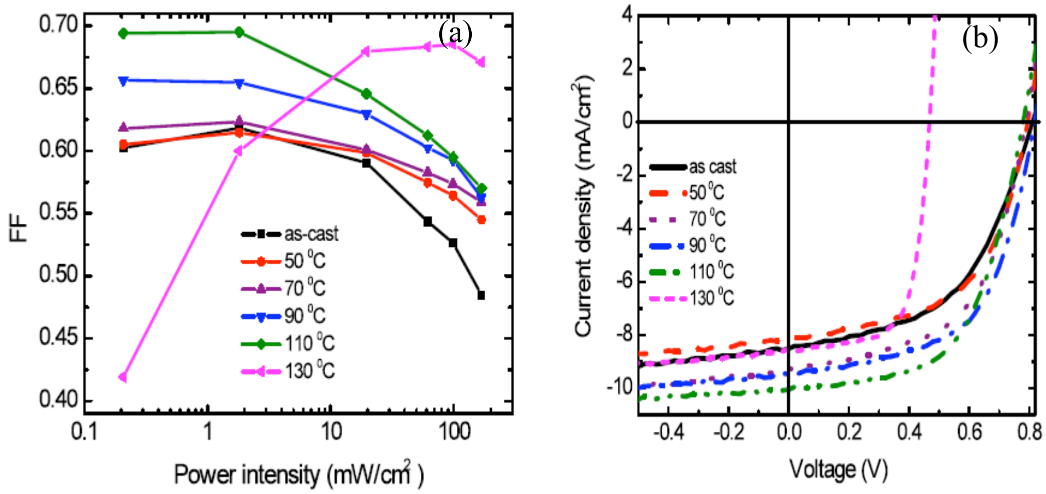

Figure 3.5: (a) fill factor (*FF*) as a function of AM 1.5 G spectral illumination power (corrected for solar spectral mismatch) of the control and five annealed cells; (b) the current density (*J*)-Voltage (*V*) characteristics of as-cast and annealed squaraine/C_{60} devices

The *FF* is found to roll off significantly at intensities approaching 1 sun as shown in Fig.3.5. Although the *FF* reaches 0.69 ± 0.01 at 0.02 sun intensity after thermal annealing at 110 ^{0}C, it drops to 0.60 ± 0.02 at 1 sun illumination (100 mW/cm^2). The roll-off feature of *FF* with increased power intensities here is caused by the series resistance (R_s) as high as 10.5 (±1.0) Ω·cm^2 (Table 3.1). Annealing up to 110 ^{0}C increases the *FF* across the range of power intensities. In contrast, annealing cells at 130 ^{0}C leads to an increase in *FF* from 0.42 ± 0.02 at 0.002 sun to 0.69 ± 0.01 at 1 sun (Table 3.1), although this increase is accompanied by an even greater differential drop in the open circuit voltage. The *J-V* curves at 1 sun illumination become more and more squared with the increase of the annealing temperature for the SQ/C_{60} devices shown in Fig. 3.6

Table 3.1**:** Summary of SQ/C_{60} solar cell characteristics under 1 sun, AM1.5G simulated illumination (solar spectrally corrected) and in the dark.

Annealing temperature (^{0}C)	V_{oc} (V)	J_{SC} (mA/cm^2)	*FF* P_o=1 sun	J_s (mA/cm^2)	R_S ($\Omega\cdot$cm^2)	η_p (%) at P_o=1 sun
As-cast	0.79(±0.02)	8.60(±0.19)	0.53(±0.01)	5.0×10^{-6}	32.5(±2.8)	3.6(±0.1)
50	0.78(±0.02)	8.26(±0.23)	0.56(±0.02)	3.5×10^{-6}	35.0(±3.5)	3.6(±0.2)
70	0.77(±0.01)	9.36(±0.30)	0.57(±0.01)	5.0×10^{-6}	20.2(±3.0)	4.1 (±0.2)
90	0.76(±0.01)	9.56(±0.34)	0.59(±0.01)	8.2×10^{-6}	17.1(±1.6)	4.5(±0.1)
110	0.76(±0.01)	10.16(±0.22)	0.60(±0.02)	8.5×10^{-6}	10.5(±1.0)	4.6 (±0.1)
130	0.46(±0.01)	8.63(±0.12)	0.69(±0.01)	2.5×10^{-4}	0.6(±0.1)	2.7 (±0.1)

While thermal annealing increases the crystallinity of SQ films spin-cast from DCM solution, it does not impact the order of SQ films deposited in vacuum. This indicates that the solution-cast SQ films precipitated from DCM solutions are far from thermodynamic equilibrium, possibly due to residual solvent remaining following the deposition process [17]. Thermal annealing leads to reorganization of the SQ clusters into stable nanocrystalline strucures. A slow and controlled solvent evaporation (so-called solvent assisted annealing) promotes the growth of the SQ nanocrystals into longer crystal grains.

3.5 Discussion

Moderate thermal annealling improves the crystallinity within the SQ network, and facilitates hole charge transport to the ITO anode. Additionally it increases the SQ surface roughness, thereby increasing the active junction area and folding it into a nearly ideal, interdigitated BHJ whose scale is on the order of the exciton diffusion length.

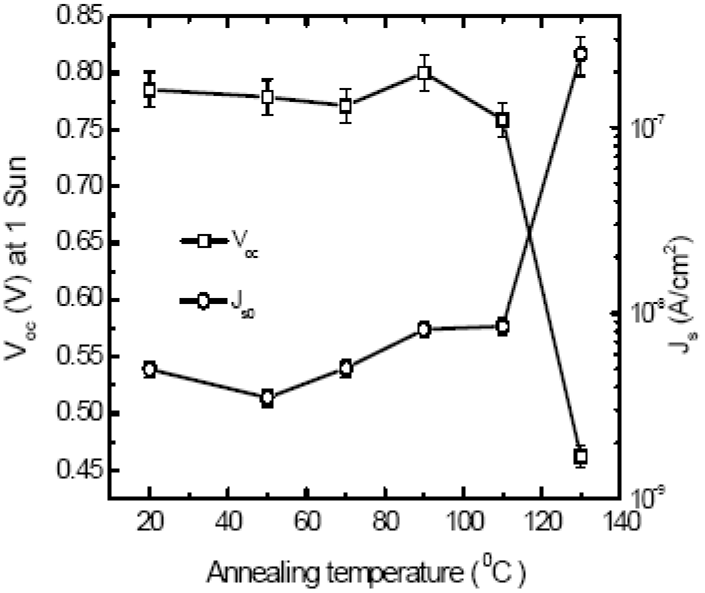

Figure 3.6: The dark current saturation current density (J_s) and open circuit voltage (V_{oc}) measured at 1 sun, AM1.5G illumination versus annealing temperature.

Though SQ has a short L_D of about 1.6 ± 0.2 nm for the thermal annealed SQ films, the interdigitated BHJ characteristics maximizes the interface between SQ and C_{60} within the photoactive layer to ensure efficient dissociation of the excitons, while typical dimensions of phase separation of SQ and C_{60} layers are within the exciton diffusion range and continuous pathways for transport of charge carriers to the electrode, resulting relatively high J_{sc}. The as-cast SQ/C_{60} cell has a series resistance of R_S=32.5 ± 2.8 $\Omega\cdot\text{cm}^2$ that decreases to 0.6 ± 0.1 $\Omega\cdot\text{cm}^2$ after annealing at 130 ^{0}C (Table 3.1), indicating that the introduction of crystalline regions in the SQ films increases conductivity, as expected. Indeed, the increased conductivity ensures for efficient hole transport across the crystalline layer, thereby enhancing charge collection due to excitons generated in the C_{60} layer. This is apparent due to the significant increase in *EQE* due to C_{60} absorption in the annealed films. However, the relatively short L_D limits the practical SQ layer thickness that can be utilized.

The reduction in R_S is consistent with the trends in *FF*, which increases from 0.53 ± 0.01 of as-cast cells to 0.69 ± 0.01 for 130 ^{0}C annealed cells measured at 1 sun intensity. Since *FF* is influenced by R_S, we infer that the annealing process significantly improves charge transport, as noted above. The V_{oc} remains larger than 0.76 ± 0.01 V with a thermal annealing temperature < 110 ^{0}C, and abruptly drops to 0.46 ± 0.01 V at 130 ^{0}C, as shown in Fig. 3.7. This change in V_{oc} is correlated to changes in the reverse saturation current density (J_s) obtained from the diode dark *J-V* characteristics [3]. An order of magnitude increase in J_s is found for cells annealed at 130 ^{0}C, indicating that roughness increases the leakage current in the diode, again due to the introduction of isolated regions where the C_{60} directly contacts the anode, thereby leading to a reduced V_{oc}.

3.6 Summary

In conclusion, we have shown that the performance of SQ/C_{60} photovoltaic cells is influenced by the morphology and crystallinity of the SQ film controlled via post-deposition annealing. The rough surface of the annealed SQ film is found to be on the scale of its exciton diffusion length, thereby leading to efficient exciton dissociation. The *FF* increases from 0.53 ± 0.01 to 0.69 ± 0.01, arising from the formation of crystalline SQ films and continuous hole transport pathways through post-annealing processes. The improved hole transport leads to a striking increase in *EQE* arising from absorption in the C_{60} layer. A solar power conversion efficiency of the SQ/C_{60} planar devices of η_p =4.6 ± 0.1 % at 1 sun, AM1.5G (correcting for solar mismatch) illumination is obtained for devices whose SQ layer is thermally annealed at 110 ^{0}C.

References

[1] D. Bagnis, L. Beverina, H. Huang, F. Silvestri, Y. Yao, H. Yan, G. A. Pagani, T. J. Marks, and A. Facchetti *J.Am. Chem. Soc.* **132**, 4074(2010).

[2] B. Walker, A. B. Tamayo, X. D. Dang, P. Zalar, J. H. Seo, A. Garcia, M. Tantiwiwat, and T. Q. Nguyen, *Adv. Func. Mater.* **19**, 3063(2009).

[3] G. D. Wei, S. Y. Wang, K. Renshaw, M. E. Thompson, and S. R. Forrest, *ACS Nano* **4**, 1927(2010).

[4] B. Fan, Y. Maniglio, M. Simeunovic, S. Kuster, T. Geiger, R. Hany, and F. Nuesch, *International Journal of Photoenergy*, **1**, (2009).

[5] B. W. Ma, C. H. Woo, Y. Miyamoto, and J. M. J. Fréchet, *Chem. Mater.* **21**, 1413(2009).

[6] S. Y. Wang, E. I. Mayo, M. D. Perez, L. Griffe, G. D. Wei, P. I. Djurovich, S. R. Forrest and M. E. Thompson, *Appl. Phys. Lett.* **94**, 233304(2009).

[7] M. T. Lioyd, J. E. Anthony, and G. G. Malliaras, *Mater. Today* **10**,34(2007).

[8] P. Peumans, S. Uchida, and S. R. Forrest *Nature*, **425**, 158(2003).

[9] J. Jo, S. I. Na, S. S. Kim, T. W. Lee, Y. S. Chung, S. J. Kang, D. Vak, and D. Y. Kim, *Adv. Funct. Mater.* **19**, 2398(2009).

[10] P. Peumans and S. R. Forrest, *Chem. Phys. Lett.* **398**, 27(2004).

[11] C. S. Kim, L. L. T., B. F. DiSalle, E. D. Gomez, S. Lee, S. Bernhard, and Y. L. Loo, *Adv. Mater.* **21**, 3110(2009).

[12] T. A. Bull, L. S. C. Pingree, S. A. Jenekhe, D. S. Ginger, and C. K. Luscombe,

ACS Nano **3**, 627(2009).

[13] F. Yang, K. Sun, and S. R. Forrest, *Adv. Mater.* **19**, 4166(2007).

[14] N. Li and S. R. Forrest, *Appl. Phys. Lett.*, **95**, 123309(2009).

[15] F. Yang, M. Shtein, and S. R. Forrest, *Nature Mater.* **4**, 37(2004).

[16] R. W. Chambers, T. Kajiwara, and D. R. Kearns, *The Journal of Physical Chemistry.* **4**, 380(1974).

[17] H. Meng, J. Zeng, A. J. Lovinger, B. C. Wang, P. G. Van Patten, and Z. N. Bao, *Chem. Mater.* **15**, 1778(2003).

[18] R. R. Lunt, N. C. Giebink, A. A. Belak, J. B. Benziger, and S. R. Forrest, *J. Appl. Phys.*, **105**, 053711(2009).

[19] V. Shrotriya, G. Li, Y. Yao, T. Morarty, K. Emery, and Y. Yang, *Adv. Funct. Mater.*, **16**, 2016(2006).

Chapter 4

Solvent annealed nanocrystalline squaraine: $PC_{70}BM$ (1:6) solar cells

4.1 Introduction

Efficient bulk heterojunction (BHJ) solar cells are characterized by a large interface area between donor and acceptor materials that ensures efficient photogenerated exciton dissociation into free charge. The optimal scale of the phase separation between these consistuents is that of the exciton diffusion length (L_D), and the separated phases must be contiguous to all for low resistance charge transport pathways from the photosensitive region to the electrodes.[1-6] To realize such a BHJ nanostructure, techniques such as thermal [7] and solvent vapor annealing[8] have been demonstrated. The most successful processing protocols affect the aggregation and morphology in a predictable and controlled manner. In Chapter 3, we have shown that solution-processed squaraine (SQ), followed by vacuum thermally evaporated C_{60} donor/acceptor solar cells can have power conversion efficiencies of η_p=4.6 ± 0.1 % when they are fabricated into a lamellar device that is subsequently annealed at high temperature (110^{o}C).[9] It was found that the annealing roughens the SQ surface, thereby creating a highly folded BHJ interface with the C_{60}, thereby compensating for the very short exciton (1.6 ± 0.2 nm) diffusion length (L_D) characteristic of the SQ donor. Although L_D of SQ is very small, this deficiency is partially compensated by its high absorption coefficient compared to that of C_{60}. This motivates the use of SQ: fullerene blends, whereby the ratio of materials strongly favors that of the fullerene to take advantage of its large L_D and low absorption. In previous work (Chapter 2) this approach has been partially successful, with the highest external quantum efficiencies (*EQE*) under low intensity illumination of SQ:$PC_{70}BM$ (1:6) blends approaching 50% across the visible spectrum. Unfortunately, devices fabricated using such blends exhibited exceptionally low fill factors (*FF*~0.35) due to a large internal series resistance to charge extraction from the low density of SQ in the mixture. Hence, under standard simulated solar illumination conditions (100 mW/cm^2, AM1.5G spectrum), the efficiency was limited to only ~3% [10].

4.2 Effect of solvent annealing to squaraine:$PC_{70}BM$ (1:6) films

4.2.1 Crystallinity of solvent annealed squaraine:$PC_{70}BM$ blend films

Post annealing of SQ:$PC_{70}BM$ (1:6) blends entails the 6 min to 30 min exposure of the films to DCM vapors in a closed glass vial enclosed in an ultrahigh purity glove box at room temperature. In Fig. 4.1, the lack of X-ray diffraction (XRD) peak for as-deposited SQ:$PC_{70}BM$ films indicates an amorphous structure. In contrast, after annealing for 10 min, a peak appears at $2\theta=7.80 \pm 0.08^0$ that increases in intensity when the annealing time is extended to 30 min. This peak is the (001) reflection of SQ, corresponding to an intermolecular spacing of 11.26 ± 0.16 Å.

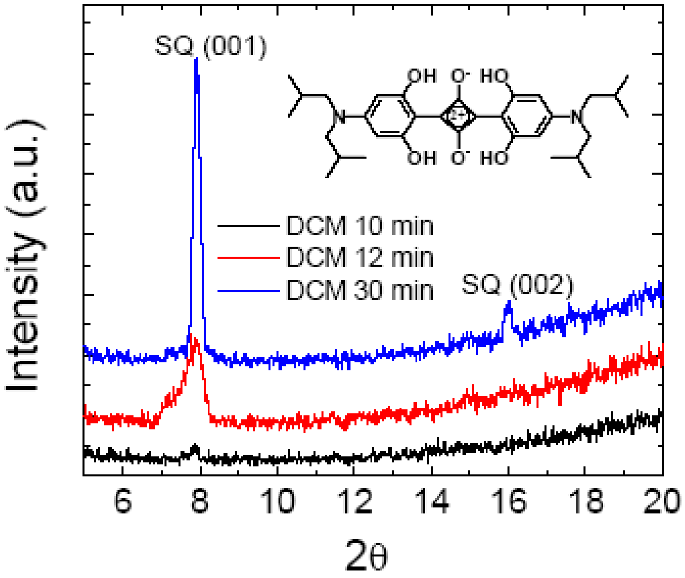

Figure 4.1:The XRD peaks for squaraine (SQ) :$PC_{70}BM$ (1:6) films annealed with dichloromethane (DCM) solvent for 10min, 12 min and 30 min.

After a 30 min exposure to DCM, a second peak corresponding to the (002) reflection appears, indicating a continued increase in order.[9] The mean crystal sizes of SQ in the blends annealed for 12 min and 30 min are estimated to be 2.0 ± 0.2 nm and 51 ± 4 nm, respectively, inferred from the XRD peak broadening using the Scherrer method.[15]

4.2.2 Optical properties of solvent annealed squaraine:$PC_{70}BM$ blend films

The spectra in the visible for the as-cast, and four DCM solvent-annealed SQ:$PC_{70}BM$ blended films on quartz substrates are shown in Fig. 4.1(a). The absorption coefficient of SQ throughout the entire observed spectral range increases with annealing time of up to 8 min, but as time is further increased, the change becomes saturated. Note also, that the crystalline blend film (DCM 12 min) has a less pronounced absorption peak at λ= 680 nm than in the amorphous films.

Now, the photoluminescence (PL) intensity of a film is quenched in the presence of photoinduced charge transfer of photogenerated excitons from a donor to an acceptor molecule. Therefore, efficient PL quenching in the SQ:PC$_{70}$BM blends indicates efficient exciton dissociation due to photogeneration within a distance, L_D, of an interface.[16-17] As above, the relevant length scales are 1.6 nm for SQ, and 20 nm to 40 nm for PC$_{70}$BM. In our experiments, a 10 min anneal results in a maximum PL intensity quenching, followed by a reduction in quenching as the annealing time is further increased. This is understood in terms of our values of L_D and mean crystallite size, δ. The PL quenching is strongest when $L_D \sim \delta \sim 2$ nm after approximately 10 -12 min annealing (Fig. 4.2b). Additional annealing leads to initiation of further phase segregation as the crystals, at which point $\delta >> L_D$, and hence the excitons are no longer efficiently transported to a dissociating heterointerface. [18]

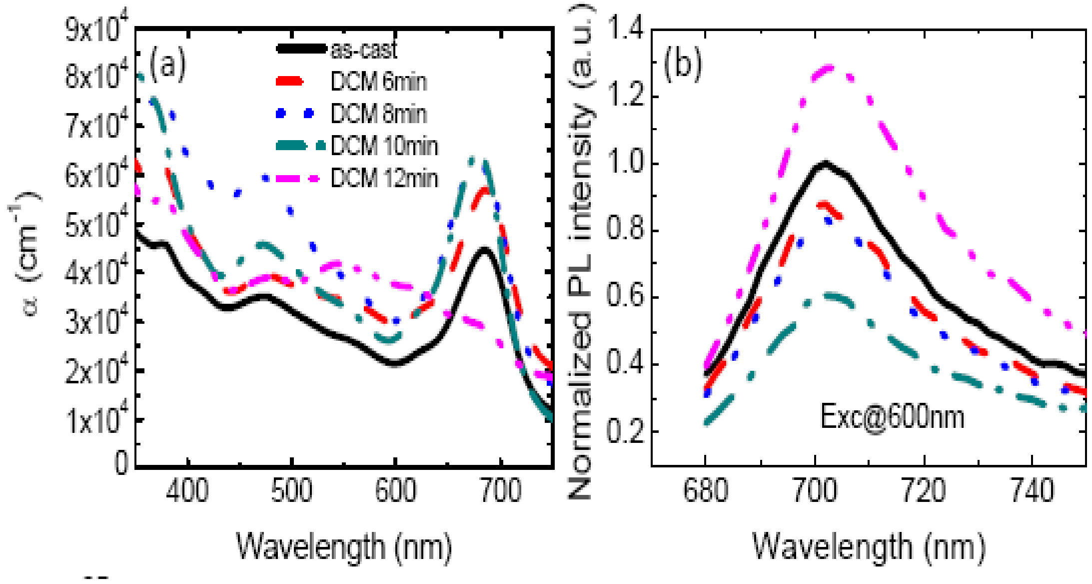

Figure 4.2: The effect of as-cast and four different (6 min, 8 min, 10 min and 12 min) dichloromethane (DCM) solvent annealing time on squaraine:$PC_{70}BM$ composite films with respect to (a) UV-vis absorption spectra, (b) photoluminescence (PL) spectrum

4.2.3 Surface morphology of squaraine:$PC_{70}BM$ blend films

The root-mean-square roughness obtained from the AFM images (Fig.4.3a) of the as-cast film is 0.8 ± 0.1 nm. In contrast, the roughness of the blend after 12 min solvent annealing increases to 8.4 ± 1.2 nm (Fig. 4.3b), indicating substantial roughening due to the polycrystalline growth of SQ in the mixture. With even longer annealing of 30 min, the phase separation of SQ and $PC_{70}BM$ continues, as indicated by further roughening to 12.0 ± 1.4 nm (Fig.4.3 c).The phase separation in nanoscale has also been obsvered in transmission electron microscope (TEM) image and surface phase image measured by AFM (the inset in Fig. 4.3(c)).

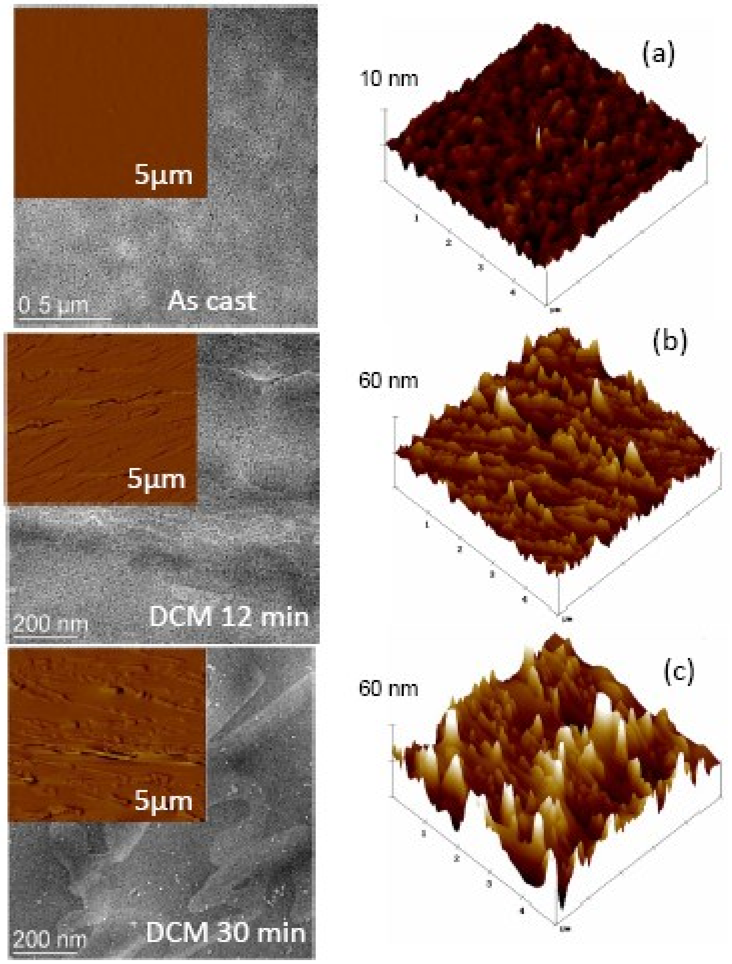

Figure 4.3: The effects of dichloromethane (DCM) solvent on film morphology. TEM and AFM images of squaraine (SQ):PC70BM (1:6) films: (a) as-cast, (b) DCM 12 min and (c) DCM 30 min. The inset shows the surface phase images measured by AFM.

The average crystal domain size also increases concomitant with the roughening, as noted above from the XRD line broadening. Thus, the change in the morphology of the blend films is strongly correlated with SQ phase evoluted from an amorphous to crystal phase. Note the SQ:$PC_{70}BM$ blend films after 12 min DCM solvent annealing have a shallow XRD peak intensity, indicating weak crystal feature of SQ. Correspondingly, the

TEM image shown in Fig. 4.3c is hard to discern the crystallite shape as well as size of SQ phases, even these two components of SQ and $PC_{70}BM$ complicates things in terms of distinguishing each material. So far, the XRD is the only quantitative way to calculate the crystal size of SQ phase.

4.3 Device performance of squaraine:PC70BM cells

The *EQE* of the as-cast and solvent annealed solar cells in Fig. 4.4(a) indicates a similarly broad spectral response as the absorption spectrum, extending from a wavelength of $\lambda = 300$ nm to $\lambda = 750$ nm. The *EQE* peak of SQ increases from 26 ± 2 % (as-cast) to 60 ± 1 % (annealed for 10 min). After a 12 min anneal, the peak *EQE* is reduced to < 40% across the entire wavelength range. These results, directly analogous to those obtained in absorption, further indicate that the cell efficiency depends strongly on crystallite size, with the optimum size comparable to L_D , thereby leading to maximum exciton diffusion to the dissociating donor/acceptor interface between SQ and $PC_{70}BM$.

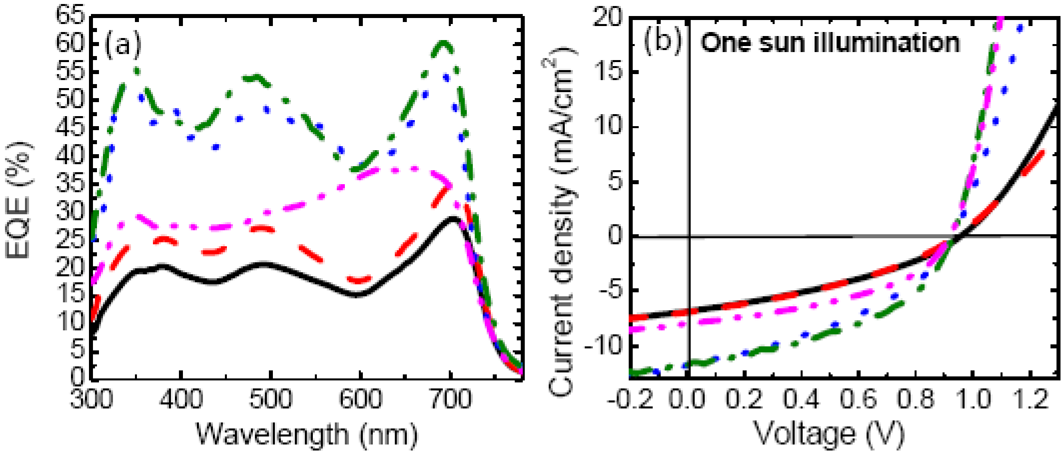

Figure 4.4: (a) External quantum efficiencies (*EQE*) and (b) the *J*-*V* characteristics of the SQ:PC$_{70}$BM (1:6) cells at 1 sun illumination.

The *J*-*V* characteristics in Fig. 4.4 (b) measured under 1 sun, AM1.5G simiulated solar emission, indicate that the short circuit current density (J_{sc}) is substantially enhanced from 6.9 mA/cm^2 (as-cast) to 12.0 mA/cm^2 (10 min solvent anneal), and then decreases to 8.3 mA/cm^2 after 12 min exposure to DCM. The *FF* shows a similar dependence on annealing time, indicating that the extended order decreases the series resistance, as anticipated for crystalline organic materials with improved molecular packing. Fitting the forward *J*-*V* curves using the modified diode equation [10] yields the specific series resistance, R_{SA}. The as-cast cell has R_{SA}=35.2 ± 1.0 Ω·cm^2, then gradually reduces to 5.0 ± 0.5 Ω·cm^2 when the annealing time is 12 min. Thus, the solvent annealing process has reduced the resistance, improving the charge transport and collection. However, further increase of DCM annealing time increases the density of pinholes between active layer and the contacts, leading to shorted diodes.

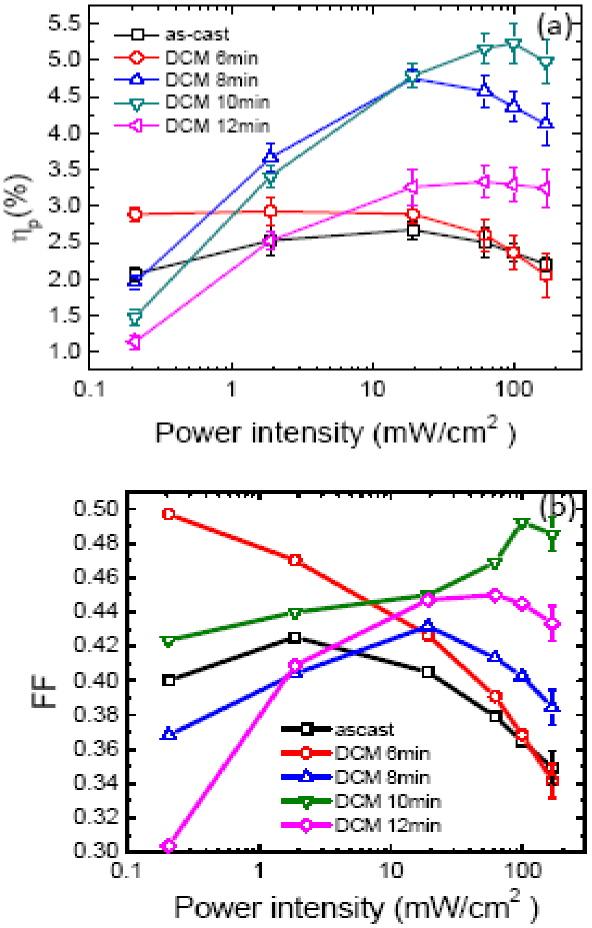

Figure 4.5:The power conversion efficiency (η_p) and (b) fill factor (*FF*) versus power intensities under as-cast and four different dichloromethane (DCM) solvent annealing time (6min, 8 min, 10 min and 12 min) for a device structure of ITO/MoO3(80 Å)/SQ:PC70BM (1:6 780 Å)/C60(40 Å)/BCP(10 Å)/LiF(8 Å)/Al(1000 Å).

Finally, the optical and electrical changes on annealing lead directly to an increase in η_p, as shown in Fig.4.5 a. Here, the as-cast cell η_p increases slightly with power intensity, then rolls off to 2.4 ± 0.1 % at 1 sun, along with a concomitant decrease in *FF* from 0.40 ± 0.02 (at 0.002 sun) to 0.36 ±0.01 (1 sun) (see Fig.4.5 b). In contrast, *FF* increases from 0.42 ± 0.01 (0.002 sun) to 0.50 ± 0.01 (1 sun), while η_p correspondingly increases from

1.5 ± 0.1 % to 5.2 ± 0.3 % (1 sun), with a peak measured value for a cell in this population of 5.5 % (J_{SC}=12.0 mA/cm^2, FF=0.5 and V_{oc}=0.92 V) the 10 min annealed cell. Finally, the η_p rolls off to 3.2 ± 0.1% with 12 min DCM annealing due to the reduced *EQE* and *FF*. Further energy tuned squaraine molecules with dicyanovinyl groups can extend the photon absorption to 900 nm and their J_{sc} as high as 12.6 mA/cm^2 in these squaraine:PCBM solar cells has been reached.[23]

4.4 Summary

In conclusion, DCM solvent annealing leads to control of the nanoscale phase separation of SQ:PC$_{70}$BM (1:6) organic films. Through optimizing morphology and molecular ordering of the SQ:PC$_{70}$BM (1:6) solar cells, a peak power conversion efficiency of 5.2 ± 0.3 % has been achieved in these blended structures, with a maximum cell performance achieved when the exciton diffusion length is approximately equal to the mean SQ crystallite size. This precise structural control takes advantage of the high absorption coefficient yet small diffusion length characteristic of this squaraine compound, allowing for only very dilute SQ:PC$_{70}$BM mixtures to result in high solar cell efficiency.

References

[1] P. Peumans, S. Uchida, and S. R. Forrest, *Nature* **425**, 158(2003).

[2] H. Hoppe and N. S. Sariciftci, *J. Mater. Chem.* **16**, 45(2006).

[3] B. Walker, A. B. Tamayo, X. D. Dang, P. Zalar, J. H. Seo, A. Garcia, M. Tantiwiwat and T. Q. Nguyen, *Adv.Func.Mater.***19**, 3063(2009).

[4] C. V. Hoven, X. D. Dang, R. C. Coffin, J. Peet, T. Q. Nguyen and G. C. Bazan, *Adv. Mater.* 22, 63(2010).

[5] M. C. Scharber, D. Wuhlbacker, M. Koppe, P. Denk, C. Waldauf and A. J. Heeger, C. L. Brabec. *Adv. Mater.* **18**, 789(2006).

[6] M. Campoy-Quilers, T. Ferenczi, T. Agostinelli, P.G. Etchegoin, Y. Kim, T. D. Anthopoulos, P. N. Stavrinou, D. D. C. Bradley and J. Nelson. *Nat. Mater.* **7**, 158(2008).

[7] W. L. Ma, C. Y. Yang, X. Gong, K. Lee and A. J. Heeger, *Adv. Func. Mater.* **15**, 1617(2005).

[8] G. D. Sharma, P. Suresh, S. S. Sharma, Y. K. Vijay and J. A. Mikroyannidis, *ACS Appl. Mater. Inter.* **2**, 504(2010).

[9] G. D. Wei, R. R. Lunt, K. Sun, S. Y. Wang, M. E. Thompson and S. R. Forrest, *Nano Letters* **10**, 3555(2010).

[10] G. D. Wei, S. Y. Wang, K. Renshaw, M. E. Thompson and S. R. Forrest, *ACS Nano* **4**, 1927(2010).

[11] Y. Yao, J. Hou, Z. Xu, G. Li, and Y. Yang, *Adv. Func. Mater.* **18**, 1783(2008).

[12] G. Li, V. Shrotriya, J. Huang, Y. Yao, Tommoriarty, K. Emery, and Y. Yang, *Nature Mater.* **4**, 864(2005).

[13] M. Morana, H. Azimi, G. Dennler, H. J. Egelhaaf, M. Scharber, K. Forberich, J. Hauch, R. Gaudiana, D. Waller, Z. Zhu, K. Hingerl, S. S. Bavel, J. Loos, and C. J. Brabec *Adv. Func. Mater.* **20**, 1180(2010).

[14] F. Silvestri, M. D. Irwin, L. Beverina, A. Facchetti, G. A. Pagani and T. J. Marks, *J. Am. Chem. Soc.* **130**, 17640(2008).

[15] T. Erb, U. Zhokhavets, G. Gobsch, S. Raleva, B. Stühn, P. Schilinsky, C. Waldauf and C. J. Brabec, *Adv. Funct. Mater.* **15**, 1193(2005).

[16] T. M. Clarke, A. M. Ballantyne, S. Tierney,M. Heeney, W. Duffy, I. McCulloch, J. Nelson and J. R. Durrant, *J. Phys. Chem. C* **114**, 8068(2010).

[17] J. S. Kim, Y. Park, D. Y. Lee, J. H. Lee, J. H. Park, J. K. Kim and K. Cho, *Adv. Func. Mater.* **20**, 540(2010).

[18] R. R. Lunt, J. B. Benziger, and S. R. Forrest. *Adv.Mater.***22**, 1233(2010).

[19] D. W. Sievers, V. Shrotriya, and Y.Yang, *J. of App. Phys.* **100**, 114509(2005).

[20] S. R. Forrest, *MRS Bulletin* **30(1)**, 28(2005).

[21] P. K. Watkins, A. B. Walker, and G. L. B. Verschoor, *Nano Letters* **5(9),**

1814(2005).

[22] V. Shrotriya, G. L., Y. Yao, T. Morarty, K. Emery, and Y. Yang, *Adv. Funct. Mater.* **16**, 2016(2006).

[23] U. Mayerhöffer, K. Deing, K. Gruβ, H. Braunschweig, K. Meerholz, and F. Würthner, *Angew. Chem. Int. Ed*. **48**, 8776(2009).

Chapter 5

Arylamine-Based Squaraine Donors for Use in Organic Solar Cells

5.1 Introduction

The development of new materials, nano-morphological control, and device design has led to significantly improved performance of organic solar cells over the last decade [1-6]. In general, strategies to improve organic solar cell efficiency include: (i) creating a donor/acceptor junction with very large surface area, (ii) choosing the energy gaps of donors and acceptors to enhance solar spectral coverage from the blue to the near infrared (NIR), leading to an increased short circuit current (J_{sc}); (iii) adjusting the highest occupied molecular orbital (HOMO) energy of the donors as well as reducing recombination at the donor/acceptor interface to increase the open circuit voltage (V_{oc}); and (iv) improving the charge transport by extending the crystalline domain size in phase-separated donors and acceptors to increase the fill factor (*FF*).

The bulk heterojunction (BHJ) is a particularly successful solar cell architecture that is characterized by a large donor/acceptor interface area that leads to efficient exciton harvesting while simultaneously permitting the use of a thick and absorptive photoactive layer.[7] An analogous structure useful primarily in small molecular weight materials systems is the nanocrystalline heterojunction (NcHJ) introduced by Yang, et al [8]. Like the BHJ, the NcHJ has a very large donor/acceptor interface area, in this case surrounded by interconnected crystalline regions of donors and acceptors formed through liquid [9], vacuum[10], or vapor phase [8] deposition processes. It has been shown that efficient exciton dissociation at these intertwined NcHJ networks that often lack islands or other morphological features that impede charge extraction can be achieved through solvent annealing[11], thermal annealing[7], or the use of additives[12-13]. To form the high surface area interface, the donor film surface is roughened by one or more of these techniques to form an extended structure whose length scales are on the order of the exciton diffusion length. This continuous donor layer is followed by blanket deposition of the acceptor, C_{60}, resulting in a stable and continuous nanocrystalline structure (Fig.5.1a) without islands, voids, or other morphological defects.

Squaraine dyes are notable for their exceptionally high absorption coefficients of ~3 $\times 10^5$ cm^{-1} and extending from the green to the near infrared[3,4,9]. In this work we use a donor based on the parent SQ: 2, 4-bis[4-(N, N-diisobutylamino)-2,6-dihydroxyphenyl] squaraine (SQ), but substitutes the sterically bulky isobutylamines with arylamines. This compound, 2, 4-bis[4-(N-phenyl-1-naphthylamino)-2,6-dihydroxyphenyl] squaraine (1-NPSQ, inset, Fig. 5.1b, employs naphthyl-functionalized end groups to increase π-stacking between donor molecules in the nanocrystalline network, thereby significantly improving the hole collection efficiency compared to the parent SQ which is sterically hindered from such close stacking [14]. The strong electron withdrawing arylamine also lowers the HOMO energy of 1-NPSQ to 5.3 eV compared to 5.1 eV for SQ [9], increasing the difference between the HOMO of the donor and the lowest unoccupied molecular orbital of the acceptor (the HOMO-LUMO interfacial gap energy, ΔE_{HL}), thereby leading to an increased V_{oc} [15,16]. Thermal annealing improves the 1-NPSQ crystallinity and roughens the interface between 1-NPSQ and C_{60}; as a result, optimized 1-NPSQ/C_{60} solar cells with a power conversion efficiency of η_p=5.7 ± 0.6% have been realized by a combination of a deep HOMO level (resulting in V_{oc}=0.90 ± 0.01 V), NIR absorption (leading to J_{sc}=10.0 ± 1.1 mA/cm^2), and increased hole conductivity (giving FF=0.64 ±0.01).

5.2 1-NPSQ/C_{60} device fabrication

Film preparation begins by dissolving 1-NPSQ in 1, 2-dichlorobenzene in a concentration of 4 mg/ml and stirred at 100 °C for approximately 10 hr prior to use. The 1-NPSQ solution was spin-coated on solvent and ultraviolet-ozone pre-cleaned indium tin oxide (ITO)-coated glass substrates (22 Ω/sq.). An 80 Å thick layer of MoO_3 is thermally evaporated onto the ITO surface in a vacuum system with a base pressure of 10^{-7} Torr.

The 1-NPSQ thin film is subsequently formed through a multiple spin-velocity coating processes: first, the spinner is set to 1000 rpm for 60 s, then to 3000 rpm for 60 s, and finishes by spinning at 6000 rpm for 60 s. The neat 1-NPSQ thin films with a thickness of 200 Å cast from 4 mg/ml solution were annealed in ultrahigh purity N_2 at temperatures ranging from 80^{o}C to 110^{o}C. For the control SQ/C_{60} cells, the SQ film with a thickness of 62 Å was spun-cast at 1000 rpm for 30 s from 1 mg/ml SQ/dichlorform (DCM) solution, stirring for 3 hr at room temperature prior to use. The thicknesses of the 1-NPSQ and SQ film were determined using a variable angle and wavelength ellipsometer. The molecular structure of SQ and 1-NPSQ is shown in Figure 5.1(b).

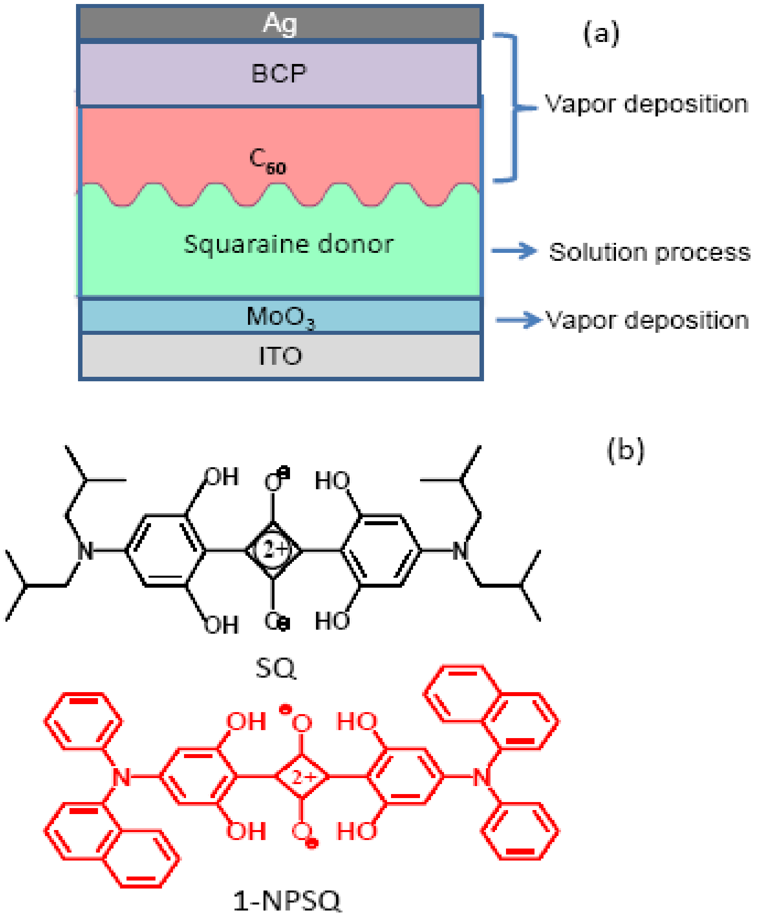

Figure 5.1:(a) the squaraine/C_{60} device architecture (b) the molecular structure of parent squaraine (SQ) and the arylamine-based squaraine (1-NPSQ).

Solar cells were grown with the structure: ITO/MoO_3(80Å)/1-NPSQ(200 Å)/C_{60}(400Å)/ bathocuproine (BCP) (100Å)/Ag (1000Å) and ITO/MoO_3(80Å)/SQ(62 Å)/C_{60}(400Å)/ BCP (100Å)/Ag (1000Å) (Fig. 5.1(a)). After spin-coating the 1-NPSQ and SQ layers, the substrates were annealed, and then transferred through an ultrahigh purity N_2 glove-box into a vacuum chamber (base pressure $<10^{-6}$ Torr) where C_{60}, BCP and the Ag cathode were sequentially thermally deposited. The Ag cathode was patterned by deposition through a shadow mask with an array of 1 mm diameter circular apertures.

5.3 Absorption spectra of SQ and 1-NPSQ thin films and device characteristics

Both SQ and 1-NPSQ thin films exhibit narrow and intense absorption bands with maxima at wavelengths of λ=700 nm and λ=710 nm (Fig. 5.2(a)), respectively. This corresponds to repsective peak absorption coefficients of 4.6×10^5 cm^{-1} and 4.0×10^5 cm^{-1}. Note that the 1-NPSQ absorption band persists to λ=810 nm, extending the spectral sensitivity further into the near infrared. Fig.5.2 (b) shows the current density (J)-voltage (V) characteristics of as-cast SQ/C$_{60}$ and 1-NPSQ/C$_{60}$ devices at 1 sun, AM1.5G spectrum illumination.

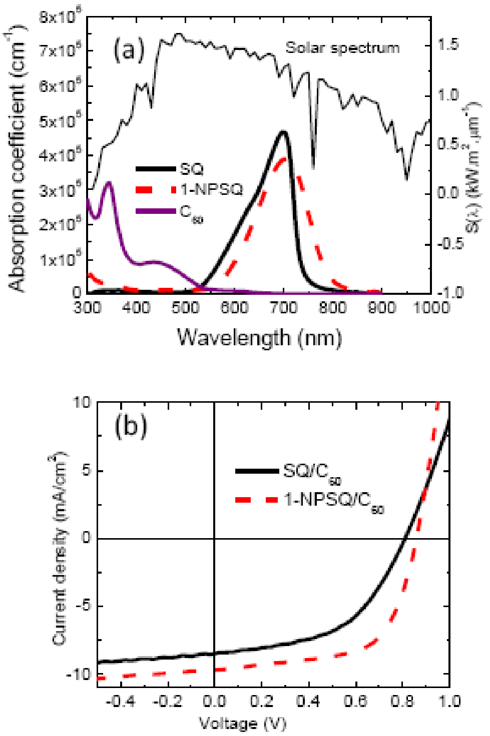

Figure 5.2: (a) absorption spectrum of SQ, 1-NPSQ and C$_{60}$, and standard solar spectrum at 1 sun illumination; (b) the current density (J)-voltage (V) of as-cast SQ/C$_{60}$ and 1-NPSQ/C$_{60}$ solar cells at 1 sun illumination.

A significant increase in V_{oc} is observed for the as-cast 1-NPSQ/C_{60} device, with V_{oc} = 0.84 ± 0.02 V consistent with the increased interfacial energy gap (ΔE_{HL} = 1.3 eV) between 1-NPSQ and C_{60}, compared with ΔE_{HL} = 1.1 eV for the SQ/C_{60} junctions.[15,16] The lowest unoccupied molecular orbital (LUMO) of 1-NPSQ is 3.7 eV and LUMO of C_{60} is 4.0 eV, thus forming an interface capable of efficient exciton dissociation. The LUMO energies were determined by measuring position of the low energy optical absorption tail, and subtracting that value from the HOMO energy.

Generally, the absorption coefficient of organic materials and optical interference within the multilayer structure determines the photon absorption and exciton generation profile. The resulting spatial distribution of excitons imposes an optimal thickness of donor materials. For the structures and materials in this comparison, the optimal active layer thicknesses of SQ and 1-NPSQ are 65 Å and 200 Å, respectively. The external quantum efficiency, *EQE* = 25% at λ=710 nm is due to 1-NPSQ absorption, whereas the peak at 42% centered at λ=470 nm results from excitons generated in C_{60}, as shown in Fig. 5.2(a). 1-NPSQ/C_{60} cells with thicker 1-NPSQ layers have response to λ=810 nm, but lower *EQE* peak in comparison with the SQ/C_{60} cells (*EQE*=35% at λ=700 nm corresponding to SQ absorption).[9] Combined with J_{sc}=8.7 ± 0.9 mA/cm^2 and *FF* =0.64 ± 0.02, we obtain η_p = 4.6 ± 0.5 % for the as-cast 1-NPSQ/C_{60} devices. This efficiency η_p is an increase of 28% over that obtained for analogous SQ/C_{60} cells (Table 5.1).

Table 5.1**:** Summary of SQ/C_{60} (control) and 1-NPSQ/C_{60} solar cell characteristics under 1 sun, AM1.5G simulated illumination (J_{sc} and η_p solar spectrally corrected) and in the dark.

Annealing temperature (°C)	V_{oc} (V)	J_{SC} (mA/cm^2)	FF P_0[a]	R_S ($\Omega\cdot$cm^2)	η_p (%) at P_0
As-cast(SQ)[12]	0.79(±0.02)	8.6(±0.2)	0.53(±0.01)	32.5(±2.8)	3.6(±0.1)
As-cast(1-NPSQ)	0.84(±0.02)	8.7(±0.9)	0.64(±0.02)	4.6(±0.8)	4.6(±0.5)
80	0.86(±0.01)	9.5(±1.0)	0.64(±0.01)	3.8(±1.2)	5.1 (±0.6)
90	0.90(±0.01)	10.0(±1.1)	0.64(±0.01)	4.2(±1.0)	5.7(±0.6)
110	0.87(±0.01)	8.6(±0.9)	0.61(±0.02)	5.9(±1.0)	4.6 (±0.5)

[a] P_0 is the incident power at 1 sun = 100 mW/cm^2 at AM1.5G spectral illumination

5.3 SQ/C_{60} and 1-NPSQ/C_{60} device characteristics

The external quantum efficiency, *EQE* = 25% at λ=710 nm is due to 1-NPSQ absorption, whereas the peak at 42% centered at λ=470 nm results from excitons generated in C_{60}, as shown in Fig.5.3a.

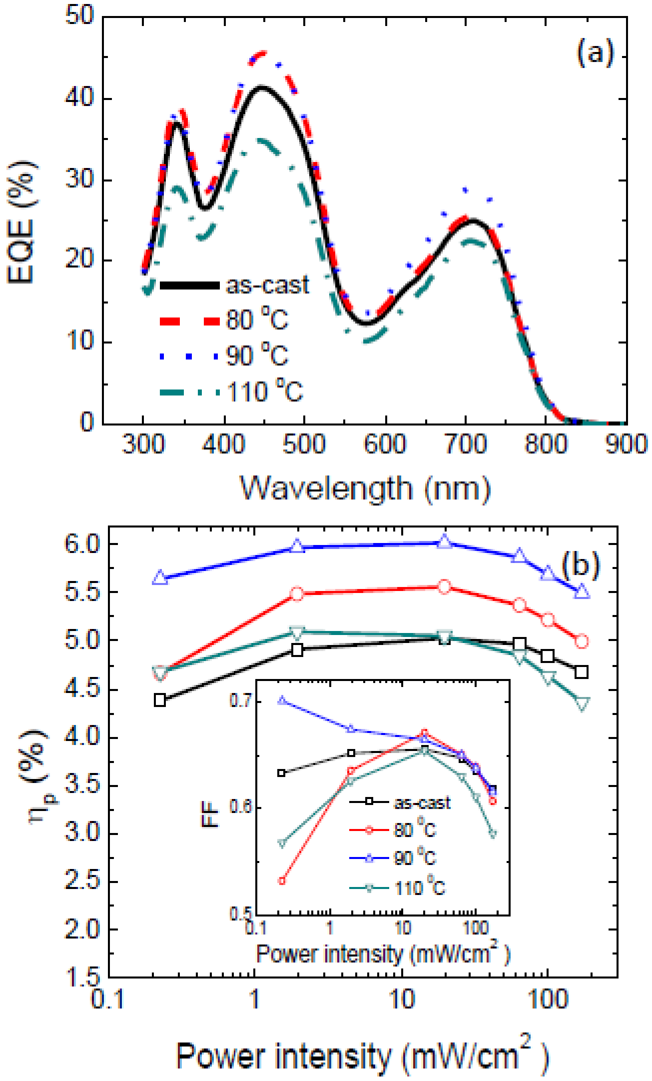

Figure 5.3: External quantum efficiencies (*EQE*) of the control and three cells annealed at temperatures shown in legend; (b) The power conversion efficiency (η_p) versus different power intensities for a device structure of ITO/MoO$_3$(80Å)/1-NPSQ(200Å)/C$_{60}$(400Å)/bathocuproine (100 Å)/Al(1000 Å).

To further improve the photon harvesting efficiency, we thermally annealed the 200 Å thick 1-NPSQ films for 10 min in an ultrahigh purity N$_2$ environment prior to the thermal deposition of the C_{60}, bathocuproine (BCP) and Ag layers that complete the device. Compared with the as-cast devices, the *EQE* in both the C_{60} and 1-NPSQ absorption regions initially increases with 1-NPSQ annealing temperature, as is apparent in Fig. 5.3(a). The peak *EQE* at λ=710 nm due to 1-NPSQ absorption increases from 25% (as-cast) to 32% (90 °C annealed), and then drops to 23% as the temperature is increased further to 110 °C. Similarly, the *EQE* arising from C_{60} absorption at λ=470 nm increases from 42% for as-cast, to 47% for the 90 °C annealed samples and then decreases at higher annealing temperatures. Also, *FF* increases to 0.70 at low intensity (inset in Fig.5.3(b)), however only reaches *FF*=0.64 at 1 sun for devices annealed at 90 °C. Correspondingly, η_p = 6.0 ± 0.7 % at 0.2 sun intensity and η_p = 5.7 ± 0.6 % at 1 sun intensity, as shown in Fig. 5.3(b). We attribute both the high η_p and *FF* to the high absorption constant characteristic of 1-NPSQ, combined with the improved charge transport due to the formation of a NcHJ morphology during annealing. The drop in *FF* at higher power intensities ultimately limits the efficiency of the 1-NPSQ/C_{60} cells.

5.4 The thermal annealing of 1-NPSQ thin films

The formation of nanocrystallites and a rough interface is apparent from the AFM images and selected area electron-beam diffraction (SAED) patterns of the 1-NPSQ thin films both before and after annealing. While the as-cast 1-NPSQ film has a root-mean-square (*RMS*) roughness of 0.8 ± 0.1 nm (c.f. Fig. 5.4(a)), the roughness increases for the film annealed at 90 °C to 1.4 nm ± 0.2 nm (Fig. 5.4(b)).

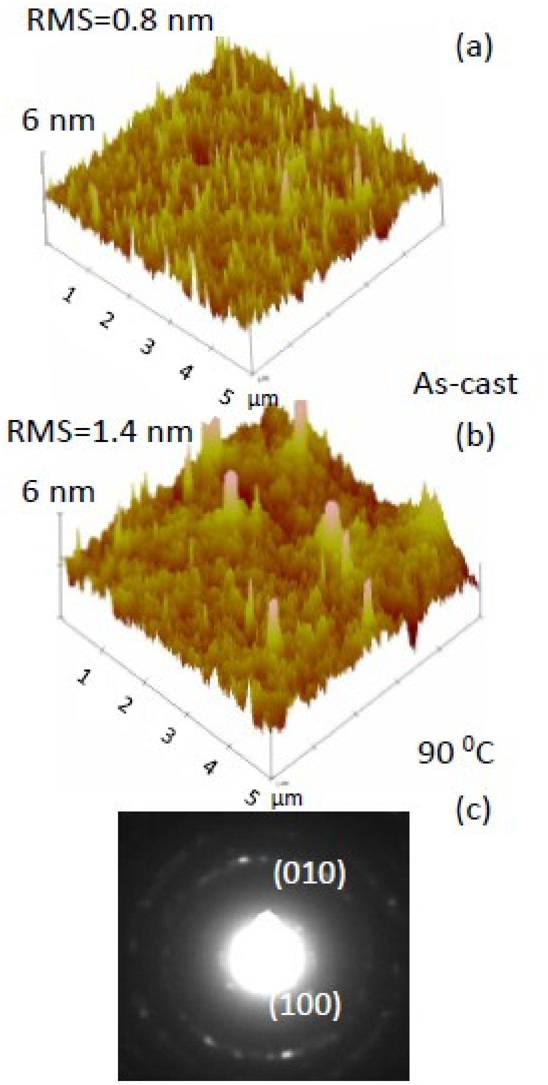

Figure 5.4: 3D atomic force microscope (AFM) images of: (a) as-cast, (b) 90 ^{0}C annealed 1-NPSQ films deposited on indium tin oxide (ITO) coated glass with a 80 Å thick layer of MoO_3; (c) selected-area electron diffraction (SAED) patterns of 90 ^{o}C annealed 1-NPSQ films.

This moderate thermal annealing provides the driving force for the 1-NPSQ molecules to reorganize and migrate into ordered domains, as is apparent from the SAED pattern in Fig. 5.4(c). Note that while the patterns show defined diffraction spots, the spot intensity is weak and is distributed in a Debye-Scherrer ring pattern. This suggests that there is some development of nanocrystallites for the annealed samples, while the SAED patterns for the unannealed samples are featureless, indicative of an amorphous morphology. The rings in Fig. 5.4(c) are indexed to the (100) and (010) crystal reflections, corresponding to planar spacings of 15.57 Å and 8.05 Å, respectively, which corresponds to the equilibrium unit cell dimensions obtained by x-ray diffraction of powder samples of 1-NPSQ.

The solid-state x-ray structure analysis [14] indicates that the SQ single crystal forms a monoclinic staircase-skip herringbone structure with an interplanar spacing of only 3.2Å. However, due to pitch and roll angles of 45^o and 36^o, respectively, there is no π-overlap between aromatic rings on adjacent molecules, which inhibits charge transport. Unfortunately, there is no single-crystal structure available for 1-NPSQ, although its thin film diffraction suggests that it crystallizes into a triclinic structure. In this context, the structure of the analogous molecule, N,N-diphenyl substituted SQ (DPSQ) has a slip-stack staircase triclinic unit cell with an intermolecular spacing of 3.4-3.5Å. However, its large, 80^o roll angle leads to a large π-overlap between the anilinosquaraine ring system and the phenyl groups of the squarate core along the stacking direction. This arrangement facilitates charge transport compared to the less aligned SQ system.

5.5 The 1-NPSQ/C_{60} cells with low series resistance (R_s)

Our analysis suggests that annealing promotes nanocrystalline growth and π-stacking of 1-NPSQ ultimately facilitates hole charge transport. Nevertheless, the limited nanocrystalline growth as inferred from the SAED data inhibits the charge transport under high-power intensity illumination, resulting in a reduction in *FF* at high power intensities for both the as-cast and annealed 1-NPSQ/C_{60} devices as shown in the inset of Fig.5.3(b). The existence of nanocrystalline order is supported by the low resistance of the 1-NPSQ-based devices. Specifically, the as-cast parent SQ/C_{60} control cell [9] has a series resistance of R_S=33 ± 3 $\Omega\cdot\text{cm}^2$ and *FF*=0.53 ± 0.01 whereas for 1-NPSQ/C_{60}, R_s=4.6 ± 0.8 $\Omega\cdot\text{cm}^2$ an *FF*=0.64 ± 0.02. The reduction in R_s is consistent with the similar trends in *FF*, where higher R_s leads to a corresponding lower *FF*. The improved hole transport of 1-NPSQ may explain why both C_{60} and 1-NPSQ have higher *EQE* after thermal annealing (Fig. 5.2). In the case of C_{60}, the exciton diffusion length is >20 nm, or much larger than the roughening observed in the AFM images. However, once an exciton generated in the C_{60} layer migrates to the heterointerface, it is dissociated into an electron and hole, the latter of which is more easily transported to the anode when the structural order of the 1-NPSQ donor is improved. Likewise, the *EQE* of the donor is improved for this same reason, although exciton diffusion is also enhanced in this layer due to the existence of the nanocrystallites.[17] Hence, we infer that the arylamine groups improve charge transport due to improved molecular packing, as noted above. The *FF* and R_S remain largely unchanged with thermal annealing temperature in the range from 80 °C to 100 °C (Table 5.1).

5.6 Conclusion

The squaraine donor, 1-NPSQ is shown to result in improved intermolecular stacking as compared to the parent, SQ donor. Nanocrystalline growth is driven by thermal annealing at 90 °C. The resulting NcHJ leads to improved exciton and hole transport. Optimized 1-NPSQ/C_{60} solar cells with a η_p=5.7 ± 0.6 % at 1 sun intensity, AM1.5G illumination (spectral mismatch corrected) have been realized by a combination of a high V_{oc} = 0.90 ± 0.01V, absorption into the NIR wavelength leading to J_{sc}=10.0 ± 1.1 mA/cm^2, and increased hole conductivity to give FF=0.64 ± 0.01.

References

[1] T. Rousseau, A. Cravino, T. Bura, G. Ulrich, R. Ziessel, and T. Roncali. *J. Chem. Comm.* **13**, 1673(2009).

[2] N. M. Kronenberg, M. Deppisch, F. Wurthner, H. W. A. Lademann, K. Deing, and K. Meerholz, *Chem. Comm.* **20**(12), 4045(2008).

[3] F. Silvestri, M.D. Irwin, L. Beverina, A. Facchetti, G. A. Pagani, and T. J. Marks, *J. Am. Chem. Soc.*​**130**, 17640(2008).

[4] H. Burckstummer, N. M. Kronenberg, M. Gsanger, M. Stolte, M. Meerholz, and F. K. Wurthner, *J. Mater. Chem.* **20**(2), 240(2010).

[5] S. Sreejith, P. Carol, P. Chithra, and A. *J.* Ajayaghosh, *Mater. Chem* **18**, 264(2008).

[6] G. Li, V. Shrotriya, J. Huang, Y.Yao, T. Moriarty, K. Emery, and Y. Yang, *Nature Mater.* **4**, 864(2005).

[7] B. Walker, A. B. Tamayo, X. D. Dang, P. Zalar, J. H. Seo, A. Garcia, M. Tantiwiwat, and T. Q. Nguyen, *Adv.Func.Mater.* **19**, 3063(2009).

[8] F.Yang, K. Sun, and S. R. Forrest *Adv. Mater.* **19**, 4166(2007).

[9] G. D. Wei, R. R.Lunt, K.Sun, S. Y. Wang, M. E.Thompson and S. R.Forrest, *Nano Letters* **10**, 3555(2010).

[10] P. Peumans, S.Uchida, and S. R. Forrest, *Nature* **425**, 158(2003).

[11] G. D. Wei, S.Y.Wang, K. Sun, M. E. Thompson, and S. R. Forrest, *Adv. Ener. Mater.* **1**(2), 184(2011).

[12] C. V. Hoven, X. D. Dang, R. C. Coffin, J. Peet, T. Q. Nguyen, and G. C. Bazan, *Adv. Mater.* **22**, E63(2010).

[13] G. D. Sharma, P. Suresh, S. S. Sharma, Y. K.Vijay, J. A. Mikroyannidis, *ACS Appl. Mater. Interfaces* **2**(2), 504(2010).

[14] S. Y. Wang, L. Hall, V.V. Diev, G. D.Wei, X. Xiao, P. I. Djurovich, and S. R. Forrest, M. E. Thompson, *Chem. Mater.* **23**(21), 4789(2011).

[15] B.P.Rand, D. P.Burk, and S. R. Forrest, *Phys. Rev. B* **75**, 11, 115327(2007).

[16] M. D. Perez, C. Borek, S. R.Forrest , and M. E.Thompson, *J. Am. Chem. Soc.* **131**, 9281(2009).

[17] R. R. Lunt, J. B. Benziger, and S. R.Forrest, *Adv. Mater.* **22**(11), 1233(2010).

[18] V. Shrotriya, G. Li , Y. Yao, T. Morarty, K. Emery, and Y. Yang, *Adv.Func. Mater.* **16**, 2016(2006).

Chapter 6

Functionalized Squaraine Donors for Nanocrystalline Organic Photovoltaics

6.1 Introduction

To improve the performance of bulk heterojunction (BHJ) polymeric solar cells, research has focused on controlling donor/acceptor phase separation (and hence interface area) and crystallinity [1] that leads to increased efficiency for exciton dissociation and conductivity [2, 3]. Nanocrystalline HJs (ncHJ) in small molecule organic solar cells with active layers deposited by vapor deposition [4,5] lead to an analogous, high interfacial surface area and crystallinity. Furthermore, when soluble molecules are blended in the liquid phase with fullerene-based acceptors, ordered molecular stacking is disrupted, forming isolated islands [6,7,8] that inhibit the formation of low resistance, percolating transport paths for carriers. However, solvent [7] or thermal annealing [9, 10] can improve donor/acceptor phase separation in blends while also improving charge transport.[8, 9,11] In particular, we have explored ncHJs consisting of squaraine-based donors combined with a C_{60} acceptor. [6] This process has resulted in both a high FF~0.7 and power conversion efficiency of η_P~6%.

Due to the facile synthetic paths to functionalizing squaraine dyes, these highly absorptive and stable materials [12] have been extensively investigated from both fundamental and technological viewpoints.[9,13,14] In this chapter, we incorporate a family of functionalized squaraines (*f*SQ) in ncHJ structures to investigate correlations between molecular structure, film morphology and device properties. For this study, based on the parent squaraine (SQ): 2, 4-bis[4-(N, N-diisobutylamino)-2,6-dihydroxyphenyl] squaraine, we synthesize three symmetric donors, namely: 2, 4-bis[4-(N-Phenyl-1-naphthylamino)-2,6-dihydroxyphenyl] squaraine (1-NPSQ), 2,4-bis[4-(N,N-diphenylamino)-2,6 dihydroxyphenyl] squaraine (DPSQ), and 2,4-bis[4-(N,N-dipropylamino)-2,6-dihydroxyphenyl] squaraine (PSQ), along with two asymmetric squaraine donors: 2,4-bis[4-(N,N-diphenylamino)-2,6-dihydroxyphenyl] squaraine (DPASQ), and 2-[4-(N,N-diisobutylamino)-2,6-dihydroxyphenyl]-4-diphenylamino] squaraine (ASSQ). The molecular structural formulae of all these compounds are shown in Figure 6.1. Here N-aryl (in 1-NPSQ, DPSQ, DPASQ and ASSQ) and N-propyl groups (in PSQ) are substituted for the alkylamines in the parent SQ.[15] The butyl end-groups of the parent SQ sterically limit its close packing of adjacent molecules, that in turn limit its hole conductivity and exciton diffusion length (L_D) (Table 6.1). Replacement of the end groups with planar aryl moieties exerts control over the crystalline morphology by influencing the intermolecular contact distance while tuning the optical absorption spectrum and energy levels of the films. We find that annealed 1-NPSQ/C_{60} ncHJ solar cells have V_{oc}= 0.90±0.01, FF=0.64±0.01 and J_{sc}= 10.0 ± 1.1 mA/cm^2 due to the combination of a deep, highest occupied molecular orbital (HOMO) energy (and hence high open circuit voltage, V_{oc}), and significant solar spectral coverage along with a high hole conductivity that results in a high short circuit current (J_{sc}). For optimized and annealed 1-NPSQ/C_{60} cells, η_p = 5.7 ± 0.6 %.[16]

6.2 Experiment of six squaraine/C_{60} devices

Single crystal x-ray structures of SQ and DPSQ were obtained for SQ and DPSQ crystals precipitated from CH_2Cl_2/MeOH and toluene, respectively. Solar cells were grown as follows: ITO/MoO_3(80Å)/squaraine (85 ± 5 Å)/C_{60}(400Å)/ 3,4,9,10 perylenetetracarboxylic bisbenzimidazole (PTCBI) (80Å)/Ag (1000Å). The squaraine thin films were spin-coated from their respective 1 mg/ml chloroform solutions on precleaned indium tin oxide (ITO) substrates, coated with a 80 Å thick layer of molybdenum oxide (MoO_3) which is thermally evaporated onto the ITO surface in a vacuum system with a base pressure of 10^{-7} Torr. After spin-coating, C_{60}, PTCBI and the Ag cathode were sequentially thermally deposited in high vacuum. The Ag cathode was patterned by deposition through a shadow mask with an array of 1 mm diameter circular apertures.

The current density-voltage (*J-V*) characteristics and η_p of the solar cells were measured using a solar simulator with AM1.5G filters and an NREL-calibrated Si detector. Solar spectral mismatch corrections were determined using standard methods.[17] The external quantum efficiency (*EQE*) was measured using a monochromator in combination with a Xe lamp.

The ionization energies (i.e. the HOMO energies) for the *f*SQ thin films were measured by ultraviolet photoemission spectroscopy (UPS) using 21.22 eV He-I emission in a Thermo VG Scientific Clam4 MCD Analyzer System. Samples were prepared by thermal evaporation of a 30 nm thick Au film onto a p-type Si substrate, followed by spin casting of the squaraines as above. Transfers between the deposition and analysis chambers were performed at $<10^{-8}$ Torr, and the pressure in the UPS measurement chamber was $<10^{-9}$ Torr. The analyzer resolution was ~0.15 eV as determined by a fit to the Fermi level of Au. The lowest unoccupied molecular orbital (LUMO) energies were determined by measuring the positions of the low energy optical absorption tails and adding those values to their HOMO energies.

To determine the *f*SQ thin film density,[18] the peak absorptions of films cast onto Si substrates from solutions with known squaraine concentrations were measured by assuming a linear dependence of absorbance on concentration (i.e. the Beer-Lambert Law). The thicknesses of the *f*SQ films were determined using a variable angle and wavelength ellipsometer. Then the squaraine films were dissolved in 6 ml chloroform for 5 min, and the absorption of the fSQ solutions was measured. Finally, the densities of *f*SQ films were calculated using a least square fit to the dependence of concentration in solution (as determined from the absolute absorption) on the measured film volume.[18]

Samples for atomic force microscopy (AFM) operated in the tapping mode were prepared by casting the squaraine thin films on 80 Å thick MoO_3 films pre-deposited on ITO-coated glass substrates. Selected area diffraction (SAED) patterns were obtained using a JEOL 2010F transmission electron microscope (TEM), where samples were prepared via wet-transfer of cast and thermally annealed squaraine films onto Cu grids coated with Carbon Type-B. TEM characterization is carried out by collaborator, Dr. Kai Sun.

6.3 Physical properties of six functionalized squaraines

6.3.1 HOMO and LUMO levels

The *f*SQs (Fig. 6.1) have lower HOMO energies than that of SQ, as shown in Table 6.1 and Fig. 6.2. Here, PSQ contains propyl amines, similar to isobutyl amines in SQ, resulting in a HOMO that is lower than that of SQ by 0.1 eV. All the other *f*SQs with aryl amines have even deeper HOMOs of 5.3 eV (1-NPSQ, DPSQ and ASSQ) and 5.4 eV (DPASQ). In combination with the C_{60} acceptor, the interface offset provides sufficient energy for efficient exciton dissociation.

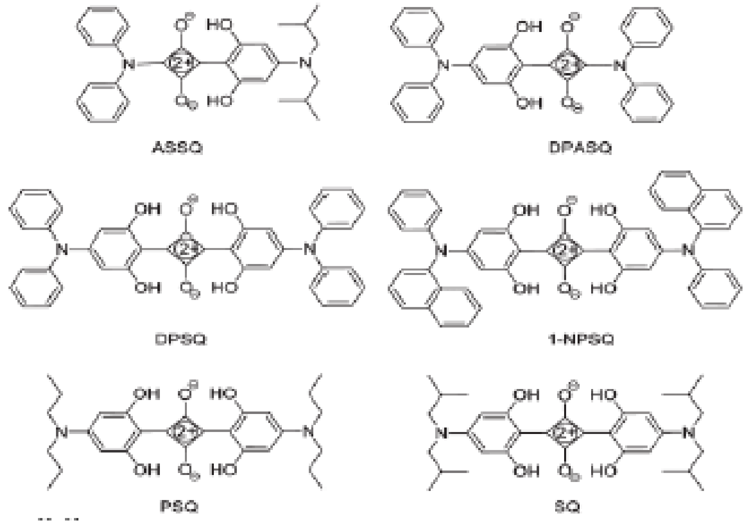

Figure 6.1: molecular structures of the family of six *f*SQs

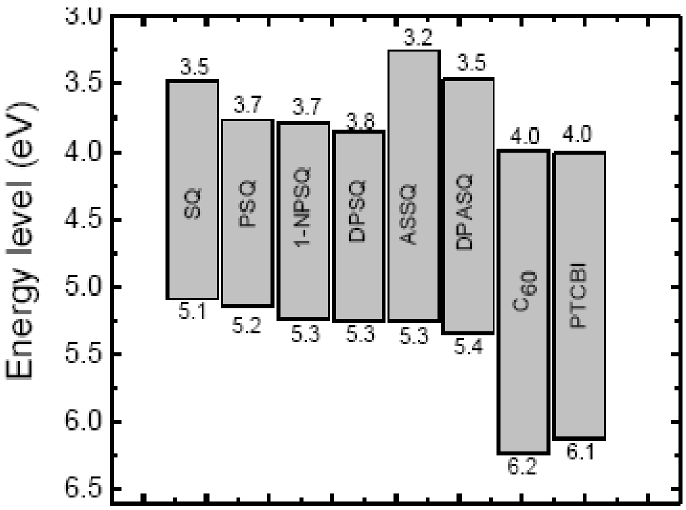

Figure 6.2: The highest occupied molecular orbital (HOMO) and the lowest unoccupied molecular orbital (LUMO) of SQ, PSQ, 1-NPSQ, DPSQ, ASSQ, DPASQ and C_{60}.

Table 6.1**:** Physical properties of squaraine donors.

Molecular species	HOMO (eV)	E_{opt} (eV)	ρ (g/cm^3)	L_D (nm)
DPASQ	5.4	1.9	1.45±0.05	10.7±0.2
DPSQ	5.3	1.5	1.39±0.04	3.4±0.7
PSQ	5.2	1.5	1.34±0.04	NA
1-NPSQ	5.3	1.6	1.35±0.04	2.9±0.8
SQ	5.1	1.6	1.29±0.03	1.6±0.2
ASSQ	5.3	2.1	1.27±0.02	11.0 ±0.6

6.3.2 Optical properties

The absorption spectra of the *f*SQ films are shown in Fig. 6.3. They exhibit a narrow and intense absorption band with maxima at wavelengths of λ=554 nm, 560 nm, 700 nm, 710 nm, 710 nm and 720 nm, with corresponding peak absorption coefficients of 4.0, 3.4, 4.6, 4.0, 4.0 and 3.5 $\times 10^{5}$ cm^{-1} for ASSQ, DPASQ, SQ, 1-NPSQ, PSQ and DPSQ, respectively. PSQ has the broadest absorption, with a full width at half maximum of $\Delta\lambda$=210 nm and two peaks apparent in the spectrum.

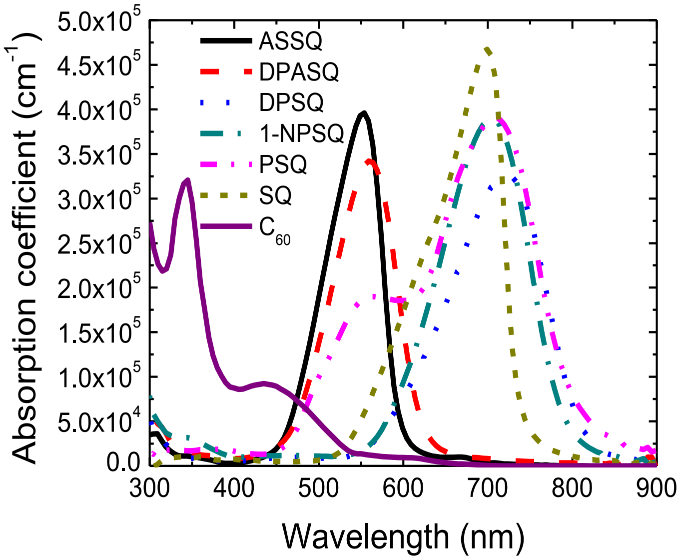

Figure 6.3: Absorption spectra of ASSQ, DPASQ, DPSQ, 1-NPSQ, PSQ, SQ and C_{60}.

6.3.3 Molecular stacking of the single crystal squaraine (SQ) and arylamine-based Squaraine (DPSQ)

Single crystal x-ray structures of SQ and DPSQ were obtained for SQ and DPSQ crystals precipitated from CH_2Cl_2/MeOH and toluene, respectively. Packing diagrams of

SQ and DPSQ show significant differences in the organization of squaraine molecules in the crystal lattice (Fig.6.4(a)) [15]. Squaraine molecules in crystals of SQ are organized in staircase slip-stacks arranged in herringbone-like arrays that alternate at skewed 90º angles with respect to the molecular long axis (Fig. 6.4(a)). The squaraine planes are separated by ca 3.2 Å and have pitch and roll angles of 45º and 36º, respectively. Here pitch inclinations translate adjacent molecules relative to one another in the direction of the long molecular axis, whereas roll inclinations translate the molecules along the short molecular axis. Thus, in the parent SQ with herringbone packing, it is characterized by large roll distortions and a displacement along the short axis by more than 3 Å. There is no π-overlap between aromatic rings in adjacent molecules (Fig. 6.4(b)).

In contrast, crystals of DPSQ are composed of parallel stacks of dimers separated by ca 3.4–3.5 Å between the molecular planes. The dimers units of DPSQ are also organized in a slip-stack staircase arrangement with the long molecular axis having a pitch angle of ca. 38º (Fig.6.4(c)). However, a large roll angle of 80º within the stack leads to a small displacement along the short molecular axis (Fig.6.4(d)). While there are no significant π-interactions between the pendant phenyl rings of adjacent squaraine molecules, the staircase packing and large roll angle leads to considerable π-overlap between the anilinosquaraine ring systems along the stacking direction. Such large roll angles, and consequent cofacial π-stacking as found in crystals of DPSQ, has been proposed to be more conducive to improved charge transport in ordered molecular films than arrangements with small roll angles and poor π-overlap as observed in SQ. Crystals with π-stacked molecules (DPSQ) would be better than those with herringbone packing (SQ) since the charge carrier mobility will be increased by generating large valence or conduction bandwidths (proportional to the orbital overlaps of adjacent molecules). Also, the π-stacks in DPSQ molecules would increase the intermolecular orbital overlap, resulting in higher mobilities.

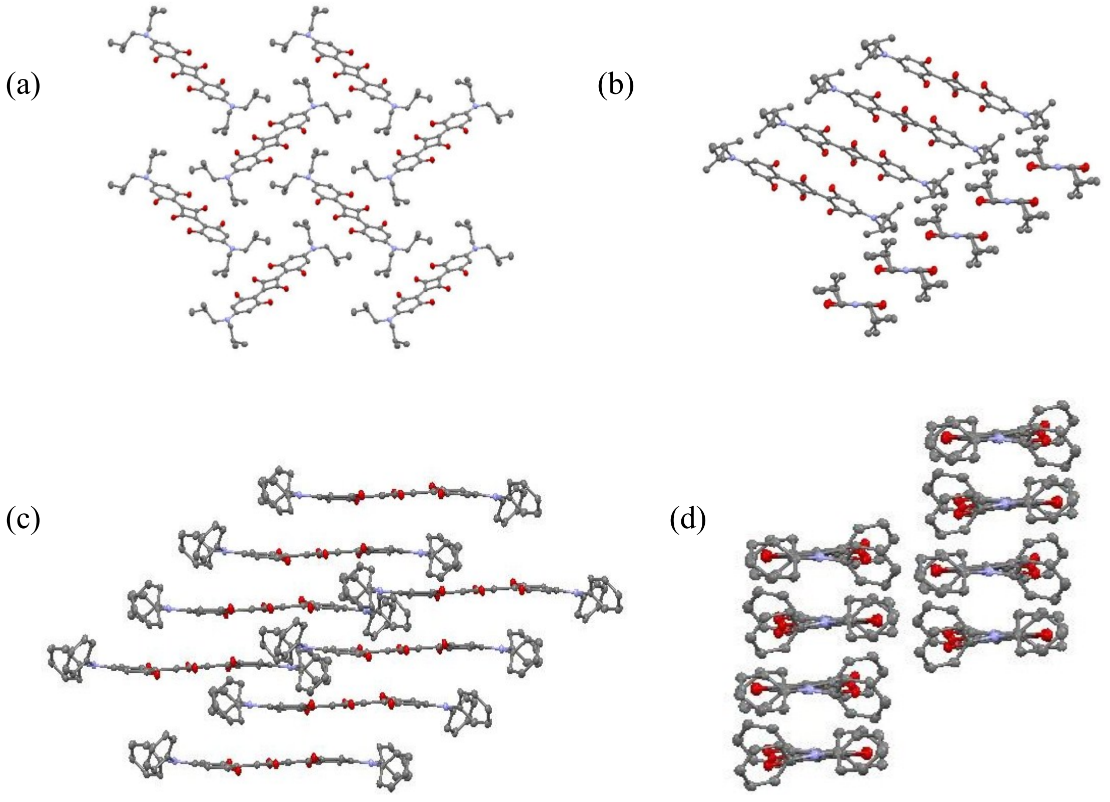

Figure 6.4: Crystal packing diagrams for the parent SQ (top) and DPSQ (bottom). View of SQ showing herringbone structure (a) and molecular stacking arrangement (b). Stacking arrangement of DPSQ viewed down the short (c) and long (d) molecular axes. Hydrogen atoms were removed for clarity [15].

6.3.4. Exciton diffusion length of *f*SQs

The exciton diffusion length (L_D) was measured using conventional spectrally-resolved photoluminescent quenching (SR-PLQ) adapted for optically thin films.[19] For the L_D of the parent SQ, a 50 Å thick C_{60}, and a 50 Å thick BCP layer were deposited on the thermal or solvent annealed SQ films to serve as exciton quenching and blocking layers, respectively. The absorption spectra of these two annealed films are shown in Fig. 6.5(a). Excitation spectra in the L_D measurements were collected for each sample at a wavelength of λ=750nm, while emission spectra were collected with an excitation wavelength of λ= 600nm as shown in Fig.6.5(b). Here, it is assumed that the optical field decays exponentially across the SQ thin film from the BCP/SQ interface. Once the exciton distribution has been calculated, it is integrated throughout the SQ layer to obtain the total exciton population. The ratio, η (λ), of the exciton population for the BCP block *vs*. the C_{60} quenched SQ is then calculated. The normalized η (λ) is then compared to the experimental data as shown in Fig. 6.5(c), where L_D is the only unknown parameter to be determined via the fit. Here, L_D of SQ thin films annealed at 130 ^{0}C is 1.6 ± 0.2 nm. Increasing the crystallinity through solvent annealing leads to $L_D = 5.0 \pm 0.2$ nm, which is three times larger than that of thermally annealed SQ thin films.

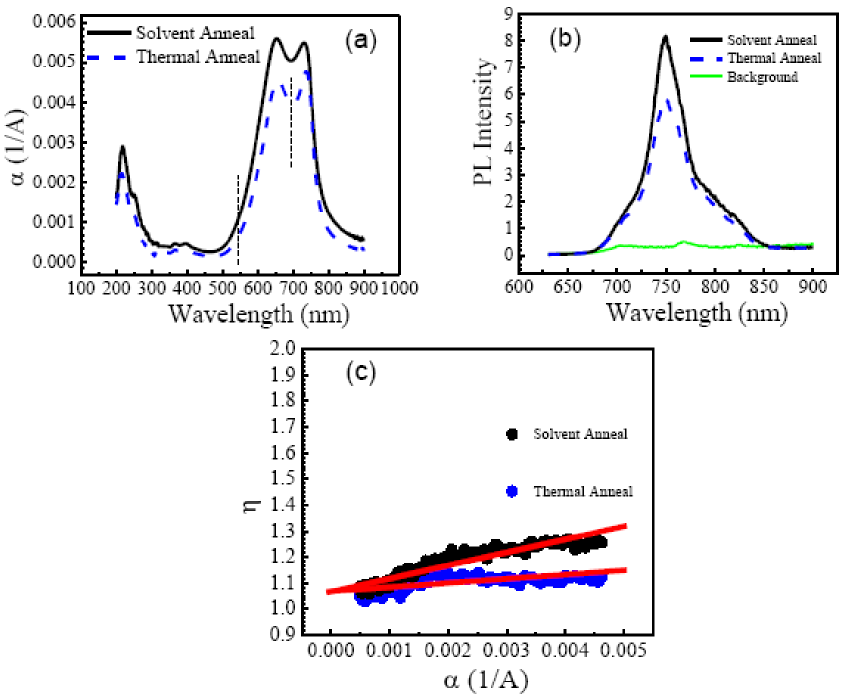

Figure 6.5: (a) Measured absorption coefficients (α) and (b) the photoluminescent (PL) spectrum as functions of wavelengths for thermal (130 ^{0}C) and DCM solvent annealed SQ thin films; (c) quenching ratio (η) versus absorption coefficient for a 40 nm SQ.

However, the conventional SR-PLQ requires the application of optically thick samples, making it impractical for measuring L_D for materials that cannot be made sufficiently thick, especially for solution-cast *f*SQ films. Their thicknesses are typically limited by the solubility in traditional organic solvent such as DCM. To address this problem, the SR-PLQ method has been extended to the case of optically thin *f*SQ films, whose thickness is comparable to or less than that of the optically absorption length across the entire optical absorption spectrum [20]. As the quenching layer C_{60} only affects excitons generated within a distance of ~ L_D from the interface, there is significant difference between the PL in the presence of a blocking or quenching layer. Thereby, the L_D is extracted from the ratio of the PL intensities in these two cases. By calculating the spatial dependence of the optical field in thin films, and using it along with the steady-state exciton diffusion equation, the L_D of ASSQ, DPASQ, DPSQ and 1-NPSQ has been determined shown in Table 6.1.

6.3.5. Surface morphology of the *f*SQ thin films

The AFM images of the as-cast pure SQ thin films as deposited on 80 Å thick MoO_3 buffer layers shown in Fig. 6.5 suggest a variation in surface morphologies for different molecules in the SQ family. The nanocrystalline PSQ film in Fig. 6.5(a) has root-means-square (rms) roughness of 8.8 ± 2.0 nm. The roughness of the five, amorphous SQ films is 5.8 ± 1.0 nm, 1.4 ± 0.5 nm, 1.2 ± 0.6 nm , 0.9 ± 0.2 nm and 0.6 ± 0.2 nm for DPSQ, ASSQ, 1-NPSQ, SQ and DPSQ, respectively. The nanocrystalline morphology in PSQ films creates interdigitated protrusions, generating an increased interface area with the subsequently deposited C_{60} for efficient exciton dissociation.

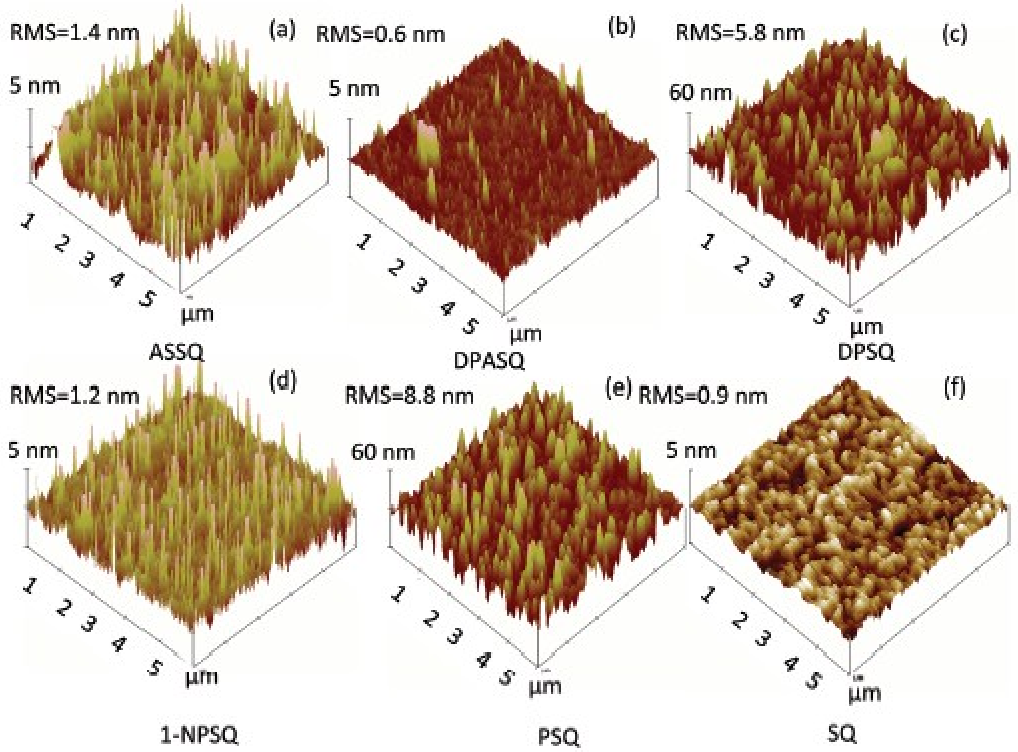

Figure 6.6: Perspective atomic force microscope (AFM) images of as-cast (a) ASSQ, (b) DPASQ, (c) DPSQ, (d) 1-NPSQ, (e) PSQ and (f) SQ films deposited on indium tin oxide (ITO) coated glass with a 80 Å thick surface layer of MoO_3. Here, RMS is the root mean square roughness of the films.

6.4 Squaraines/C_{60} NcHJ solar cells

The external quantum efficiency (*EQE*) of the squaraine-derivative donor/C_{60} OPV cells is shown in Fig.7. The peak *EQE* =30 % is due to SQ absorption in the parent SQ/C_{60} cells, whereas the peak efficiencies of 26% and 40% centered at λ= 350 nm and 470 nm, result from C_{60} absorption. The PSQ devices have the highest peak *EQE*=41% for C_{60}, with the *EQE* of PSQ, reaching up to 33% at λ= 710 nm. The other two symmetric 1-NPSQ/C_{60} and DPSQ/C_{60} cells have comparable C_{60} peak efficiencies of

EQE=32 % at λ= 470 nm and 25 % at λ= 350 nm, both red-shifted from the peaks of 1-NPSQ and DPSQ. The ASSQ/C_{60} devices have similar C_{60} response as the parent SQ/C_{60} cell. The DPASQ/C_{60} cells have relatively lower *EQE* response compared with ASSQ, consistent with its lower absorption efficiency as shown in Fig. 6.3.

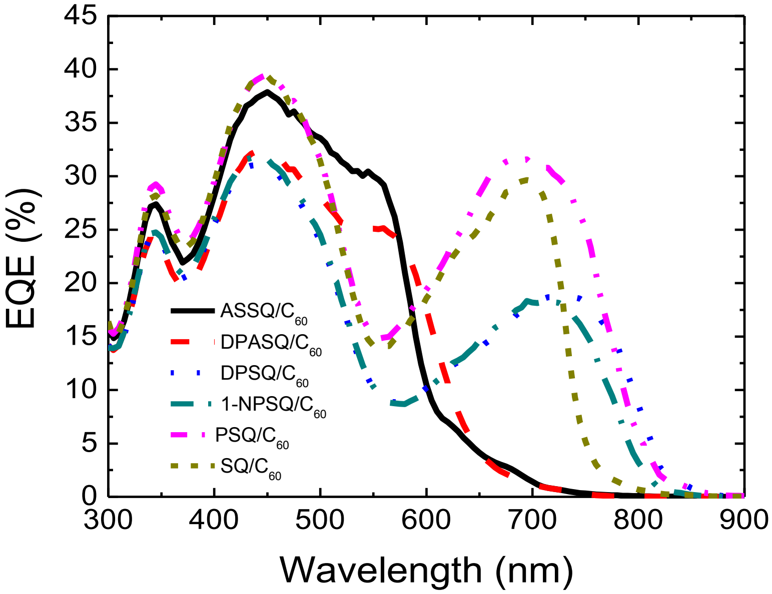

Figure 6.7: External quantum efficiencies (*EQE*) of the six as cast SQs/C_{60} cells with device structure of ITO/MoO_3(80Å)/SQs(85 ± 5 Å)/C_{60}(400Å)/ 3,4,9,10 perylenetetracarboxylic bisbenzimidazole (PTCBI) (100Å)/Ag (1000Å).

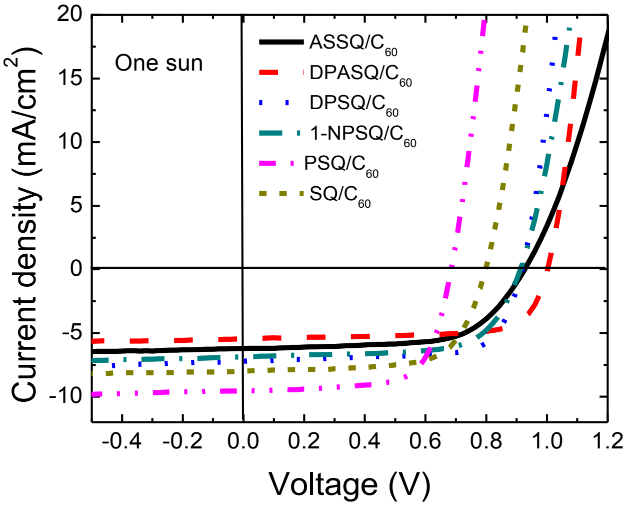

Figure 6.8: The current density (*J*) versus voltage (*V*) at 1 sun illumination of the six as cast SQs/C_{60} cells with device structure of ITO/MoO_3(80Å)/SQs(85 ± 5 Å)/C_{60}(400Å)/ 3,4,9,10 perylenetetracarboxylic bisbenzimidazole (PTCBI) (100Å)/Ag (1000Å).

The $J - V$ characteristics of the as-cast OPV cells at 1 sun illumination are shown in Figure 6.8, with details listed in Table 6.2. A significant increase in V_{oc} is observed from 1-NPSQ, DPSQ, ASSQ to DPASQ, reaching 0.90 ±0.01 V, 0.90 ± 0.01V, 0.91 ± 0.01V and 1.0 ± 0.01 V, which is consistent with the increased interface energy difference, ΔE_{HL}, between HOMOs of the donors and the LUMOs of C_{60} (where ΔE_{HL}=1.3 eV to 1.4 eV) compared with ΔE_{HL} = 1.1 eV for SQ/C_{60} junctions. Moreover, DPASQ/C_{60} devices have the squarest *J-V* curve, reaching FF = 0.73 ± 0.01. The blue-shifted absorption of DPASQ limits the J_{sc} obtained from this device. In contrast, PSQ/C_{60} cells have the highest J_{sc} = 9.72 ± 1.07 mA/cm^2, which is consistent with the high *EQE* in Fig. 6.7. The broadened absorption of PSQ improves photon harvesting in the near-IR.

Table 6.2**:** Performance of as-cast *f*SQ/C_{60} solar cells under 1 sun, AM1.5G simulated illumination and in the dark.

Molecular Species	V_{oc} (±0.01V)	J_{SC} (mA/cm^2)	FF (±0.01)	η_p (%)	J_s (mA/cm^2)	n	R_S ($\Omega\cdot$cm^2)	R_p ($10^6\Omega\cdot$cm^2)
DPASQ	1.0	5.5(±0.1)	0.73	4.0(±0.1)	9.3×10^{-11}	1.56	3.8	116
DPSQ	0.91	7.2(±0.1)	0.70	4.8(±0.2)	8.6×10^{-9}	1.77	1.7	1.5
PSQ	0.68	9.5(±0.1)	0.69	4.6 (±0.2)	1.6×10^{-7}	1.46	3.6	48.9
1-NPSQ	0.90	6.9(±0.1)	0.71	4.3(±0.1)	5.4×10^{-8}	1.84	9.3	1.59
SQ	0.79	8.0(±0.1)	0.68	4.4 (±0.1)	5.9×10^{-8}	1.66	4.7	45.3
ASSQ	0.92	6.3(±0.1)	0.63	3.7(±0.1)	2.5×10^{-9}	1.64	41.2	27.1

The *FF* versus incident power intensity is shown in Fig. 6.9(a). Here, *FF* of the DPASQ/C_{60} cells reaches 0.77 ± 0.01 at low intensity, gradually decreasing to 0.73 ± 0.01 at 1 sun. The DPSQ/C_{60} cells have *FF* ranging from 0.70 ± 0.01 to 0.74 ± 0.01 throughout the measured power intensities. The other symmetric squaraine donor cells (1-NPSQ, PSQ and SQ) have relatively high and intensity-independent *FF* (>0.66) as well. In contrast, *FF* of the ASSQ/C_{60} cells falls off sharply, from 0.70 ± 0.01 at 0.002 suns to 0.56 ± 0.01 at 1.7 suns.

The power conversion efficiency, η_p, as a function of incident power intensity is shown in Fig. 6.9(b). Consistent with their high *FF*, the power efficiency of the DPSQ/C_{60} cell increases from η_p = 3.4 ± 0.2 % at low intensity to 4.8 ± 0.2 % at 1 sun. With the exception of the ASSQ/C_{60} cells, the efficiency of the remaining five *f*SQ-based OPV cells increases with power intensity, which differs from roll-off in η_p previously reported for SQ/fullerene solar cells[8]. The roll off in η_p of ASSQ/C_{60} cells is due to the decrease in *FF*, as shown in Fig. 6.9(a).

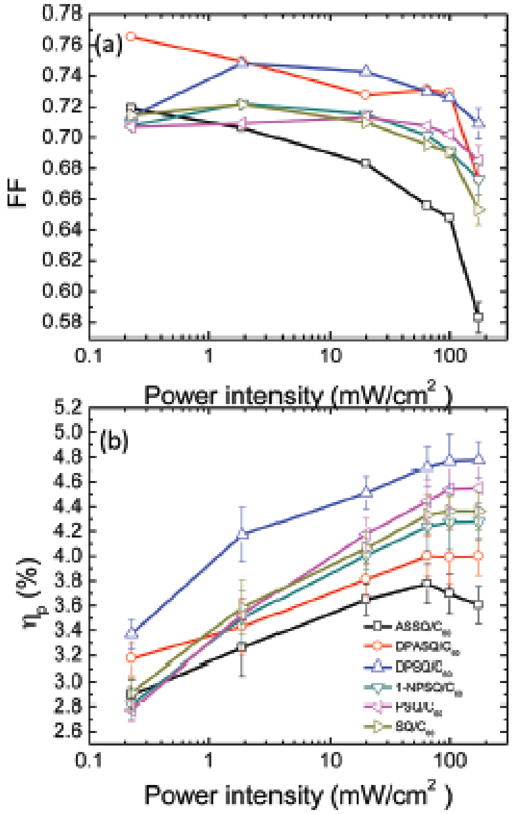

Figure 6.9: (a) Fill factor (*FF*) and (b) power conversion efficiency (η_p) as functions of AM1.5G spectral illumination power intensities (corrected for solar spectral mismatch) of the six as-cast SQs/C_{60} cells with device structure of ITO/MoO_3(80Å)/SQs(85 ± 5 Å)/C_{60}(400Å)/ 3,4,9,10 perylenetetracarboxylic bisbenzimidazole (PTCBI) (100Å)/Ag (1000Å).

6.5 Discussion

The SAED patterns for as-cast squaraine donors other than PSQ are featureless, indicative of an amorphous morphology (Fig. 6.10(a)). The clusters in the annealed DPSQ films suggest a single crystal structure with diffraction features of the SAED pattern indexed to the (010) and ($30\bar{1}$) crystal planes (Fig. 6.10(b)). The annealed 1-NPSQ and SQ films are also polycrystalline (see Fig. 6.10(c) and 6.10(f), respectively). The formation of PSQ nanocrystallites both before and after thermal annealing is apparent in Fig. 6.10(d) and 6.10(e). While the diffraction patterns show defined spots, their intensity is relatively weak and distributed in Debye-Scherrer ring patterns that are indexed to the (100) and (010) crystal reflections. In general, thermal annealing of amorphous, symmetric squaraines results in the formation of nanocrystallinites, whereas the asymmetric DPASQ and ASSQ films are amorphous.

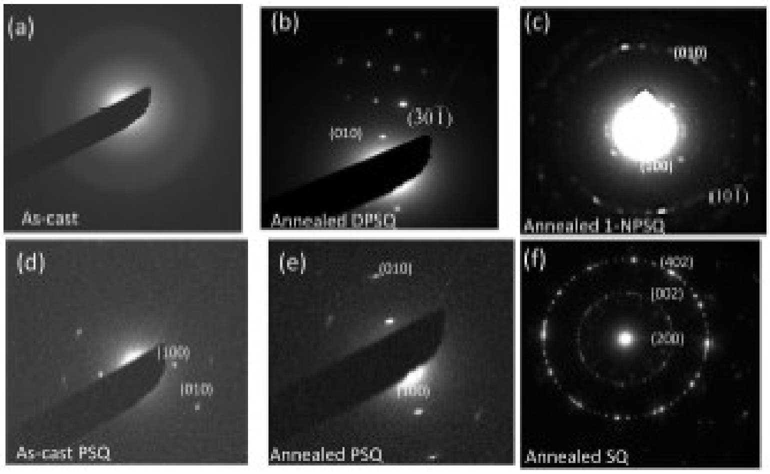

Figure 6.10: The selected-area electron diffraction (SAED) patterns of: (a) as-cast PSQ; (b) annealed PSQ;(c) annealed DPSQ;(d) annealed 1-NPSQ and (e) annealed SQ films.

Fig. 6.11 shows a correlation between OPV *FF* at 1 sun and thin film density. With the increase in density from 1.27 ± 0.02 g/cm^3 for ASSQ, to 1.45 ± 0.05 g/cm^3 for DPASQ thin film, we observe a corresponding increase in *FF* from 0.63 ± 0.01 to 0.73 ± 0.01, suggesting that compact molecular stacking improves the charge transport and collection. Moreover, the densities of the DPSQ and SQ thin films are consistent with those calculated from the single crystal structural data.[15] Here, the DPSQ density of 1.39±0.04 g/cm^3 is larger than that of SQ due to the close molecular stacking resulting from the inclusion of the planar, diphenyl functional groups. As shown previously, this produces a crystal habit with close intermolecular, co-facial π-stacking, and hence an increase in hole mobility. [15] As shown in Fig. 6.9(a), the

DPSQ/C_{60} cells have higher *FF* compared with SQ/C_{60} cells throughout the range of measured power intensities.

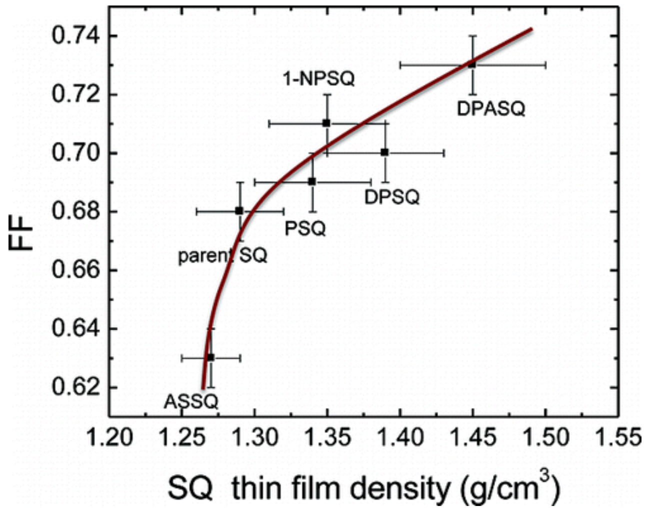

Figure 6.11: Fill factor (*FF*) versus the mass density of six functionalized SQs.

To further understand the performance of the *f*SQ/C_{60} cells, the modified ideal diode equation for organic heterojunctions:[21, 22]

$$J = J_s[\exp(q(V - JR_s)/nk_BT) - \frac{k_{PPd}}{k_{PPd,eq}}] + \frac{V_a - JR_s}{R_p}$$

Here, J_s is the reverse saturation current density, q is the electron charge, R_s is the series resistance, n is the ideality factor, k_B is the Boltzmann constant, T is the temperature, and R_p is the parallel (or shunt) resistance. For simplicity, the ratio of the polaron pair dissociation rate (k_{PPd}) to its equilibrium value ($k_{PPd,eq}$) is assumed to be 1.

As shown in Table 6.2, ASSQ-based cells have the largest series resistance (R_s=41.2 ± 4.6 Ω·cm^2) along with the lowest molecular density of 1.27 ± 0.02 g/cm^3. Their high resistance results in a sharp roll off in *FF* with power intensity in Fig. 6.9(a). In contrast, DPASQ with four phenyl groups on each molecule as shown in Fig. 6.1, has intimate molecular π-stacking and the highest density. As a consequence, DPASQ/C_{60} cells have R_s one order of magnitude lower than ASSQ/C_{60} cells (Table 6.2 and Fig. 6.12).

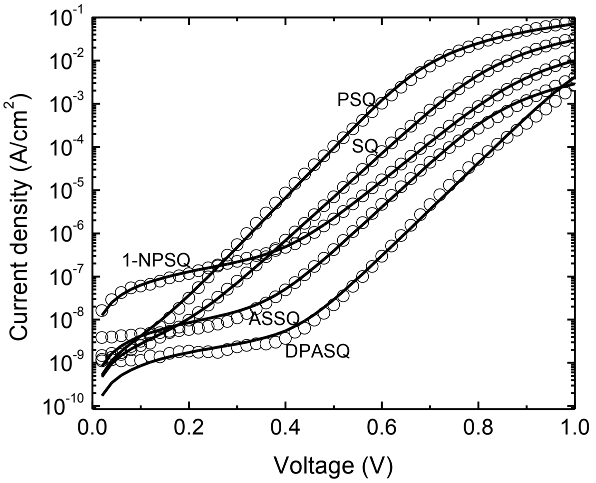

Figure 6.12: Dark current density versus voltage characteristics (open circles) of five as-cast *f*SQs/C_{60} cells. The solid lines are fits to the *J-V* characteristics based on the modified ideal diode equation.

Polycrystalline PSQ introduces a rough interface with C_{60}, resulting in high exciton dissociation efficiency. On the other hand, increased roughness allows the C_{60} to directly contact the anode, resulting in a thousand-fold increase in J_s in comparison with cells based on DPASQ/C_{60} (Table 6.2 and Fig. 6.10). The high J_s leads to a reduction in V_{oc} = 0.68 V, which limits the device efficiency to 4.6 ± 0.2 %.

The exciton diffusion length is an important parameter to consider in the design of solar cells. Typically, L_D is limited due to weak intermolecular interactions. Thermal annealing is, therefore, necessary to generate a distribution of crystallites whose dimension is ~L_D to promote exciton diffusion to a nearby donor-acceptor interface, and thus efficient dissociation. The parent SQ has a relatively short L_D = 1.6 ± 0.2 nm resulting in an optimum SQ donor thickness of only ~65 Å.[6] As shown in Table 6.1, the asymmetric *f*SQs have significantly longer diffusion lengths with L_D = 10.7 ± 0.2 nm for DPASQ, and 11.0 ± 0.6 nm for ASSQ. However, their photon absorption in the green limits the photocurrent generated on such cells. The symmetric NIR absorptive DPSQ and 1-NPSQ have L_D approximately double than that of SQ. Thus, the optimum thickness of 1-NPSQ is 200 Å.[16]

Thermal annealing has been proven to be effective in creating squaraine nanocrystalline structures6 that lead to higher efficiency OPVs. This strategy has been applied to the six *f*SQ/C_{60} devices with the same donor thicknesses of 85 ± 5 Å. As shown in Table 6.2 (as-cast devices) and Table 6.3(annealed devices), annealing improves the efficiencies of all symmetric *f*SQ-based cells. In particular, DPSQ/C_{60} cell efficiency is increased from 4.8 ± 0.2% (as-cast) to 5.2 ± 0.2% (80 °C). In contrast, the ASSQ/C_{60} based cells, have a reduced efficiency following thermal annealing. Furthermore, annealing PSQ results in roughening, and hence the formation of shorts.

Finally, the relatively high *FF* (0.73 ± 0.01) of the DPASQ/C_{60} cell results from its compact molecular stacking, allowing for low resistance to charge transport, and ultimately efficient hole collection at the anode. The PSQ/C_{60} cells with efficiency of 4.6 ± 0.2 % are only slightly inferior to the DPSQ/C_{60} cells resulting from its tendency to form crystalline structures whose dimensions are on the order of L_D.

Table 6.3: Performance of annealed *f*SQ/C_{60} solar cells under 1 sun AM1.5G simulated illumination.

Molecular Species	Annealing Temp.	V_{oc} (±0.01V)	J_{SC} (mA/cm^2)	FF(±0.01) P_0=1 sun[a]	η_p (%) at P_0=1 sun
DPASQ	70°C	0.98	6.25(±0.15)	0.72	4.4(±0.2)
DPSQ	80°C	0.94	7.40(±0.14)	0.72	5.2(±0.2)
1-NPSQ	70°C	0.91	6.97(±0.14)	0.71	4.5(±0.2)
SQ	90°C	0.73	9.27(±0.22)	0.68	4.6(±0.1)
ASSQ	70°C	0.90	6.20(±0.11)	0.63	3.6(±0.1)

[a] P_0 is the incident power. 1 sun = 100 mW/cm^2 at AM1.5G spectral illumination

Table 6.4: Power conversion efficiency (η_p) at 1 sun illumination obtained from optimized *f*SQ/C_{60} solar cells

Devices	$\eta_{p\,(\max)}$ (%)
DPASQ/C_{60}	4.4 ± 0.2
DPSQ/C_{60}	5.2 ± 0.2
PSQ/C_{60}	4.6 ± 0.2
1-NPSQ/C_{60}	5.7 ± 0.6
SQ/C_{60}	4.6 ± 0.1
ASSQ/C_{60}	3.6± 0.1

6.6 Conclusion

A family of functionalized squaraine molecules has been synthesized with molecular structures intended to improve intermolecular π-π stacking. This strategy has led to improved exciton diffusion lengths and conductivities over the parent squaraine lacking the planar end group motif. Solar cells employing an asymmetric molecule with diphenyl end groups (DPASQ) have a $FF = 0.73 \pm 0.01$ and V_{oc}=1.0 V, although its absorption in the green ultimately limits the increase in J_{sc}. We find a correlation between solar cell FF with the *f*SQ thin film density, providing support for the molecular design concept that planar end groups result in close intermolecular stacking, and hence improved charge transport and exciton diffusion. Finally, thermal annealing of the films results in the formation of nanocrystalline morphologies that lead to further improvements in device performance.

References

[1] C. V. Hoven, X. D. Dang, R. C. Coffin, J. Peet, T. Q. Nguyen, and G. C. Bazan, *Adv. Mater.* **22**, 63(2010).

[2] M. S. Kim, B. G. Kim, and J. Kim *ACS Appl. Mater&Interfaces* **1**(6), 1264(2009).

[3] H. Y. Chen, J. H. Hou, S.Q. Zhang, Y.Y. Liang, G.W.Yang, Y.Yang, L.P.Yu, Y.Wu and G. Li, *Nature Photonics* **3**, 649(2009).

[4] P. Peumans, S.Uchida, and S. R. Forrest, *Nature* **425**, 158(2003).

[5] F.Yang, K.Sun and S. R.Forrest, *Adv. Mater.* **19**, 4166 (2007).

[6] G. D.Wei, R. R Lunt, K.Sun, S. Y.Wang, M. E. Thompson, and S. R.Forrest, *Nano Letters **10***, 3555 (2010).

[7] G. D.Wei, S. Y.Wang, K. Sun, M. E.Thompson, and S. R.Forrest, *Adv. Energ. Mater*, **1**(2), 184(2011).

[8] G. D.Wei, S. Y.Wang, K. Renshaw, M. E.Thompson, and S. R.Forrest, *ACS Nano* **4**, 1927 (2010).

[9] F. Silvestri, M. D. Irwin, L.Beverina, A.Facchetti, G.A. Pagani, and T. J. Marks, *J. Am. Chem. Soc.*, **130**, 17640 (2008).

[10] B. Walker, A. B. Tamayo, X. D. Dang, P. Zalar, J. H. Seo, A. Garcia, M.Tantiwiwat, and T.Q. Nguyen, *Adv. Funct. Mater.*, **19**, 3063 (2009).

[11] R. R. Lunt, J. B. Benziger, and S. R. Forrest, *Adv.Mater.* **22**, 1233-1236(2010).

[12] D. Bagnis, L.Beverina, H.Huang, F.Silvestri, Y.Yao, H.Yan, G. A.Pagani, T. J.Marks, A. Facchetti, *J. Am. Chem. Soc.*, **132**, 4074(2010).

[13] U. Mayerhoffer, K.Deing, K. Gruß, H.Braunschweig, K.Meerholz, F.Wurthner, *Angew. Chem. Int. Ed.*, **48**, 8776(2009).

[14] S. Sreejith, P.Carol, P.Chithra, and G. Ajayaghosh, *J. Mater. Chem* 18, 264-274(2008).

[15] S.Y.Wang, L. Hall, V.V.Diev, G. D.Wei, X. Xiao, P. I. Djurovich, S.R.Forrest, and M. E Thompson, *Chem. Mater.*, **23(21)**, 4789(2011).

[16] G. D. Wei, X. Xiao, S. Y. Wang, J. Zimmerman, M. E. Thompson, and S. R. Forrest, Nano Letters **11**, 4261(2011).

[17] V. Shrotriya, G. Li, Y.Yao, T.Morarty, K.Emery, and Y.Yang, *Adv. Funct. Mater.***16**, 2016-2023(2006).

[18] H. F. Xiang, Z. X. Xu, V. A. L. Roy, C. M. Che, and P. T. Lai, *Rev. Sci. Instru.***78**, 034104(2007).

[19] R. R. Lunt, N. C. Giebink, A. A. Belak, J. B. Benziger, and S. R. Forrest, *J. Appl. Phys.* **105**, 2009, 053711(2009).

[20] K. J. Bergemann and S. R. Forrest, *Appl. Phys. Lett.* **99**, 243303(2011).

[21] B. P. Rand, D. P. Burk, and S. R. Forrest, *Phys. Rev. B*.**75(11)**, 115327(2007).

[22] N. C. Giebink, G. P. Wiederrecht, M. R. Wasielewski, and S. R. Forrest, *Phys. Rev. B*, **82**, 155305(2010).

Chapter 7

Conclusions and outlooks

This thesis has focused on understanding the physics of photocurrent generation of organic photovoltaic cells in the small molecule bulk HJ structures, designing new squaraine donor materials and employing them in the unique nanocrystalline heterojunction (NcHJ) device structure to improve device efficiency.

7.1 Conclusions

Spin-coating is a widely used technique for making uniform, thin organic films, especially the active layers in most experimental semiconducting organic-based devices such as photovoltaics. The efficiency of these devices can be greatly improved by employing two blends of organic materials with phase separation during or after the spin-coating process, creating an interpenetrating network that leads to performance enhancements. Thus, blending of semiconducting organic materials can lead to efficient photovoltaic devicesowing to the importance of interfaces in the localization and separation of excitons. The bulk heterojunction is a particularly successful solar cell architecture that is characterized by a large donor/acceptor interface area that leads to efficient exciton harvesting while simultaneously permitting the use of a thick and absorptive photoactive layer.

In Chapter 2, we systematically examine squaraine device performance employing spin-cast SQ:$PC_{70}BM$ and SQ:PCBM bulk structures, in comparison with SQ/C_{70} and SQ/C_{60} planar structures. Our result indicates that the nanomorphology in the SQ:$PC_{70}BM$ and SQ:PCBM introduces internal resistance into the as-cast bulk thin films. The roll off in efficiency (which is due to a roll off in *FF*) at high intensities in the blends, but not observed in the planar junction control cells, arises from the formation of discontinuous pathways for hole transport. The 1:2 SQ:$PC_{70}BM$ cells have peak efficiencies at low light levels of 4.1 ± 0.2 % (solar spectral mismatch corrected), which is comparable to that of the control, solution + vacuum deposited planar nanocrystalline SQ/C_{60} cells (4.1 ± 0.2 %).

In Chapter 3, we have tackled the problem of relatively low *FF* in squaraine bulk HJ solar cells, especially under high power intensity illumination. A unique nanocrystalline heterojunction (NcHJ) architecture with squaraine (SQ)-donor and C_{60}-acceptor phase separation using solution casting of the SQ donor followed by vacuum deposition of C_{60}. The rough interface between the donor and acceptor layers forms a nanocrystallinie HJ with low resistance to the transport of photogenerated carriers, resulting in *FF*=0.69 at 1 sun illumination. Thus, this unique structure opens up a new window to improve the *FF* of small moleculesolar cells. The performance of SQ/C_{60} photovoltaic cells is influenced by the morphology and crystallinity of the SQ film controlled via post deposition annealing. The rough surface of the annealed SQ film is found to be on the scale of its exciton diffusion length, thereby leading to efficient exciton dissociation. A solar power conversion efficiency of the SQ/C_{60} planar devices of η_p =4.6 ± 0.1 % at 1 sun, AM1.5G (correcting for solar mismatch) illumination is obtained for devices whose SQ layer is thermally annealed at 110 ^{0}C.

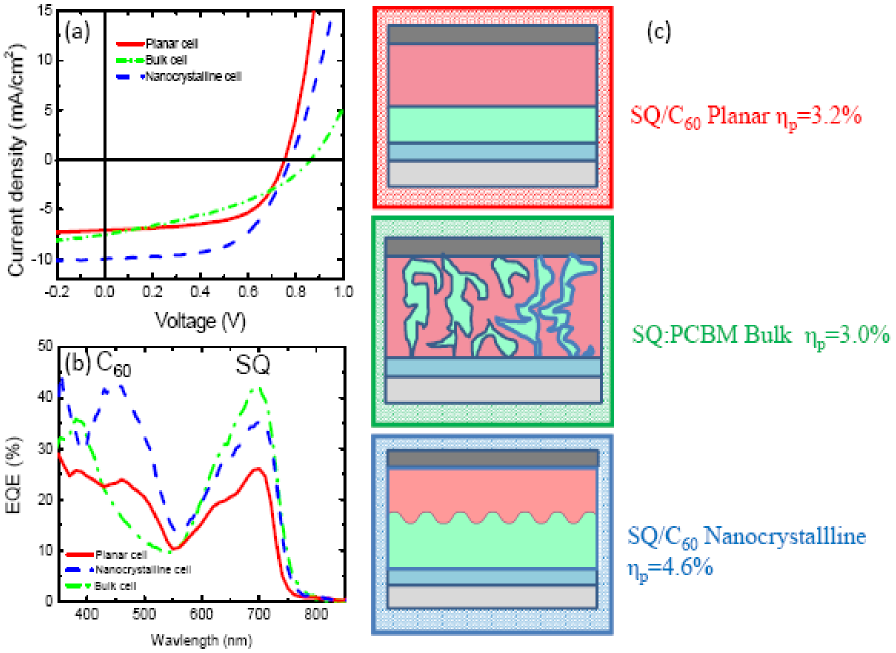

Figure 7.1: (a) Comparison of Current density (*J*) versus voltage (*V*) and (b) External quantum efficiency (*EQE*) for three different device structures: planar, bulk and NcHJ cells.

Based on Chapter 2 and Chapter 3, we have a direct comparison among three different device structures. As discussed above, SQ/C$_{60}$ NcHJ structure is comprised of solution processed SQ layer followed by thermally evaporated C$_{60}$ layers. With the SQ/C$_{60}$ planar structure, both SQ and C$_{60}$ are thermally evaporated and form a continuous, sandwiched structure. For SQ:PCBM (1:6), the active homogeneous layer of SQ:PCBM (1:6) is spin-cast from SQ:PCBM solution. From Fig. 7.1(a), while these three devices have comparable V_{oc}, the SQ/C$_{60}$ NcHJ device has the largest J_{sc} =10.16 mA/cm^2 (Table 7.1). The improved J_{sc} is consistent with the *EQE* response of SQ/C$_{60}$ NcHJ cells (Fig.7.1b). The improved nanomorphology and crystallinity of SQ films enhance exciton harvest and charge collection efficiency. Note that the *EQE* in the C$_{60}$ absorption region increases dramatically, and its peak of 43% is significantly higher than 24% reported previously for vacuum-deposited SQ/C$_{60}$ planar cells. For the SQ:PCBM (1:6) bulk cell, it has the highest *EQE* response in the SQ absorption region:, its peak of 44% is higher than 36% of SQ/C_{60} NcHJ cells, indicating efficient exciton dissociation in the intimately mixed donor/acceptor interface. Meanwhile, the most significant difference among these three structures is the *FF*. SQ/C_{60} NcHJ cell has *FF* = 0.60 at 1 sun illumination, indicating efficient charge collection efficiency. In contrast, SQ:PCBM bulk cell has a sharp slope in its *J-V* curve with *FF* = 0.42, resulting from high resistant and recombination loss. Thus, SQ/C_{60} NcHJ cell has an optimized combination of efficient charge generation and collection.

Table 7.1**:** Summary of squaraine solar cell characteristics under 1 sun, AM1.5G simulated illumination (J_{sc} and η_p solar spectrally corrected) for three different device structures.

Structure	V_{oc} (±0.01V)	J_{SC} (mA/cm^2)	*FF*(±0.01) P_0=1 sun[a]	η_p (%) at P_0=1 sun
SQ/C_{60} planar	0.75	7.13(±0.05)	0.56	3.2(±0.1)
SQ:PCBM bulk	0.78	9.17(±0.14)	0.42	3.0(±0.2)
SQ/C_{60} NcHJ	0.76	10.16(±0.19)	0.60	4.6 (±0.1)

[a] P_0 is the incident power. 1 sun = 100 mW/cm^2 at AM1.5G spectral illumination

In Chapter 4, we continue to address the relatively low *FF* in the squaraine bulk solar cells by employing post solvent annealing processes. DCM solvent anneal leads to the control of the nanoscale phase separation of SQ:$PC_{70}BM$ (1:6) organic films. Through optimizing morphology and molecular ordering of the SQ:$PC_{70}BM$ (1:6) active layers, a peak power conversion efficiency of 5.2 ± 0.3 % was achieved in blended structures, with a maximum cell performance obtained when the exciton diffusion length is approximately equal to the mean SQ crystallite size. This precise structural control takes advantage of the high absorption coefficient and small diffusion length characteristic of this compound, allowing for only very dilute SQ:$PC_{70}BM$ mixtures to result in high solar cell efficiency.

In Chapter 5, we further explored a functionalized squaraine donor, 1-NPSQ, which is shown to result in improved π-π stacking as compared to the parent, SQ donor. Nanocrystalline growth is driven by thermal annealing at $90^{o}C$. The resulting NcHJ of 1-NPSQ/C_{60} devices leads to improved exciton and hole transport. Optimized 1-NPSQ/C_{60} solar cells with a η_p=5.7 ± 0.6 % at 1 sun intensity, AM1.5G illumination (spectral mismatch corrected) have been realized by a combination of a high V_{oc} = 0.90 ± 0.01V, absorption into the NIR wavelength leading to J_{sc}=10.0 ± 1.1 mA/cm^2, and increased hole conductivity to give *FF*=0.64 ± 0.01.

In Chapter 6, we study the correlation between the molecular stacking of functionalized squaraine (*f*SQ) donors and device performance. By means of molecular design, the π-π molecular stacking of the highly absorptive SQ family of donors has been increased to improve charge transport. The HOMO levels of five *f*SQs (1-NPSQ, PSQ, DPSQ, ASSQ and DPASQ) are shown to affect the V_{oc} of the solar cells. The DPASQ/C_{60} solar cells have the highest *FF* = 0.73 ± 0.01 and V_{oc}=1.0 V, although the blue-shifted absorption of DPASQ limits the increase in J_{sc}. DPASQ provides an ideal candidate to blend with other symmetric *f*SQs to broaden the absorption spectrum. We find a correlation between solar cell *FF* with the *f*SQ molecular density, providing support for the concept that planar end groups result in close intermolecular stacking, and hence improved charge transport and exciton diffusion.

7.2 Outlook

Based on the NcHJ device structure, we have reached V_{oc} = 1.0 V and FF = 0.74 at 1 sun illumination. To achieve aefficiency higher than 8%, we need to focus on improving absorptionin the near-infrared (NIR) region to obtain an increasedJ_{sc}; while designing new device architectures with a large donor/acceptor interface areas that leads to efficient exciton harvesting while simultaneously permitting the use of a thick and absorptive photoactive layer. Indeed, CuPc/C_{60} NcHJ solar cells have reached J_{sc} as high as 17.0 mA/cm^2[1]. For solution-processed SQ:$PC_{70}BM$ (1:6) bulk solar cells, J_{SC}=12.0 mA/cm^2 has been obtained (c.f. Chapter 4).

7.2.1 The design and synthesis of new squaraine donors

Though we now have squaraine donors such as 1-NPSQ and DPSQ with absorption λ=850 nm. Without affecting V_{oc} and FF, there is an ongoing search for improved materials that absorb λ=900 nm. It has been reported that a squaraine dye bearing an additional dicyanovinyl acceptor moiety at the central acceptor unit does absorbin the highly desired NIR range. A substantial red shift and band broadening is observed, especially a second absorption band with a maximum at λ=380 nm evolves, resulting in a J_{sc} = 12.6 mA/cm^2 [2].

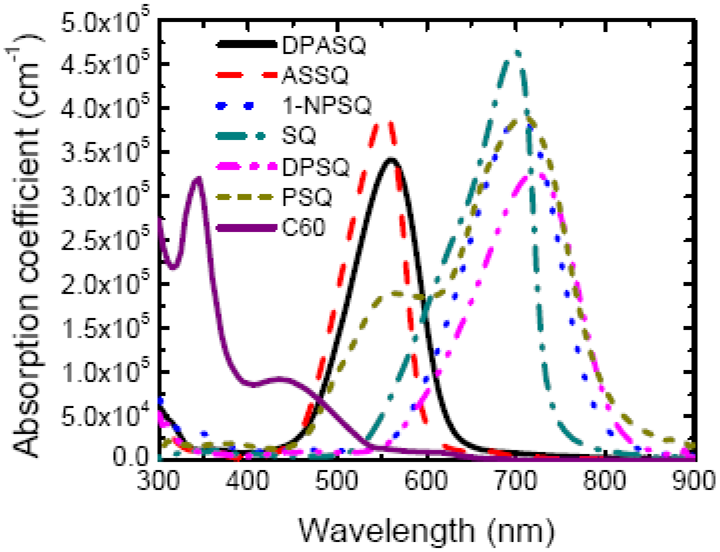

Figure 7.2: Absorption spectrum of the current available squaraine donors and fullerene acceptor

Another promising direction is based on the polymeric squaraine dyes as electron donors in bulk heterojunction solar cells [3]. As pointed out in Chapter 4, one of the characteristic properties of SQ donors is that they have very short exciton (1.6 ± 0.2 nm) diffusion lengths (L_D). This deficiency is partially compensated by its high absorption coefficient compared to that of C_{60}. This motivates the use of SQ:fullerene blend solar cells, whereby a peak measured efficiency of 5.5% (J_{sc}=12.0 mA/cm^2, FF=0.5 and V_{oc}=0.92 V) has been obtained in these structures, with a maximum cell performance achieved when the exciton diffusion length is approximately equal to the mean SQ crystallite size. Here, the *FF* has to be further improved to be larger than 0.65 to target 8% efficiency solar cells. The lack of continuous transport paths in SQ donors typically inhibits the charge collection efficiency and increases series resistance. One option would be to polymerize SQ molecules, forming long repeating chains [4, 5]. The polymerization of a squaraine dye by Yamamoto coupling has been recently investigated and employed as a donor-component with wide absorption range of the polysquaraine from 300 to 850 nm [3]. This broadened and red-shifted absorption is due to exciton coupling of the squaraine monomers in the polymer strand and interchain interactions in the solid material. Using modified processing procedures, there is still room for polymerized squaraine bulk solar cell efficiency improvement.

7.2.2. Synthesis of single crystal squaraine nanowires

Currently, one of the limitations of the squaraine-related solar cells is the short diffusion length of squaraines(for parent SQ, L_D is 1.6 ±0.2 nm, c.f. Chapter 3). This inhibits the use of thicker layer deposition for NcHJ excitonic organic devices. Strategies have been designed to increase L_D of organic materials. Lunt, et al. have shown that L_D in the 3,4,9,10-perylenetetracarboxylic dianhydride (PTCDA) is increased nearly fourfold over that of amorphous thin films through an increase in the extent of crystalline order [6]. Long-range exciton diffusion in highly ordered organic semiconductors has been obtained. For example, the diffusion of triplet excitons in the highly ordered rubrene occurs over macroscopic distance (2-8 μm) [7]. All these results indicate that well-ordered organic semiconductors have longer L_D. Thus, a potential research direction on squaraine-related materials, is to synthesize single crystal squaraine SQ nanowires employed to improve solar cell performance. These SQ nanowires incorporated in the SQ:$PC_{70}BM$ blends should facilitate the formation of a bi-continuous nanoscale morphology that improves carrier mobilities. Meanwhile, they will overcome the problem of poorly assembled SQ crystalline aggregates in the SQ:$PC_{70}BM$ mixtures and open up a potential solution for the roll-off in fill factor with power intensities, as shown in Fig. 7.3.

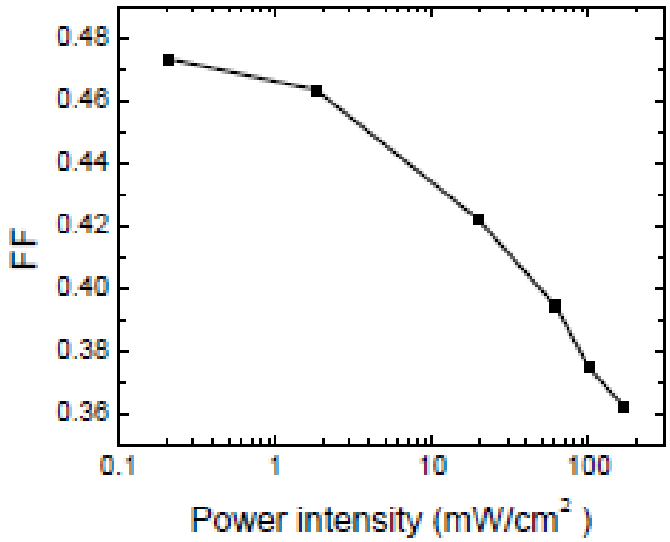

Figure 7.3: Fill factor versus power intensities for a typical as-cast SQ:$PC_{70}BM$ (1:6) solar cell.

The intermolecular forces such as dipole-dipole interactions, π-π stacking and hydrogen bonding can determine the growth habit of the organic nanostructures. Recently, evaporation-induced self-assembly has been demonstrated to be a means for preparing aligned organic nanowires [8]. Here, single crystal SQ nanowires have been synthesized and assembled into aligned films at the dichloromethane (DCM)/methanol (liquid/liquid) interface.

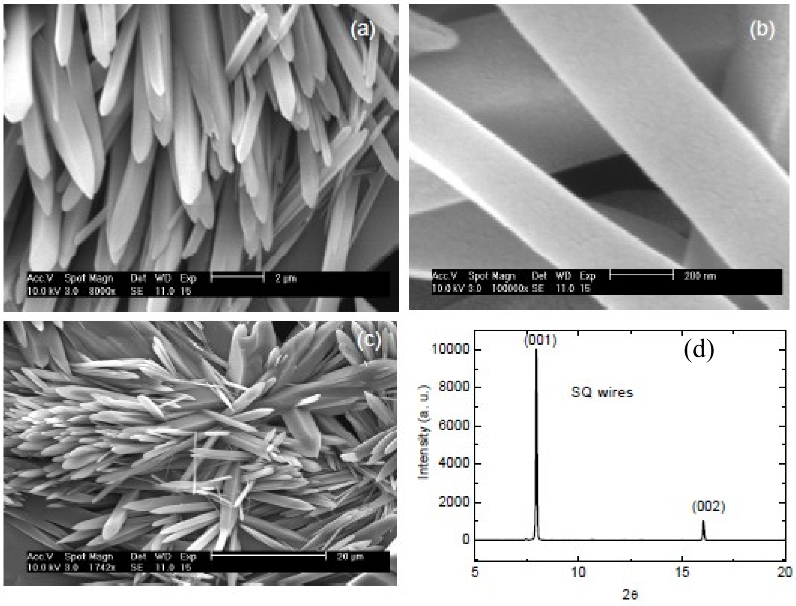

Figure 7.4: (a), (b), (c) SEM images of squaraine nanowires; (d) XRD of squaraine nanowires.

The SQ was dissolved in DCM at a concentration of 6 mg/l. The solution was then placed into a beaker, and methanol was slowly added onto the surface of the DCM solution. The container was placed in a well-ventilated hood to accelerate the evaporation of DCM solvent. During the evaporation of volatile DCM, SQ molecules first aggregated to form clusters, which gradually assembled into a film driven by the compression force arising from the shrinking DCM/methanol interface. After complete evaporation of DCM, SQ films remained at the methanol interface. The rapid evaporation of DCM causes the interface to shrink, inducs a driving force to direct the SQ crystal growth between the interface between methanol and DCM that compresses the SQ wires to align in a more compact and ordered manner. Large-scale SQ nanowires with 100 to 200 nm diameter and several micronmeters in length are shown in Fig. 7.4. The XRD and selected area electron diffraction pattern (SAED) confirm the single crystal feature of as-prepared SQ nanowires (Fig. 7.4(d) and Fig. 7.5).

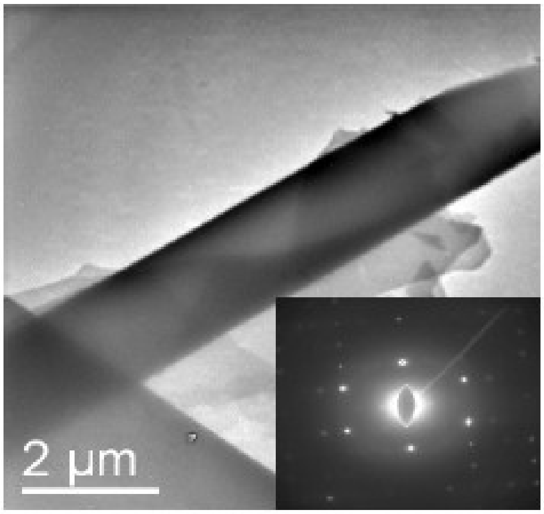

Figure 7.5: TEM image and selected area electron diffraction pattern (SAED) of a single SQ nanowire.

7.2.3 Nanocomposite squaraine:$PC_{70}BM$ solar cells

The efficiency of the squaraine based solar cells is ultimately limited by the photocurrent density J_{sc}. Here, we propose a SQ:$PC_{70}BM$ nanocomposite cells composed of SQ nanowires.

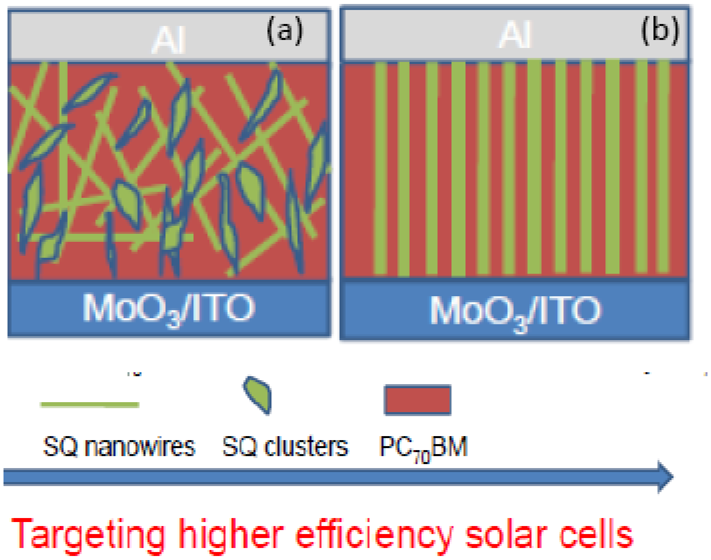

Figure 7.6: Schematic diagram of SQ nanowire:$PC_{70}BM$ bulk HJ solar cells

As shown in Fig.7.6, the interconnected SQ nanowires provide continuous transport path of hole carriers without losing the intermixed interface between SQ donors and PCBM acceptors. The large interface area ensures efficient photogenerated exciton dissociation into free charge. The scale of the phase separation of SQ and $PC_{70}BM$ phases can be optimized in the limit of the exciton diffusion length via control of the assembly of SQ nanowires. Then the separated phases can be contiguous to result in low resistance charge transport from the photosensitive region to the electrode (Fig. 7.8). The ideal case ensures that SQ nanowire arrays are completely embedded into $PC_{70}BM$ matrix, forming a continuous SQ phase while at the same time, maintaining the intimate contact interface between SQ and $PC_{70}BM$ phases.

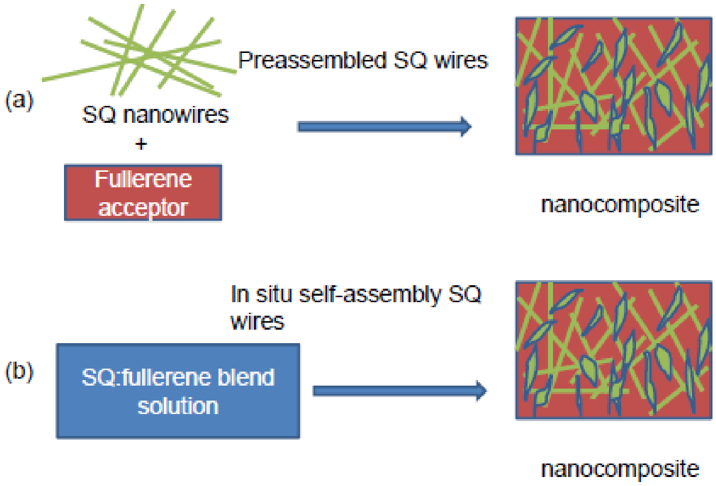

Figure 7.7: Schematic diagram on strategies to assembly squaraine nanocomposite solar cells: (a) pre-assemble SQ nanowires first, then mix them with PCBM; (b) start with SQ:PCBM solution, then in situ self-assembly SQ wires in the SQ:PCBM mixture.

Potentially, two strategies, as shown in Fig. 7.7(a) can be applied to realize the SQ:PC_{70} BM nanocomposite solar cells: preassembled SQ nanowires, then mixed with PCBM; or mixed SQ with $PC_{70}BM$ solution at first, then in situ self-assembly of SQ nanowires in the mixture. The critical step is to control the size of SQ nanowires in the scale of the exciton diffusion length [9].

7.2.4 Two squaraine donor blending solar cells

SQ dyes are promising small molecule donors for organic photovoltaics (OPV) due to their high absorption coefficients in both visible and near-infrared regions. However, it is challenging to further broaden the absorption spectrum for a better coverage of solar spectrum without affecting open circuit voltage (V_{oc}) or fill factor (*FF*). We have obtained both symmetric and asymmetric SQs with different absorption bands by engineering the parent molecular structure of 2,4-bis[4-(N,N-dissobutylamino) -2,6-dihydroxyphenyl] squaraine (SQ). The symmetric SQ (1-NPSQ) absorbs photons within the wavelengths between λ=550 nm and 800 nm, whereas the asymmetric SQ (DPASQ) has absorption between λ=450 nm to 650 nm, which fills in the absorption gap between 1-NPSQ and C_{60} (Fig. 7.2). By blending 1-NPSQ and DPASQ together, followed by thermal evaporation of C_{60}, as shown in Fig. 7.8, the 1:1 blended cells have broadened spectrum coverage in comparison with pure 1-NPSQ/C_{60} and DPASQ/C_{60} cells.

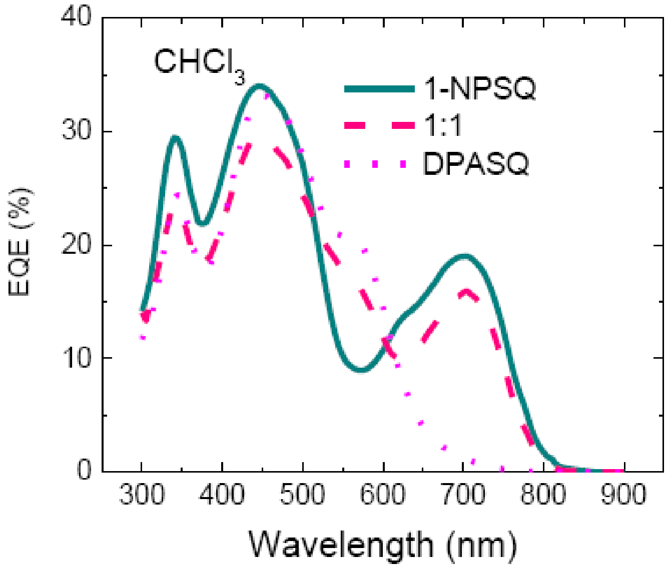

Figure 7.8: External quantum efficiency (*EQE*) of 1-NPSQ/C_{60}, DPASQ/C_{60} and 1:1 blend/C_{60} devices

Table 0.2: Device performance of neat 1-NPSQ, DPASQ and blend SQ cells with different weight ratios.

Weight ratio between 1-NPSQ and DPASQ	V_{oc} (V)	J_{SC} (mA/cm^2)	*FF*	η_p (%) at One sun
1-NPSQ	0.92(±0.02)	7.3(±0.1)	0.70(±0.01)	4.7(±0.1)
Blend (1:0.2)	0.94(±0.02)	7.5(±0.1)	0.71(±0.01)	5.0(±0.1)
Blend (1:0.5)	0.98(±0.02)	7.9(±0.2)	0.71(±0.01)	5.5(±0.2)
Blend (1:1)	0.98(±0.02)	7.6(±0.2)	0.7(±0.02)	5.2(±0.3)
Blend (1:2)	1.00(±0.02)	6.6(±0.2)	0.66(±0.01)	4.3(±0.2)
DPASQ	1.00(±0.02)	5.9(±0.1)	0.72(±0.01)	4.3(±0.1)

The weight ratio of 1-NPSQ and DPASQ can be varied to optimize sunlight harvesting, as shown in Table 7.2. The short circuit current density of 7.9 ± 0.2 mA/cm^2 has been reached. Most interestingly, the open circuit voltage (V_{oc}) is dominated by the DPASQ donor, ranging from 0.94 V to 1.0V. The Fill factor remains as high as 0.70. Overall, the power conversion efficiency η_p at 1 sun intensity increases from 4.7% for neat 1-NPSQ cells to 5.5% for blend SQ cells at an optimal ratio of 1:0.5. All of these results have opened up a window to further improve squaraine-related solar cell performance.

7.2.5 Solvent annealing of functionalized squaraines (*f*SQ)/C_{60} solar cells

In Chapter 5, we have explored solvent annealing on the squaraine:PC_{70} BM bulk solar cells. Their efficiency was increased to to 5.5 % by this method. Here DCM solvent vapor is diffused into the mixture of SQ:PC_{70}BM films to facilitate the migration of the SQ molecules. Similarly, it is worthwhile to improve *f*SQ/C_{60} solar cell efficiency through post-solvent-annealing. After spin-coating *f*SQ thin films, DCM solvent vapor can be applied to anneal as-cast *f*SQ films covered with thermally evaporated C_{60} layers as shown in Fig. 7.9. Interestingly, with appropriate DCM solvent annealing, the *EQE* response of C_{60} peak increases from 35% to 44% (DCM 12 min) and 1-NPSQ *EQE* peak increases from 18% to 43% (Fig.7.10). This increase of photoresponse through solvent annealing provides a strategy to improve the photocurrent density for the*f*SQ materials.

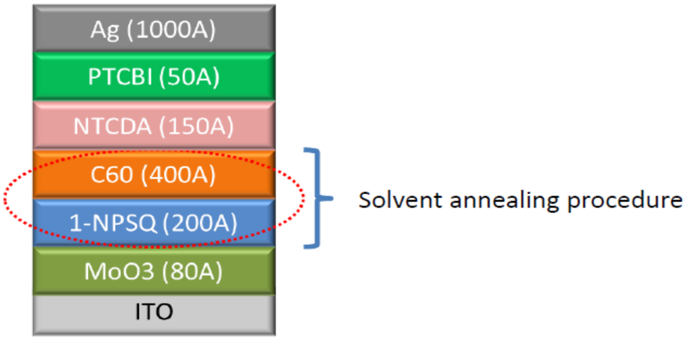

Figure 7.9: One typical 1-NPSQ/C_{60} device architecture and solvent annealing procedure on the 1-NPSQ/C_{60} layers

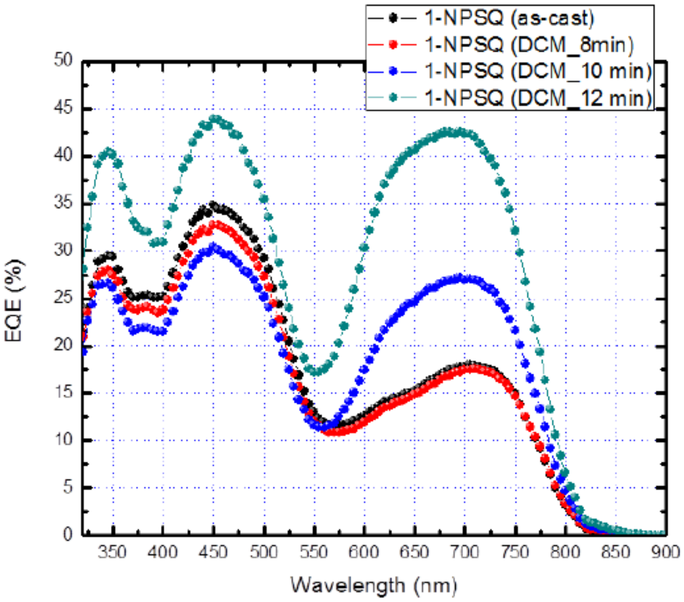

Figure 7.10: *EQE* response of as-cast and DCM annealed 1-NPSQ/C_{60} solar cells

7.3 Afterword

The results of organic solar cells presented in this thesis suggest that squaraine-related small molecule materials have promise for achieving further increases in solar cell efficiency in ordered nanocrystalline OPVs. This can provide an ideal material system and device architecture for low-cost, large-area OPVs using roll-to-roll printing techniques, thereby providing a clean and renewable energy source through solar energy conversion.

References

[1] F. Yang, K. Sun, and S. R. Forrest , *Adv. Mater.***19**, 4166–4171(2007).

[2] U. Mayerhöffer, K. Deing, K. Gruβ, H. Braunschweig, K. Meerholz, and F. Würthner, *Angew. Chem. Int. Ed.* **48**, 8776(2009).

[3] S. F. Vlker, S. Uemura, M. Limpinsel, M. Mingebach, C. Deibel, V. Dyakonov, C. Lambert, *Macromol. Chem. Phys.* **211**, 1098(2010).

[4] C. Yang, J. K. Lee, A. J. Heeger, and F. Wudl, *J. Mater. Chem.***19**, 5416(2009).

[5] Y. Y. Liang, Z. Xu, J. B. Xia, S.-T. Tsai, Y. Wu, G. Li, C. Ray, and L. P. Yu, *Adv. Mater*. **22**, 135(2010).

[6] R. R. Lunt, N. C. Giebink, A. A. Belak, J. B. Benziger, and S. R. Forrest, *J. Appl. Phys.* **105**, 053711(2009).

[7] H. NNajafov, B. Lee, Q. Zhou, L. C. Feldman, and V. Podzorov, *Nature Mater*. **9**, 938(2010).

[8] C. Y. Zhang, X. J. Zhang, X. H. Zhang, X. M. Ou, W.F. Zhang, J. S. Jie, J. C. Chang, C.S. Lee, and S.T. Lee, *Adv. Mater.* **21**, 4172(2010).

[9] H. Xin, O.G. Reid, G. Q. Ren, F. S. Kim, D. S. Ginger, and S. A. Jenekhe, *ACS Nano*. **4**, 1861(2010).

Appendix 1

Thermodynamic limits of quantum photovoltaic cell efficiency based on one photon absorption

Quantum solar cells (i.e. cells containing a quantum confined region) [1] have been suggested as a means to exceed the Shockley and Queisser (SQ) efficiency limit [2] via the absorption of sub-band gap photons ordinarily lost in a conventional homojunction cell. Free-carriers generated in the narrow energy gap wells contribute to photocurrent, in addition to photocarriers generated by higher energy absorption directly in the wide gap barrier regions. This exploitation of more than one carrier population to achieve more complete coverage of the solar spectrum [3] is based on the assumption that the two carrier populations do not achieve thermal equilibrium with each other or with the lattice before they are extracted from the device. This is equivalent to assuming that the quasi-Fermi levels (QFL) in the quantum confined and bulk semiconductor regions are at different energies.

The mechanisms for efficiency enhancement over homojunction solar cells have been the subject of considerable debate [4]. Luque, et al. [5] have claimed that the second law of thermodynamics is violated when sub-band gap photocarriers are transported into the barrier material without excitation by a second photon. They conclude that two sub-band gap photons are required to complete the transition of an electron from the valence band to the intermediate level and from there, into the conduction band [6]. Unfortunately, the prospects for achieving high efficiency via this two photon process are unlikely since the generation rate induced by the second photon (~ 10^3 s^{-1}), is typically less than the recombination rate within the lower band gap quantum dots (~10^9 s^{-1}) due to the small solar power density (~0.1 W/cm^2), the small optical absorption cross section (~10^{-15}-10^{-16} cm^2) and typically low density of dots (~10^{10} cm^{-2}) [7]. Thus, there remains a large discrepancy between theoretically predicted limiting efficiency of 63.2% for cells based on quantum dots, and actual device performance [8-9].

Both experimental and theoretical analysis have provided evidence for a separation in QFL between the well and barrier materials [10-11]. For example, InAs/GaAs quantum dot (QD) solar cells have shown a 0.187 eV QFL separation between the GaAs barrier and InAs QDs under illumination [12]. In this work, the efficiency of quantum solar cells in the radiative limit is analyzed using the detailed balance framework, with carrier generation due solely to single photon absorption. In the quantum confined regions, photoexcited carriers escape via thermionic emission or tunneling into the conduction band of the barrier material [4]. Efficiencies of QD cells can exceed the SQ limit when there exists a positive QFL discontinuity between the quantum confined and bulk regions.

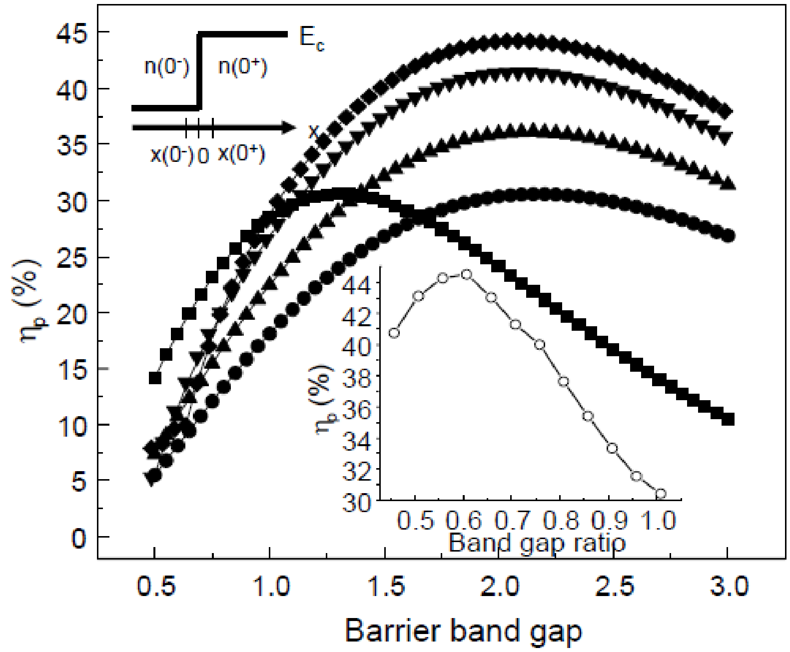

Figure 1. Detailed balance efficiency limit of a quantum solar cell and a homojunction cell as a function of the band gap of the barrier material with $f = 2.18\times10^{-5}$. The band gaps of the quantum materials are assumed to equal 60% of the barrier materials. A maximum efficiency of 44.5 % for a black body at T_{sun}=5963 K is found for the quantum confined cells. The various lines correspond to the SQ limit (squares), ξ=0 (circles), ξ=0.2 (triangles), ξ= 0.4 (inverted triangles), ξ= 0.5 (diamonds). *Upper Inset*: Conduction band edge of a heterojunction positioned at x=0. *Lower Inset*: Maximum achievable efficiency versus the corresponding band gap ratio between quantum and barrier materials.

Such a cell is macroscopically consistent with the second law of thermodynamics, but requires the carrier temperature in the wells to exceed that of the lattice to support the positive QFL discontinuity. When materials with dissimilar band gaps are incorporated into the junction depletion region, there is a discontinuity of the electron affinity and the density of states at the heterointerface [13]. The electron density under quasi-equilibrium can be described by Maxwell-Boltzmann statistics:

$$n(x) = N_c(x) \exp\left[\frac{\mu_e(x) - E_c(x)}{kT}\right] \quad , \tag{1}$$

when $E_c(x)-\mu_e(x)>kT$. where $N_c(x)$, $\mu_e(x)$, and $E_c(x)$ represent the local effective density of states, electron quasi-Fermi energy, and the conduction band minimum, respectively, and x is the distance from the heterojunction, as shown in the upper inset, Fig. 1. Also, k is the Boltzmann constant, and T is the temperature. Therefore, the electron quasi-Fermi energy difference at the heterointerface is given by:

$$\Delta\mu_e = \Delta\chi + kT \ln\left[\frac{n(0^+)N_c(0^-)}{n(0^-)N_c(0^+)}\right] \tag{2}$$

where $\Delta\mu_n = \mu_n(0^+) - \mu_n(0^-)$, χ is the electron affinity of the well and barrier materials, and $\Delta\chi = \chi(0^+) - \chi(0^-)$. The total thermionic emission and tunneling current density, J_L, determine the ratio of $n(0^-)$ to $n(0^+)$ [11]. That is:

$$J_L = -qv_{e1}(1+\delta)n(0^-)\exp(-\frac{\Delta E_c}{KT}) + qv_{e2}(1+\delta)n(0^+) \,. \tag{3}$$

Here, q is the electron charge, v_{e1} and v_{e2} are the mean electron thermal velocities from quantum to barrier, and from barrier to quantum material, respectively, δ is the ratio of charge entering the conduction band via tunneling *vs.* thermionic emission, and ΔE_c is the conduction band offset between the well and barrier regions. Here, $\Delta\mu_n \neq 0$ in the presence of thermionic or tunneling currents (J_L>0). Similar expressions can be written for the hole quasi-Fermi levels.

Sub-band gap photocarriers escape from the potential well by thermionic emission, or thermally assisted tunneling through the confining barriers [4]; otherwise they recombine via radiative or nonradiative processes. The change of the free energy, dF, due to the number, dN, of electrons and holes that a solar cell delivers to a load is [14]:

$$dF = dF_e + dF_h = (\mu_{e,w} - \mu_{h,w})dN = \mu_w dN\,, \tag{4}$$

Here, $\mu_{e,w}$ and $\mu_{h,w}$ are electron and hole quasi-Fermi energies in the quantum confined regions.

The total current is the difference between the photons absorbed and the photons re-emitted via radiative recombination. Both the absorbed and emitted photon fluxes, ϕ, are [16]:

$$\phi(E_1, E_2, T, \mu) = \frac{2\pi}{h^3 c^2} \int_{E_1}^{E_2} \frac{E^2}{\exp((E-\mu)/kT)-1} dE\,, \tag{5}$$

where h is Planck's constant, c is the speed of light, and $[E_1, E_2]$ is the energy interval of the radiation flux. The chemical potential, μ, of luminescent radiation is equal to the carrier QFL separation, while in the case of black-body radiation, it is zero.

The photocurrent density is determined by assuming that photocarriers from the barrier material do not trap in the quantum well layers, and that all sub-band gap photogenerated carriers escape and contribute current to the external load:

$$\begin{aligned} J_{ph} &= q[f\,\phi(E_{gb},\infty,T_{sun},0) - \phi(E_{gb},\infty,T_a,\mu_b)] + q[f\;\phi(E_{gw},E_{gb,}T_{sun},0) - \phi(E_{gw,}E_{gb,}T_a,\mu_w)] \\ &= J_b + J_w \end{aligned} \tag{6}$$

Here, f is the solid angle subtended by the sun [2], and E_{gb} and E_{gw} are the band gaps of the barrier and quantum materials, respectively. Also, T_{sun} is the solar surface temperature, T_a is the cell ambient temperature, and μ_b and μ_w are the chemical potentials in the barrier and quantum regions, respectively. Complete absorption of radiation at photon energies $E > E_{gb}$ or $E > E_{gw}$ requires that μ_b and μ_w are less than E_{gb} and E_{gw}. Finally, J_b and J_w are the photocurrents from the barrier and quantum confined regions, respectively.

Since the reverse saturation currents, J_{0b} and J_{0w} are due only to radiative recombination between free electrons and holes, the *J-V* characteristic of the cell is given by:

$$J_{TOT} = J_{0b}[\exp(qV/kT_a)-1]-J_b+J_{0w}[\exp((qV-\Delta\mu)/kT_a))-1]-J_w \qquad (7)$$

where J_{0b} and J_{0w} are equal to the second and fourth terms of Eq. (6), respectively. The aggregate electron and hole QFL discontinuity is $\Delta\mu = (E_{gb}-E_{gw})\cdot\xi$, where the parameter ξ ranges between 0 and 1. The total power density generated by the cell, *P*, is $P=-JV$, with a maximum at $\partial P/\partial V = 0$. The efficiency is found by dividing the maximum power by the incident solar flux, $f\sigma T_{sun}^4$, where σ is the Stefan-Boltzmann constant[6]. Under uniform solar irradiation, f=2.18×10^{-5}.

The efficiency calculated as a function of E_{gb} is shown in Fig. 1. The sun and cell are assumed to be black bodies with temperatures of 5963K and 300K, respectively. When there is no QFL separation (corresponding to ξ=0), the efficiency limit of quantum solar cells is equal to the SQ limit (31%). In this case, the efficiency of a quantum solar cell is always less than or equal, to that of a homojunction cell. While photon absorption in the quantum confined regions contributes to the photocurrent, increased radiative recombination results in a reduction in open circuit voltage, V_{oc}.

With an increase in QFL separation (i.e. where ξ increases from 0 to 0.5), the cell efficiency increases (see Fig. 1). The optimum band gap of the barrier materials shifts from 1.3 eV for conventional cells with a maximum efficiency of η_{max}=31%, to 2.0 eV for quantum solar cells with η_{max}=44.5 % (at E_{gw}=0.6E_{gb}). A further increase in QFL splitting continues to increase η_{max}, but the integrated entropy generation becomes negative, in violation of the second law of thermodynamics. The lower inset in Fig. 1 shows $\eta_{\max}$ versus the corresponding band gap ratio between the quantum and barrier materials. The maximum, thermodynamically consistent efficiency increases from 40.8% (E_{gb}=2.75 eV, E_{gw}=1.24 eV and $\Delta\mu$=0.30 eV) to 44.5% (E_{gb}=2.0 eV, E_{gw}=1.20 eV and $\Delta\mu$=0.42 eV) when the band gap ratio increases from 0.45 to 0.6. Further increases in the band gap ratio gradually reduces $\eta_{\max}$ to the SQ limit. Interestingly, the band gaps of the quantum well materials are between 1.2 eV and 1.3 eV, which correspond to the values that yield the SQ limit for single band gap solar cells. Here the determination of the QFL separation is based on *macroscopic* compliance with the second law of thermodynamics; *microscopic* compliance at the well/barrier QFL discontinuity must be provided by an elevated carrier temperature in the wells.

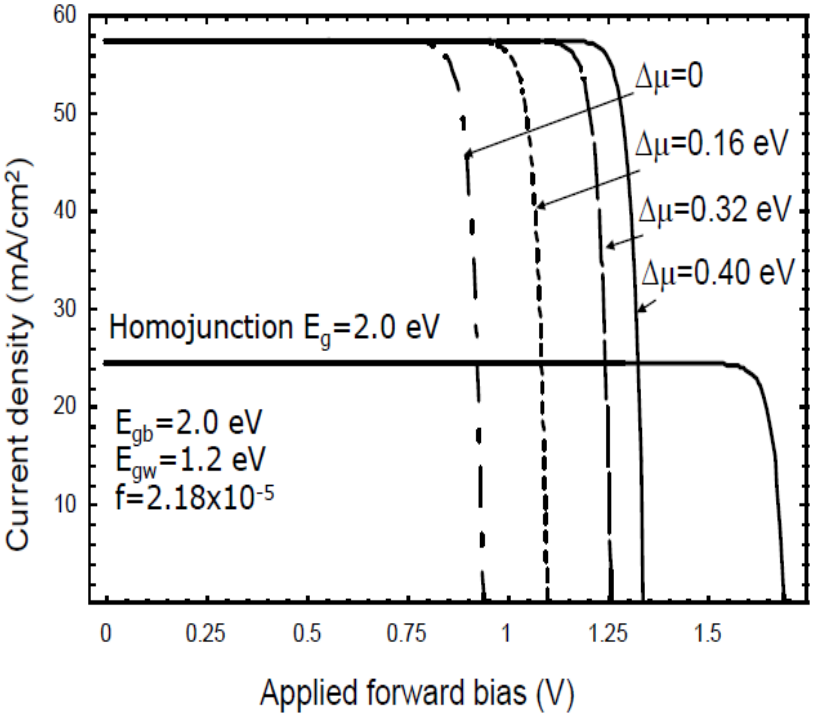

Figure 2: Current density vs. voltage characteristics under unconcentrated solar illumination for a quantum solar cell with barrier and well band gaps of E_{gb}=2.0 eV and E_{gw}=1.2 eV, respectively. Also shown are calculations for a homojunction solar cell with band gap of 2.0 eV.

Here, $\Delta\mu$ is the quasi-Fermi-level splitting between the barrier and quantum materials.

Figure 2 shows the *J-V* characteristics for quantum solar cells with different barrier and quantum material band gaps (E_{gb}=2.0 eV and E_{gw}=1.2 eV), and a homojunction solar cell with a band gap of 2.0 eV for comparison. Homojunction solar cells employing barrier materials with E_{gb}=2.0 eV and quantum materials with E_{gw}=1.2 eV have calculated open circuit voltages of V_{oc} = 1.70 V and 0.94 V, respectively. When the QFL is constant throughout the cell, the V_{oc} of the quantum heterostructure solar cell with energy gaps E_{gb} and E_{gw}, is the same as that of the corresponding conventional cell of single gap, E_{gw}. As a result, the device performances are identical. When the quantum device structure sustains a QFL discontinuity, V_{oc} is determined by both the barrier and quantum materials. Based on theoretical considerations of the radiative limits, Anderson [17] found that the V_{oc} of quantum well solar cells was consistently higher than that of conventional cells formed by the well materials, as has been verified experimentally [18]. While Anderson's ideal radiative limit calculation is based on constant QFL separation, the radiative recombination current in the quantum materials is overestimated, resulting in the different band gaps and offsets compared with our results.

Finally, we calculate the entropy generation rate $\dot{S}_{irr}$ [5]. Here, $\dot{S}_{irr}$ is the difference between the entropy flux leaving and entering the cells, following:

$$\begin{aligned} T_a\dot{S}_{\mathrm{irr}} = -P &+ [\dot{E}(E_{\mathrm{gw}},\infty,T_{\mathrm{sun}},0) - T_a\dot{S}(E_{\mathrm{gw}},\infty,T_{\mathrm{sun}},0)] \\ &- [\dot{E}(E_{\mathrm{gw}},E_{\mathrm{gb}},T_a,V-\Delta\mu) - T_a\dot{S}(E_{\mathrm{gw}},E_{\mathrm{gb}},T_a,V \\ &- \Delta\mu)] - [\dot{E}(E_{\mathrm{gb}},\infty,T_a,V) - T_a\dot{S}(E_{\mathrm{gb}},\infty,T_a,V)], \end{aligned} \tag{8}$$

where the radiant energy flux, $\dot{E}$, satisfies [5]:

$$\dot{E}(E_1,E_2,T,\mu)=\frac{2\pi}{h^3c^2}\int_{E_1}^{E_2}\frac{E^3}{\exp[(E-\mu)/kT]-1}dE, \quad , \tag{9}$$

and $\dot{E}-T\dot{S}=\mu\phi+\dot{\Omega}$, where the grand potential flux, $\dot{\Omega}$ [5]:

$$. \qquad \dot{\Omega}(E_1,E_2,T,\mu)=kT\frac{2\pi}{h^3c^2}\int_{E_1}^{E_2}\ln[1-e^{(\mu-E)/kT}]E^2dE \tag{10}$$

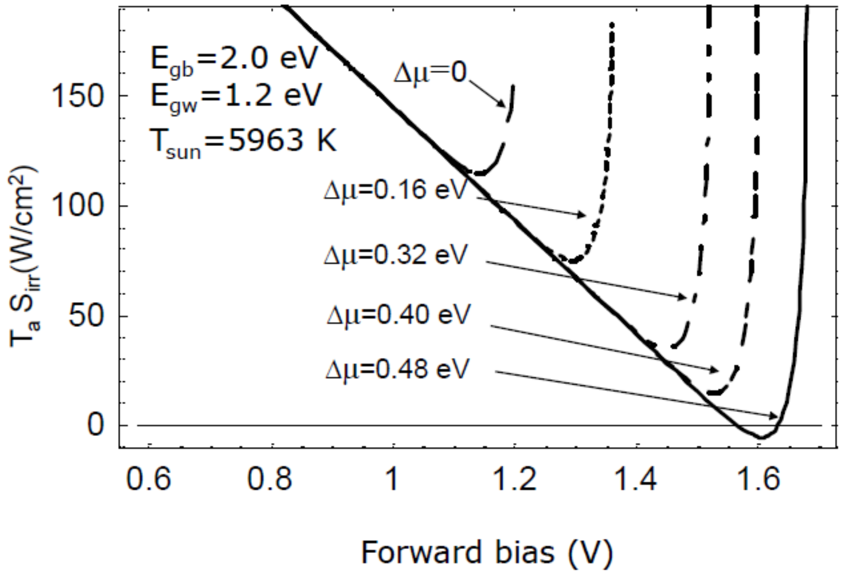

Figure 3: Entropy generation rate multiplied by the ambient temperature ($T_a\dot{S}_{irr}$) for a quantum confined cell with a barrier energy gap of E_{gb} = 2.0 eV and a well energy gap of E_{gw} = 1.2 eV at various quasi-Fermi level splittings, $\Delta\mu$. The irradiator and ambient temperatures are assumed at T_{sun}= 5963 K and T_a = 300 K, respectively.

The calculated entropy generation rate versus the terminal voltage, *V,* in the quantum solar cells (E_{gb}=2.0 eV and E_{gw}=1.2 eV) with an irradiator temperature of T_{sun}=5963 K is shown in Fig. 3. With an increase in *V*, the entropy generation rate decreases to a positive minimum, and then once again increases rapidly. An increase in $\Delta\mu$ shifts the minimum entropy generation rate to a higher voltage. When $\Delta\mu = 0.48\ eV$ (corresponding to ξ=0.6), S_{irr} becomes negative at $V >$ 1.57 V due to the negative entropy contribution at the QFL discontinuity, indicating an unphysical mode of operation. The maximum efficiency versus band gap ratio shown in the lower inset of Fig. 1 is based on appropriate QFL separation obeying the second law of thermodynamics.

In conclusion, a detailed balance approach is applied to calculate the efficiency limits of quantum heterostructure solar cells. In the radiative limit, the carrier temperature in the wells exceeds that of the barrier, introducing a positive discontinuity in QFL between well and barrier regions. In this case, a maximum power conversion efficiency of 44.5% is calculated for $\Delta\mu =$ +0.48eV when the band gaps of the barrier and well materials are optimized to 2.0 eV and 1.2 eV, respectively.

References

[1] K.W.J. Barnham and G. Duggan, *J. Appl. Phys.* **67**, 3490(1990).

[2] W. Shockley and H. J. Queisser, *J. Appl. Phys*. **32**, 510(1961).

[3] C. B. Honsberg, S. P.Bremner, Corkish R., *Physica E* **14**, 136(2002).

[4] N. G. Anderson, *Physica E* **14**, 126(2002).

[5] A. Luque, A. Martí, and L. Cuadra, *IEEE Trans. Electron Devices* **48**, 2118 (2001).

[6] A. Luque and A. Martí, *Phys. Rev. Lett.* **78**, 5014(1997).

[7] V. Aroutiounian, S. Petrosyan, and A. Khachatryan, *Sol. Energy Mater. Sol. Cells* **89**, 165(2005).

[8] A. Martí, N. López, E. Antolín, E. Cánovas, C. Stanley, C. Farmer, L. Cuadra, and A. Luque, *Thin Solid Films* **511**, 638(2006).

[9] S. Suraprapapich, S. Thainoi, S. Kanjanachuchai, and S. Panyakeow, *Sol. Energy Mater. Sol. Cells* **90**, 2968(2006).

[10] J. Nelson, J. Barnes, N. E. Daukes, B. Kluftinger, E. Tsui, K. Barnham, C. Foxon, T. Cheng, and J. Roberts, *J. Appl. Phys* **82**, 6240(1997).

[11] K.Yang, J. East and G. Haddad, *Solid-State Electronics* **36**, 321(1993).

[12] A. Luque, A. Marti, N. Lopez, E. Antolin, E. Canovas, C. Stanley, C. Farmer, L. J. Caballero, L. Cuadra, and J. L. Balenzategui, *Appl. Phys. Lett.* **87**, 083505(2005).

[13] A. Van Der Ziel, *Solid-State Electronics* **16**, 1509(1973).

[14] P. Würfer, *Physics of solar cells*, Willey-vch, P57 (2005).

[15] M. Mazzer, K. W. J. Barnham, N. Ekins-Daukes, D. B. Bushnell, J. Connolly, G. Torsello, D. Diso, S. Tundo, M. Lomascolo, and A. Licciulli, *3rd World Conference on*

Photovoltaic Energy Conversion, 2661(Osaka, 2003).

[16] A. De Vos, *J. Phys. D: Appl. Phys.* **13**, 839(1980).

[17] N. G.Anderson, *J. Appl. Phys.* **78**, 1850(1995).

[18] K. Barnham, J. Connolly., P. Griffin, G. Haarpaintner, J. Nelson, E. Tsui, A. Zachariou, J. Osborne, C. Button, G. Hill, M. Hopkinson, M. Pate, J. Roberts, and T. Foxon, *J. Appl. Phys.* **80**, 1201(1996).

Appendix 2

Thermodynamic limits of quantum photovoltaic cell efficiency based on two photon absorption

The model of Luque and Marti[1] (L&M) is fundamentally different than our model described in Ref. 2. The L&M model requires a sequential, two photon absorption processes to exceed the Shockley-Queisser (SQ) limit, while our model assumes only single photon transitions where recycling of carrier thermalization energy in the quantum wells leads to efficiencies higher than predicted by the SQ limit. This distinction results in predicted efficiencies that exceed that of the L&M model for some bandgap energy combinations, as pointed out in their comment.

To compare the two models, in Fig. 1 we show the maximum predicted efficiency at one sun concentration ($f = 2.18\times10^{-5}$) and maximum solar concentration (f=1) for the L&M model, whereas the inset shows the upper limit efficiency for our model at one sun concentration. We note that in our original paper[2], we avoided calculations at f = 1, which corresponds to a physically irrelevant concentration factor of 4600. For the L&M model, the maximum efficiency shifts from 63.1% (E_i=0.7 eV, E_g=1.93 eV) at f=1 to 46.7% (E_i=0.9 eV, E_g=2.36 eV) at $f = 2.18\times10^{-5}$, where E_i is the intermediate band energy in the quantum region, and E_g is the band gap energy of the host semiconductor. Since only the absorption of the second photon contributes to the sub-band-gap photocurrent for L&M model, for comparison between these two models, the band gap of the quantum material is $E_{gw} = E_g - E_i$. The efficiency at the corresponding band gap energy combination of E_{gw}=1.46 eV and E_{gb}=2.36 eV for the model in Ref. 2 is 40.0 %. The upper limit efficiency is 44.5% (E_{gb}=2.0 eV, E_{gw}=1.2 eV), whereas for the

L&M model, the limiting efficiency is 41.0% for this same energy band gap combination as claimed in the comment. It is clear that some bandgap combinations lead to higher efficiency in our model, while others lead to higher efficiency in the L&M model. The overall, limiting efficiency of the L&M model is higher than ours. Since the two models are based on fundamentally different physical assumptions, the choice of an identical bandgap combination as a basis for comparison between the two models, as in L&M's comment, seems arbitrary. Instead, the overall, limiting efficiency of each model model should be compared, as in Fig. 1.

The efficiency differences between the two models can be understood as follows. In both cases, the cell operates at a voltage higher than the lowest quasi-Fermi level splitting in the system, leading to efficiencies exceeding the SQ limit to be surpassed. In the L&M model, the second photon supplies the energy needed for this mode of operation, while in our model it is supplied by excess carrier thermalization energy that elevates the well carrier temperature to thermoelectrically drive the QFL discontinuity, $\Delta\mu$. Photocurrent due to sub-band-gap photon absorption[1] is delivered only when the VB $\Rightarrow$ IB and IB $\Rightarrow$ CB transition rates are exactly equal. Our model does not have this restriction, and it is this added flexibility that allows for greater efficiency than the L&M model for some energy gap combinations shown in Fig. 1. Note, however, as in Ref. 2, $\Delta\mu$ is thermodynamically limited by the finite thermalization energy available, which is equal to the sum of all photon energies in excess of the transition energy. Exceeding this total (by operation at $\Delta\mu$ >0.4eV) leads to an unphysical mode of operation, as evidenced by negative total entropy generation, limiting the efficiency to 44.5%.

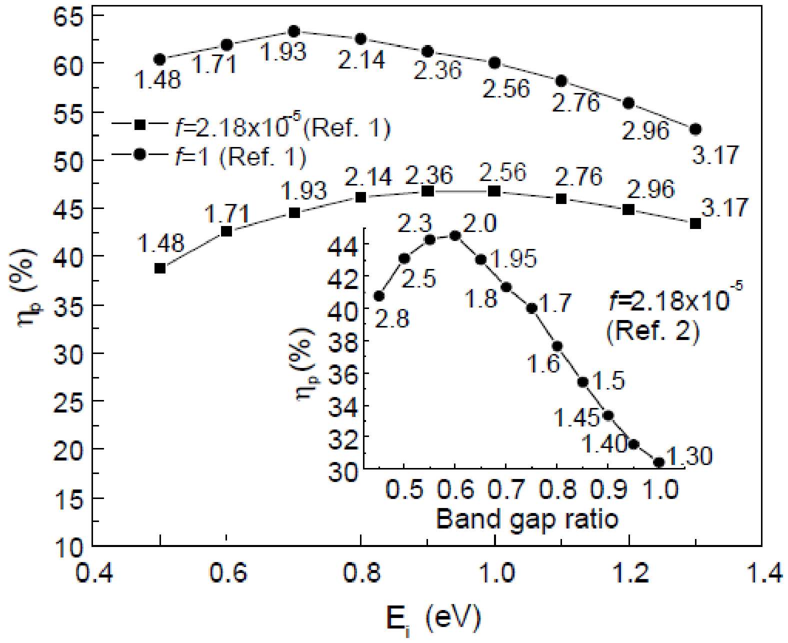

In conclusion, the assumptions of our model are different from that of L&M, and hence our results are not in conflict with L&M's results. Rather, our work aims at determining the theoretical efficiency limit of quantum solar cells that employ single photon absorption in the absence of unrealistic concentration factors assumed in Ref. 1.

References:

[1] A. Luque, A. Martí, Phys. Rev. Lett. **78**, 5014(1997).

[2] G. D. Wei, K.-T. Shiu, N. C. Giebink, S. R. Forrest, Appl. Phys. Lett. **91**, 223507 (2007).

Appendix 3

List of Publications, Conference Presentations and Patents

1. Guodan Wei, Xin Xiao, Siyi Wang, Kai Sun, Mark E. Thompson, and Stephen R. Forrest, *Functionalized Squaraine Donors for Nanocrystalline Organic Photovoltaics*, **ACS Nano**, 6(1), 972-978(2011).
2. Guodan Wei, Siyi Wang, Kai Sun, Mark E. Thompson, Stephen R. Forrest, *Solvent annealed crystalline squaraine: $PC_{70}BM$ (1:6) solar cells,* **Advanced Energy Materials, 1(2),** 184-187(2011).
3. Guodan Wei, Xin Xiao, Siyi Wang, Jeramy D. Zimmerman, Kai Sun, Vyacheslav V. Diev, Mark E. Thompson, and Stephen R. Forrest, *Arylamine-Based Squaraine Donors for Use in Organic Solar Cells*, **Nano letters**, 11(10), 4261-4264(2011).
4. Guodan Wei, Richard R. Lunt, Sun Kai, Siyi Wang, Mark E. Thompson, Stephen R. Forrest, *Efficient, Ordered bulk heterojunction nanocrystalline solar cells by annealing of ultrathin squaraine thin films*, **Nano Letters**, 10(9), 3555, (2010).
5. Guodan Wei, Siyi Wang, C. Kyle Renshaw, Mark E. Thompson, Stephen R. Forrest, *Solution processed squaraine bulk heterojunction photovoltaic cells*, **ACS Nano**, 4(4), 1927, (2010)
6. Guodan Wei, Kuen-Tsing Shiu, N. Chris Giebink, Stephen R. Forrest, *Response to "Comment on 'Thermodynamic limits of quantum photovoltaic cell efficiency'"*, **Applied Physics Letters**, 92(6), 066101, (2008).
7. Guodan Wei, Kuen-Tsing Shiu, N. Chris Giebink, Stephen R. Forrest, *Thermodynamic limits*

of quantum photovoltaic cell efficiency, **Applied Physics Letter**s, 90(22): 223507, (2007).

8. Guodan Wei, Stephen R. Forrest, *Intermediate-band solar cells employing quantum dots embedded in an energy fence barrier*, **Nano Letters**, 7 (1): 218-222, (2007).
9. Xin Xiao, Guodan Wei, Siyi Wang, Jeramy D. Zimmerman, Christopher K. Renshaw’ Mark E. Thompson, Stephen R. Forrest, *Small-molecule photovoltaics based on functionalized squaraine donor blends*, accepted by **Advanced Materials**, (2012).
10. Brian E. Lassiter, Guodan Wei, Xin Xiao, Siyi Wang, Mark E. Thompson, Stephen R. Forrest, *Electron conducting buffer layers in organic photovoltaics*, **Applied Physics Letters**, 98(24), 243307 (2011).
11. Siyi Wang, Lincoln Hall, Vyacheslav V. Diev, Guodan Wei, Xin Xiao, Peter I. Djurovich, S.R.Forrest, M. E Thompson, *Chem. Mater.*, 23(21), 4789(2011).
12. Siyi Wang, Elizabeth I. Mayo, M. Dolores Perea, Laurent Griffe, Guodan Wei, Peter I. Djurovich, Stephen R. Forrest, Mark E. Thompson, *High efficiency organic photovoltaic cells based on a vapor deposited squaraine donor*, **Applied Physics Letters**, 94, 233304, (2009).
13. Xiaoran Tong, Rhonda F. Bailey-Salzman, Guodan Wei, Stephen R. Forrest. *Inverted small molecule organic photovoltaic cells on reflective substrates*, **Applied Physics Letters**, 93, 173304, (2008).
14. Ning Li, Brian E. Lassiter, Richard R. Lunt, Guodan Wei, Stephen R. Forrest, *Open circuit voltage enhancement due to reduced dark current in small molecule photovoltaic cells*, **Applied Physics Letters**, 94, 023307, (2009).

CONFERENCE PRESENTATIONS

1. Guodan Wei, Xin Xiao, Siyi Wang, Mark E. Thompson, Stephen R. Forrest, *New squaraine donors for high efficiency organic photovoltaic cells,* 37th IEEE Photovoltaic Specialists Conference, 2011, Seattle, Washington.
2. Guodan Wei, Xin Xiao, Siyi Wang, Kyle Renshaw, Mark E. Thompson, Stephen R. Forrest, *High efficiency energy harvesting using nanocrystalline solar cells,* Science for our nation's Energy future Summit and Forum, 2011, Washington, DC.
3. Xin Xiao, Guodan Wei, Siyi Wang, Mark E. Thompson, Stephen R. Forrest, *High efficiency small molecular solar cells based on blending two squaraine donors*, MRS 2011 Fall meeting, Symposium H: Organic Photovoltaic Devices and Processing, Boston, MA.
4. Stephen R. Forrest, Guodan Wei, Siyi Wang, Mark E. Thompson, *Solution processed of small molecule bulk heterojunction solar cells*, MRS 2011 Spring meeting, Symposium OO: Synthesis and processing of organic and polymeric materials for semiconductor applications, San Francisco, CA.
5. Guodan Wei, Siyi Wang, Kai Sun, Mark E. Thompson and Stephen R. Forrest, *Morphology control of solution processed squaraine: $PC_{70}BM$ bulk heterojunction photovoltaic cells,* 8th International Conference on Electroluminescence & Organic Optoelectronics (ICEL2010), Ann Arbor, MI.
6. Guodan Wei, Siyi Wang, Ning Li, Jeramy Zimmerman, Kai Sun, Mark Thompson, Stephen R. Forrest, *Solution processable squaraine/$PC_{70}BM$ bulk heterojunction photovoltaic cells*, MRS 2009 Fall meeting, Symposium S: Organic materials and devices for sustainable energy systems, Boston, MA.
7. Mark Thompson, Stephen R. Forrest, M. Dolores Perez, Siyi Wang, Guodan Wei, Cody

Schlenker, *New materials for organic photovoltaics*, MRS 2009 Fall meeting, Symposium S: Organic materials and devices for sustainable energy systems, Boston, MA.

8. Brian E. Lassiter, Guodan Wei, Zhi L. Li, Stephen R. Forrest, *Improved spectral uniformity and high open-circuit voltage organic tandem solar cells based on the subphthalocyanines*, MRS 2008 Fall Meeting, Symposium H: Physics and technology of organic semiconductor devices, Boston, MA.
9. Guodan Wei, Stephen R. Forrest, *Intermediate-band solar cells employing quantum dots embedded in an energy fence barrier*, **MRS 2006 Fall meeting**, Symposium M: Quantum dots-Growth, Behavior, and Applications, Boston, MA.

Patents

1. Mark E. Thompson, Siyi Wang, Lincoln Hall, Vyacheslav V. Diev, Stephen R. Forrest, Guodan Wei, Xin Xiao, *New aryl squaraines for photovoltaic application,* pending, 2011.
2. Stephen R. Forrest, Brian E. Lassiter, Guodan Wei, Xin Xiao, *Electron conducting buffer layers in organic photovoltaics*, pending, 2011.
3. Stephen R. Forrest, Guodan Wei, *Thermal and solvent annealing influence on the performance of solution-processed squaraine/C_{60} planar and squaraine:$PC_{70}BM$ bulk heterojunction photovoltaic cells*, pending, 2010
4. Stephen R. Forrest, Guodan Wei, *Type II quantum dot solar cells*

   U. S. Patent No, 20,090,095,349
5. Stephen R. Forrest, Guodan Wei, *Quantum dot solar cells employing energy fences*

   U. S. Patent No, 20,070,151,592
6. Stephen R. Forrest, Ning Li, Guodan Wei, Enhancement of organic photovoltaic cell open

circuit voltage using electron/hole blocking exciton blocking layers

U.S. Patent No, 20,110,012,091

7. Stephen R. Forrest, Brian E. Lassiter, Guodan Wei, *Small molecule organic tandem solar cells*

   U.S. Patent No, 2,010,0084,011